

20cm e-MERLIN Observations of an Optically Selected Nearby Galaxy Sample

A THESIS SUBMITTED TO THE UNIVERSITY OF MANCHESTER
FOR THE DEGREE OF MASTER OF SCIENCE
IN THE FACULTY OF ENGINEERING AND PHYSICAL SCIENCES

2015

By
Ruth Evans
School of Physics and Astronomy

Contents

Abstract	12
Declaration	13
Copyright	14
Acknowledgements	15
The Author	16
	17
1 Introduction	19
1.1 Radiative processes	23
1.1.1 Thermal Radiation	23
1.1.2 Non-Thermal Radiation	23
1.2 Galaxy Types and Sources of Radio Emission	25
1.2.1 Active Galaxies	25
1.2.2 Unification of Active Galactic Nuclei	30
1.2.3 Radio Emission from Normal Galaxies	31
1.2.4 Radio Emission from Active Galactic Nuclei	35
1.3 The Far Infrared-Radio Correlation	37
1.4 Radio Observations of Compact Objects	40
1.5 LeMMINGs	42

1.5.1	Scientific Goals	43
1.5.2	LeMMINGs Galaxy Sample	44
1.6	Scientific Goals of this Thesis	45
2	Radio Interferometry	47
2.1	Interferometry	47
2.1.1	The (u,v) Plane	50
2.1.2	Aperture Synthesis	51
2.1.3	Antenna Weighting	54
2.1.4	Deconvolution Methods	54
2.1.5	Image Weighting	56
2.1.6	Wide-Field Imaging and Limitations	57
2.2	e-MERLIN	59
2.3	Observations and Data Reduction	61
2.3.1	e-MERLIN Data Reduction	62
2.3.2	Imaging and Self-Calibration	68
2.4	Summary	69
3	Results	70
3.1	NGC 7817 (0003+2045)	72
3.2	IC10 (0020+5917)	77
3.3	NGC 147 (0033+4830)	83
3.4	NGC 185 (0038+4820)	87
3.5	NGC 205 (0040+4141)	90
3.6	NGC 221 (0042+4051)	96
3.7	M31 (0042+4116)	100
3.8	NGC 278 (0052+4733)	109
3.9	NGC 7741 (2343+2604)	113
3.10	NGC 7798 (2359+2045)	119
3.11	Summary	121

CONTENTS

4	Discussion	124
4.1	Galaxy Luminosities	124
4.2	Detecting Active Galactic Nuclei	127
4.2.1	Radio-Loud AGN	127
4.2.2	Radio Quiet AGN	128
4.3	Detecting Supernovae Remnants	130
4.4	NGC 7817	133
4.5	IC10	133
4.6	NGC 147	134
4.7	NGC 185	134
4.8	NGC 205	135
4.9	NGC 221	135
4.10	M31	136
4.11	NGC 278	137
4.12	NGC 7741	137
4.13	NGC 7798	138
4.14	Determining a Star Formation and Radio Supernova Rate from Radio Observations	138
4.15	Summary	142
5	Conclusion and Future Work	146
	References	149

Word Count: 20,957

List of Tables

1.1	Observation Schedule for the LeMMINGs Project	42
2.1	e-MERLIN Technical Capabilities	60
2.2	Calibrator Sources	62
2.3	e-MERLIN Telescopes	62
3.1	Thesis Sample Source List	71
3.2	Observed Values for a Source in the Field of NGC 7817	75
3.3	Observed Values for the Compact Object in IC10	80
3.4	Observed Values for a Source in the Field of IC10	82
3.5	Observed Values for a Source in the Field of NGC 147	86
3.6	Observed Values for a Source in the Field of NGC 205	93
3.7	Observed Values for a Source in the Field of NGC 205	95
3.8	Observed Values for a Source in the Field of NGC 221	99
3.9	Observed Values for a Source in the Field of M31	104
3.10	Observed Values for a Source in the Field of M31	107
3.11	Observed Values for a Source in the field of NGC 278	112
3.12	Observed Values for a Source in the field of NGC 7741	116
3.13	Observed Values for a Source in the Field of NGC 7741	118
3.14	Beam Sizes, Flux Density Expectations and RMS Noise Values for All Galaxies	122

LIST OF TABLES

4.1	e-MERLIN Flux Density and Luminosity Expectations of Each Galaxy	126
4.2	The Expected Flux Density of a Radio-Quiet AGN at the Distance of Each Target Galaxy	129
4.3	The Expected Flux Density of a SNR at the Distance of Each Target Galaxy	132
4.4	The Star Formation and Radio Supernovae Rates for Each Galaxy	141

List of Figures

1.1	Typical SED of Normal, Starburst and Seyfert Galaxies	21
1.2	Radio and Far Infrared Spectrum of M82	24
1.3	Optical Spectra of AGN Types	25
1.4	Optical Spectrum of the Quasar PKS0454+039	26
1.5	The FRII Galaxy 3C 175	28
1.6	Radio-loud AGN Unification	30
1.7	Contour Maps of Normal Galaxies	32
1.8	Global Emission from Normal Galaxies	33
1.9	Supernovae Shock Waves	35
1.10	The FIR/Radio Correlation	37
1.11	Radio Maps of Compact Objects within M82	40
1.12	Radio Spectra of Compact Sources in M82	41
1.13	The LeMMINGs Galaxy Sample	44
2.1	Two-Element Interferometer	48
2.2	UV Coverage of the Target Source NGC 7817 at a Frequency of 1.7026 GHz.	52
2.3	UV Coverage of the Target Source NGC 7817 with Continuous Coverage Between 1.25 GHz and 1.71 GHz.	53
2.4	Spectral Plot of Flagged, Fringe-Fitted and Bandpass-Calibrated Data for OQ 208	66
2.5	Flowchart of the Calibration Procedure in AIPS	67

LIST OF FIGURES

3.1	<i>Spitzer</i> 3.6 μm Image of NGC 7817	72
3.2	NVSS Field of NGC 7817	73
3.3	A Source in the Field of NGC 7817	74
3.4	IC 10: A Dwarf Irregular Galaxy	77
3.5	24 μm <i>Spitzer</i> MIPS Image of IC10	78
3.6	NVSS Field of IC10	79
3.7	A Compact Object in IC10	80
3.8	A Source in the Field of IC10	81
3.9	24 μm <i>Spitzer</i> MIPS Image of NGC 147	83
3.10	NVSS Field of NGC 147	84
3.11	A Source in the Field of NGC 147	85
3.12	24 μm <i>Spitzer</i> MIPS Image of NGC 185	87
3.13	NVSS Field of NGC 185	88
3.14	A 24 μm <i>Spitzer</i> Image of NGC 205	90
3.15	NVSS Field of NGC 205	91
3.16	A Source in the Field of NGC 205	92
3.17	A Source in the Field of NGC 205	94
3.18	24 μm <i>Spitzer</i> MIPS Image of NGC 221	96
3.19	NVSS Field of NGC 221	97
3.20	A Source in the Field of NGC 221	98
3.21	20 cm VLA Image of M31	100
3.22	24 μm <i>Spitzer</i> MIPS image of M31	101
3.23	NVSS Field of M31	102
3.24	A Source in the Field of M31	103
3.25	A Source in the Field of M31	105
3.26	VLA Image of a Source in the Field of M31	106
3.27	24 μm <i>Spitzer</i> MIPS Image of NGC 278	109
3.28	NVSS Field of NGC 278	110
3.29	A Source in the Field of NGC 278	111

LIST OF FIGURES

3.30	24 μm <i>Spitzer</i> MIPS Image of NGC 7741	113
3.31	NVSS Field of NGC 7741	114
3.32	A Source in the Field of NGC 7741	115
3.33	A Source in the Field of NGC 7741	117
3.34	24 μm <i>Spitzer</i> MIPS Image of NGC 7798	119
3.35	NVSS Field of NGC 7798	120
4.1	Plot of SNR Flux Density Against Distance	131
4.2	1.4 GHz SNR Light Curve Including Individual Luminosity Limits of Each Galaxy	140

Glossary of Terms

2MASS	Two Micron All-Sky Survey
AGN	Active Galactic Nucleus/Nuclei
AIPS	Astronomical Image Processing System
BL Lac	BL Lacertae
BLR	Broad-Line Region
BLRG	Broad-Line Radio Galaxy
Cas A	Cassiopeia A
CCSNe	Core-Collapse Supernovae
CRE	Cosmic Ray Electron
CSM	Circumstellar Material
e-MERLIN	e-Multi-Element Remote Linked Interferometer Network
EVLA	Expanded Very Large Array
FIR	Far InfraRed
FOV	Field of View
FRI	Fanaroff-Riley I
FRII	Fanaroff-Riley II
FT	Fourier Transform
IF	Intermediate Frequency
IMF	Initial Mass Function
ISM	InterStellar Medium
LeMMINGs	Legacy e-MERLIN Multi-band Imaging of Nearby Galaxies
LINER	Low Ionization Nuclear Emission-line Region
MERLIN	Multi-Element Radio Linked Interferometer Network
MEM	Maximum Entropy Method
MIPS	Multi-band Imaging Photometry for <i>Spitzer</i>

NASA	National Aeronautics and Space Administration
NED	NASA Extragalactic Database
NLR	Narrow-Line Region
NLRG	Narrow-Line Radio Galaxy
NRAO	National Radio Astronomy Observatory
NVSS	NRAO VLA Sky Survey
OVV	Optically Violent Variable
RFI	Radio Frequency Interference
RMS	Root Mean Square
RSNe	Radio Supernovae
SED	Spectral Energy Distribution
SF	Star Formation
SFR	Star Formation Rate
SHA	<i>Spitzer</i> Heritage Archive
SKA	Square Kilometre Array
SMBH	Super Massive Black Hole
SN	Supernova
SNe	Supernovae
SNR	Supernova Remnant
UK	United Kingdom
ULIRG	Ultra-Luminous InfraRed Galaxy
UV	Ultra-Violet
VLA	Very Large Array
VLBA	Very Long Baseline Array
WIM	Warm Ionized Medium

The University of Manchester

ABSTRACT OF THESIS submitted by Ruth Evans

for the Degree of Master of Science and entitled

“20cm e-MERLIN Observations of an Optically Selected Nearby Galaxy
Sample”, 2015.

We present high resolution ($\sim 0''.2$) 1.2 - 1.7 GHz (L-band) e-MERLIN observations of a LeMMINGs sub-sample consisting of 10 nearby, optically selected galaxies. The LeMMINGs project aims to study star formation at both L and C-bands (4 - 8 GHz) for a total of 286 galaxies with a median distance of 20 Mpc. The ten galaxies included in this thesis are a sub-sample of this project and comprise of the fourth observation block, in which each galaxy has been observed for a total of 40 minutes. Wide-field maps have been produced for each of the targets in order to search for any compact objects within the galaxy and the surrounding field. IC10 is included in the sub-sample of galaxies for this thesis. In this galaxy one HII region has been detected and imaged. There are no detections of any compact objects or extended emission within the other 9 target galaxies in this small sub-sample. Due to the high resolution of the e-MERLIN observations, much of the extended emission from the targets has been resolved out resulting in the low detection rate. In this thesis an analysis of the limits derived from these observations with respect to rates of star formation and AGN activity has been presented. It is concluded that low to moderate star formation rates of the galaxies studied here is consistent with the non-detection of compact radio emission from radio supernovae. No evidence for radio-emitting compact AGN components is found in any sources in this sub-sample. This is consistent with previous observations of these sources in the literature. It is hoped that future deep tier observations of IC10 will yield a higher number of detections for further analysis, but deeper observations are needed of the other 9 galaxies to study their radio and star-forming properties in greater detail.

Declaration

No portion of the work referred to in this thesis has been submitted in support of an application for another degree or qualification of this or any other university or other institution of learning.

Copyright

The author of this thesis (including any appendices and/or schedules to this thesis) owns certain copyright or related rights in it (the “Copyright”) and she has given The University of Manchester certain rights to use such Copyright, including for administrative purposes. Copies of this thesis, either in full or in extracts and whether in hard or electronic copy, may be made only in accordance with the Copyright, Designs and Patents Act 1988 (as amended) and regulations issued under it or, where appropriate, in accordance with licensing agreements which the University has from time to time. This page must form part of any such copies made. The ownership of certain Copyright, patents, designs, trade marks and other intellectual property (the “Intellectual Property”) and any reproductions of copyright works in the thesis, for example graphs and tables (“Reproductions”), which may be described in this thesis, may not be owned by the author and may be owned by third parties. Such Intellectual Property and Reproductions cannot and must not be made available for use without the prior written permission of the owner(s) of the relevant Intellectual Property and/or Reproductions. Further information on the conditions under which disclosure, publication and commercialisation of this thesis, the Copyright and any Intellectual Property and/or Reproductions described in it may take place is available in the University IP Policy (see <http://www.campus.manchester.ac.uk/medialibrary/policies/intellectual-property.pdf>), in any relevant Thesis restriction declarations deposited in the University Library, The University Library’s regulations (see <http://www.manchester.ac.uk/library/aboutus/regulations>) and in The University’s policy on presentation of Theses.

Acknowledgements

I would like to express my gratitude to my supervisors Dr. Robert Beswick and Dr. Megan Argo for the many hours spent reading through this thesis, and for helping me through the steep learning curve that is AIPS.

I would also like to thank my fellow MSc and PhD students for the moral (and occasionally immoral) support. You truly are a wonderful bunch.

I cannot forget to thank my family and friends who have supported me throughout this project, and for sticking with me even though I may not have shown much appreciation at the time. Thank you.

The Author

The author was born in March 1993 in Essex, England. She studied a BSc in Observational Astronomy at the University of South Wales where she graduated in July 2014. In September 2014 she started an MSc at the Jodrell Bank Centre for Astrophysics, for which this thesis is submitted.

*To my wonderful Mum and Stepfather, without
whom this thesis would not be submitted. Thank you
for both your emotional and financial support,
I owe you one.*

Chapter 1

Introduction

Radio emission accounts for just 0.0001% of the bolometric luminosity of a normal galaxy (Condon 1992), but despite the relatively small contribution to the overall emission, observing galaxies at radio frequencies gives unprecedented insight into regions of the galaxy that are obscured at other wavelengths. Radio astronomy is also a useful tool when used in correspondence with observations at other wavelengths to obtain a better understanding of the physical processes occurring in objects that emit radiation over a broad spectrum.

Above ~ 200 GHz, thermal radiation of dust heated by stars dominates radio observations and so frequencies above this limit cannot be considered as radio continuum observations due to the thermal blackbody nature of the emission. This frequency defines an efficient upper limit to radio band observations (Condon 1992).

Radio emission is detected from a wide range of galaxy types, including spiral, dwarf irregular and peculiar types, as well as interacting systems. This emission has also been detected in a limited number of elliptical and lenticular type galaxies with ongoing star formation (Condon 1992; Ho 1999). The key similarity between these objects is the formation of stars which is indicated by the presence of HII regions (emitting free-free radiation) and supernovae (SNe) (type Ibc and II

emitting synchrotron radiation) from massive stars greater than $8M_{\odot}$ (Beswick et al. 2014b).

The power emitted by normal galaxies at a frequency of 1.4 GHz ranges between $L \sim 10^{18} h^{-2} \text{ W Hz}^{-1}$ and $L \sim 10^{23} h^{-2} \text{ W Hz}^{-1}$ (Condon 1992). Normal galaxies with relatively high radio luminosities often contain a large number of disturbed, peculiar and interacting systems compared to galaxies on the lower end of this range, indicating that regions of star formation provide an ideal environment for the production of thermal and non-thermal radio emission (Bressan et al. 2002). As a result, observing galaxies at radio frequencies is beneficial due to the nature of the objects within the galaxy. Starburst galaxies typically contain large quantities of gas and dust which can obscure observations at other wavelengths such as optical. At radio frequencies, this starburst activity is transparent which enables the observed flux to be relative to the intrinsic luminosity. The typical spectral energy distribution (SED) of both normal and starburst galaxies can be seen in Figure 1.1.

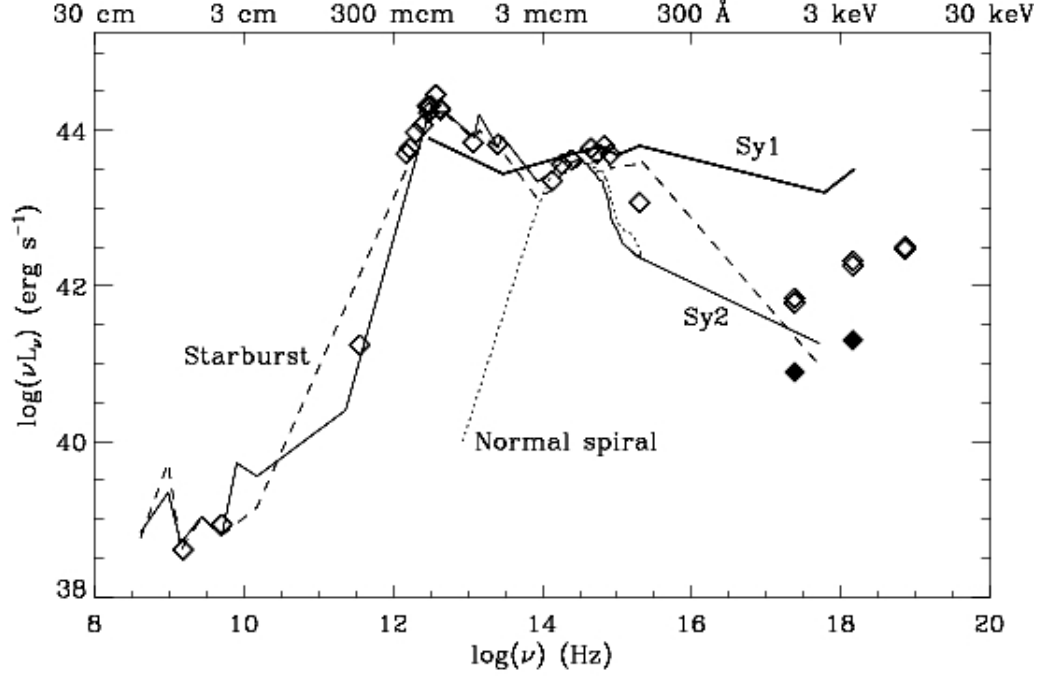


Figure 1.1: The typical spectral energy distribution (SED) of spiral, starburst and Seyfert galaxies. The dotted line shows a typical spectrum of a normal spiral galaxy, the dashed line represents a typical starburst galaxy, and the thick and thin solid lines represent Seyfert 1 and Seyfert 2 galaxies respectively which are discussed in section 1.2.1. The open diamonds correspond to actual spectral measurements of the starburst galaxy NGC 7679. Points at 6cm (5 GHz) and 20cm (1.5 GHz) are observed by the VLA, and the filled diamonds represent X-ray data from the XMM-Newton archive. Image taken from Yankulova et al. (2007).

A few percent of galaxies host an active galactic nucleus (AGN), and radio-loud AGN are powerful emitters at radio wavelengths. Typical low-luminosity AGN range between 1.8×10^{18} and 1.8×10^{21} W Hz $^{-1}$ at a frequency of 1.4 GHz (Ho and Peng 2001), and high-luminosity AGN can exceed the luminosity of a thousand normal galaxies (Begelman et al. 1984).

Within normal and active galaxies, there are two radiation mechanisms that account for nearly all radio emission; thermal free-free radiation and non-thermal

synchrotron radiation which are discussed in detail in sections 1.1.1 and 1.1.2 respectively. The term ‘thermal’ relates to radiation resulting from the acceleration of charged particles whose movement and energy is a direct result of temperature. Thermal radiation is emitted predominantly via Bremsstrahlung, or free-free, emission. For observations of galaxies at radio wavelengths, the term ‘thermal’ generally relates to free-free radiation rather than blackbody, as blackbody radiation from galaxies is above the typical ~ 200 GHz frequency limit of radio observations. The term ‘non-thermal’ is used for radiation emitted by high energy particles whose acceleration is caused by non-thermal phenomena. It is described as being ‘continuum radiation from particles, the energy spectrum of which is not Maxwellian’ (Longair 2011).

1.1 Radiative processes

1.1.1 Thermal Radiation

Above ~ 30 GHz, radio emission from normal galaxies becomes dominated by unpolarized, thermal free-free emission as opposed to non-thermal emission (see figure 1.2). The majority of thermal free-free radiation in galaxies is produced in HII regions within the interstellar medium, which have been photoionized by massive O and B type stars within the galaxy environment (Beswick et al. 2014b). The resulting plasma causes thermal emission by means of acceleration of charged particles, particularly electrons due to their relatively low mass, as their trajectories are diverted by oppositely charged particles within the warm ionized medium (WIM) (Irfan 2014). This deflection of the trajectory causes acceleration of the particle and the resulting electromagnetic radiation has a frequency dependent on the initial energy of the emitting particle. Free-free emission has a typical brightness temperature of $\sim 10^4$ K (Derham 2000). The process is so-called free-free as it is produced by free electrons that are deflected by ions without being captured.

1.1.2 Non-Thermal Radiation

Synchrotron radiation is linearly polarized non-thermal radiation from relativistic electrons spiraling through a magnetic field whose energies are much greater than their rest mass energy, so that $\gamma = E/m_e c^2 \gg 1$ (Frank et al. 2002). Synchrotron radiation dominates radio spectra at frequencies below ~ 30 GHz, and accounts for 90% of the radio emission from normal galaxies at these frequencies (Condon 1992). Synchrotron emission in normal galaxies is predominantly caused by radio supernovae (RSNe) and their supernovae remnants (SNRs) associated with stars with masses greater than $8M_\odot$ (Bressan et al. 2002). Their shock waves propagate through the circumstellar medium at supersonic speeds (McDonald 2001) up to

$v_s \sim (0.1 - 0.3)c$ (Perez-Torres et al. 2015). The shock waves accelerate cosmic ray electrons (CREs) to the relativistic speeds required to produce synchrotron radiation within the given magnetic field of the system, and the non-thermal radio component is observed.

In the case of radio-loud AGN, non-thermal radiation is responsible for the majority of radio emission via jets and radio lobes, which are discussed in section 1.2.

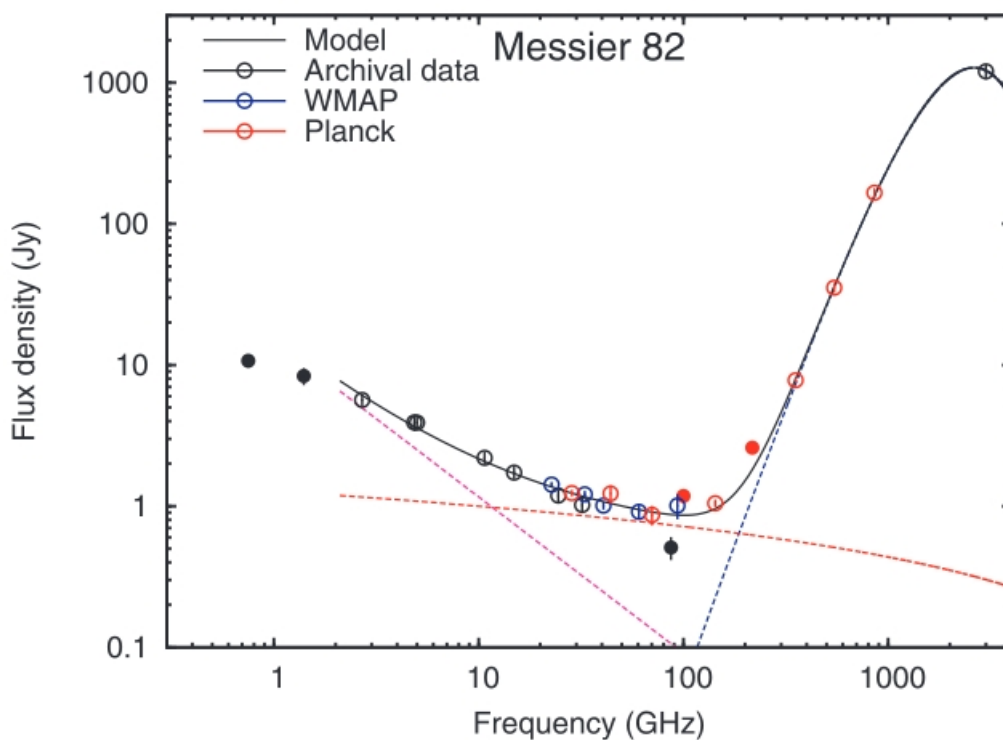


Figure 1.2: The radio and far infrared spectrum of the normal galaxy M82. The red line represents the thermal free-free emission, the pink line represents the non-thermal synchrotron emission, and the blue line shows the thermal blackbody radiation emitted by dust. The solid line represents the best fit of the observed spectrum. Blackbody emission from the thermal radiation of dust overwhelms free-free emission at a frequency of ~ 200 GHz. Image taken from Peel et al. (2011).

1.2 Galaxy Types and Sources of Radio Emission

1.2.1 Active Galaxies

Radio emission is observed in every galaxy that exhibits ongoing star formation, and is also observed in all AGN (Begelman et al. 1984). AGN are generally classified as either Seyfert galaxies, quasars, radio galaxies, blazars or Low Ionization Emission-Line Region galaxies (LINERs), which are differentiated by their observed properties over all wavelengths. Seyfert galaxies and 90-95% of quasars are so-called ‘radio-quiet’ due to the low flux observed at radio wavelengths, although they are not considered ‘radio-silent’. The optical spectral differences of each of these types of active galaxies can be seen in Figure 1.3.

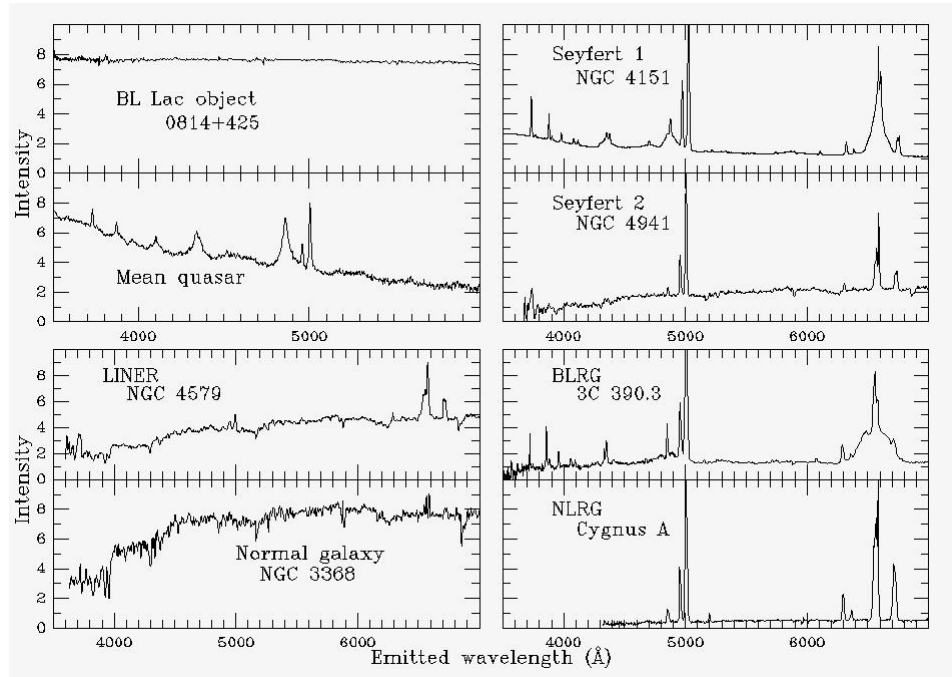


Figure 1.3: The optical spectra of AGN types showing the characteristics exhibited by different types at optical wavelengths. Image taken from Keel (2002).

Seyfert Galaxies

Seyfert galaxies are spiral galaxies that host a supermassive black hole (SMBH) and ongoing star formation in the spiral arms (Begelman et al. 1984). Seyferts are considered ‘radio-quiet’ although some radio emission is detected as a result of accretion onto the central black hole and star formation. They are classified as either type I or type II depending on the presence of both broad and narrow spectral lines (type I) or just narrow spectral lines (type II) as can be seen in Figure 1.3.

Quasars

Upon discovery, all quasars were thought to be radio-loud as their radio-quiet counterparts appear stellar in optical observations and were assumed to be such. Radio-quiet quasars are considered to be ‘high-luminosity Seyfert I galaxies’ (Begelman et al. 1984). The spectrum of a radio-quiet quasar is similar to that of Seyfert I galaxy but can be characterised by high redshift and the presence of the Lyman- α hydrogen emission line at an optical wavelength of 121.6nm at rest and a Lyman- α forest, as can be seen in Figure 1.4.

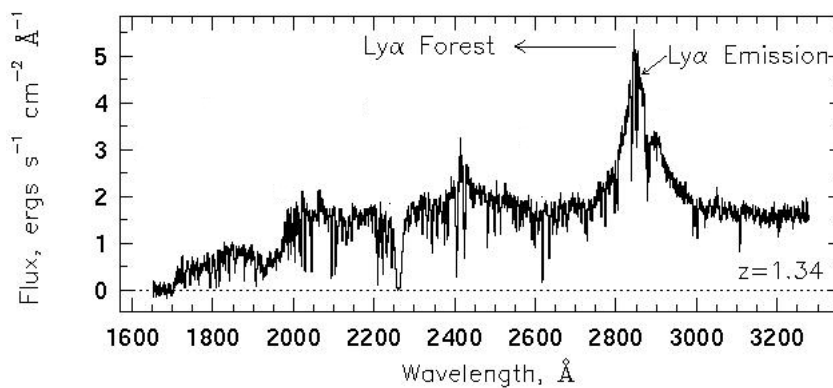


Figure 1.4: The spectrum of the quasar PKS0454+039 at a redshift of $z=1.34$. The Lyman- α hydrogen emission line and Lyman- α forest are clearly identified. Image taken from Charlton and Churchill (2000).

Quasar spectra also exhibit weak stellar absorption features and narrow lines are generally weaker in comparison to broad lines. The main visual difference in the two objects is that quasars are spatially unresolved in Palomar Sky Survey images, indicating an angular size of less than $\sim 7''$ (Peterson 1997), and quasars are typically associated with elliptical galaxies rather than spiral. Quasars also exhibit other features such as jets and radio lobes which are extremely luminous at radio wavelengths.

Radio Galaxies

Radio galaxies can either exhibit both broad and narrow lines or purely narrow lines, and are so called broad-line radio galaxies (BLRGs) or narrow-line radio galaxies (NLRGs) which are analogous of type I and II Seyferts respectively but residing within elliptical hosts rather than spiral (Peterson 1997). Radio galaxies can be classified as Fanaroff-Riley I (FRI) or Fanaroff-Riley II (FRII) depending on the luminosity and physical characteristics of the jets and radio lobes. FRI galaxies are relatively low luminosity and have bright radio jets, but with less distinguishable lobes. FRII galaxies have higher luminosities, with bright radio lobes and relatively dim jets in comparison (Fanaroff and Riley 1974). Figure 1.5 shows the FRII galaxy 3C 175.

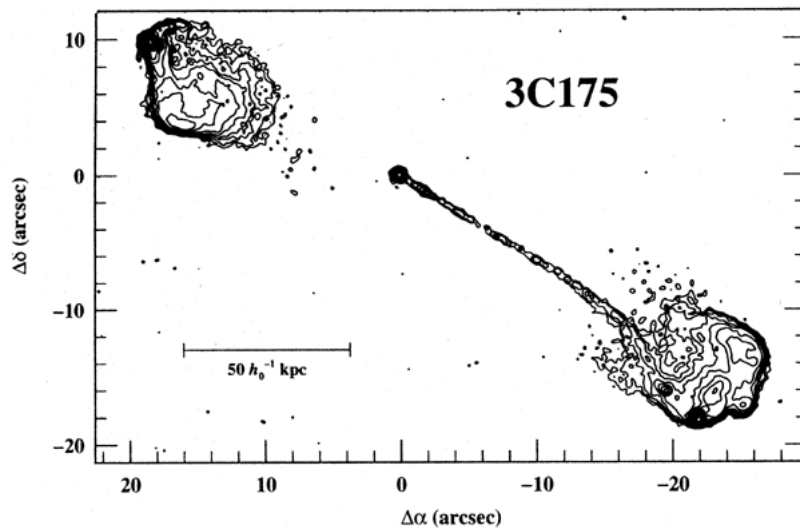


Figure 1.5: The FR II galaxy 3C 175 clearly exhibits bright radio lobes, although only one jet is visible due to the effects of relativistic beaming which is described in section 1.2.2. Image taken from Peterson (1997).

Blazars

All blazars are radio sources, and are generally classified into two groups, BL Lacertae (BL Lac) objects and Optically Violent Variables (OVVs). OVVs can vary by $\Delta m \geq 0.1$ mag over timescales as short as 24 hours (Peterson 1997) at optical wavelengths, and so were originally thought to be variable stars when they were first discovered. BL Lac objects are defined by little variation in flux across all wavelengths and indistinguishable emission or absorption lines. The light from blazars is highly polarized and the polarisation also varies in magnitude and position angle. It is thought that both OVVs and BL Lac objects have a beamed component such as a relativistic jet close to the line of sight. Blazars are thought to be quasars but viewed along the plane of the rotation axis; this is called the ‘beam model’ (Antonucci 1993).

LINERs

LINERs are Low-Ionization Nuclear Emission-Line Region galaxies whose spectra resemble that of a type II Seyfert, with the main difference being the strong presence of low-ionization emission lines such as [OI] λ 6300Å and [NII] $\lambda\lambda$ 6548,6583Å (Peterson 1997). According to Ho et al. (1994), LINERs are observed in nearly half of all spiral galaxies, making them them by far the most commonly observed active galaxy.

ULIRGs

ULIRGs are Ultra-Luminous InfraRed Galaxies, which emit a large fraction of their emission at wavelengths greater than 10 μ m. Their infrared luminosities range between $\sim 10^9 L_\odot$ and $\sim 10^{12} L_\odot$ (Lonsdale et al. 2006). The infrared emission exceeds optical emission by more than a factor of ten (Peterson, 1996), which is a result of thermal re-radiation of dust (T=100K or less) that is being heated by a hidden AGN or starburst activity.

Starburst Galaxies

Although not classified as an AGN, starburst galaxies exhibit strong star-formation activity which ‘cannot be sustained over its lifetime’ (McDonald 2001). They are characterised by very strong HII-region-type emission line spectra due to the presence of O and B stars, and emit radio emission due to the large numbers of SNRs and HII regions associated with this star formation.

1.2.2 Unification of Active Galactic Nuclei

There are numerous unification schemes that aim to unify AGN by their physical properties. To be able to do this, it is assumed that all AGN have the following properties; (i) a SMBH at the centre, (ii) an accretion disc around the SMBH, (iii) high energy gas causing spectral Doppler Broadening in type I AGN, (iv) lower energy gas that results in the narrow lines seen in type I and II AGN, (v) a dusty torus that obscures broad-line regions from the observer in the case of type II AGN (Jones and Lambourne 2004). One simple model highlights a distinction between radio-loud and radio-quiet AGN due to the presence of jets and lobes that are absent in radio-quiet AGN. This simplistic model hopes to unify radio galaxies, quasars and blazars depending on their jet and lobe characteristics, and the abundance of broad-line regions (BLRs) or narrow-line regions (NLRs), as can be seen in Figure 1.6.

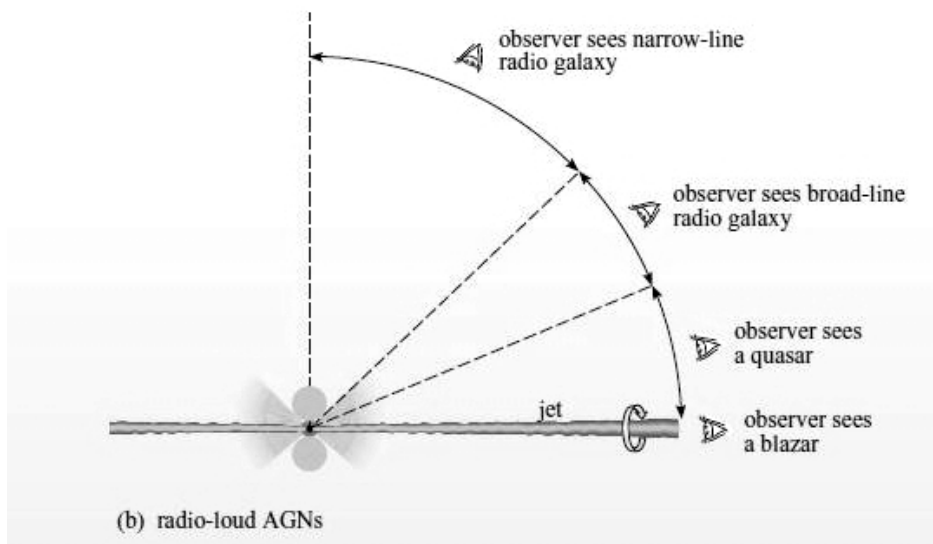


Figure 1.6: The unification model for radio-loud AGN. The central engine is surrounded by the dusty torus in which the BLR is contained, and the NLR extends from the torus. The jet can be seen parallel to the axis of rotation. Image taken from Jones and Lambourne (2004).

Between the rotation axis and around approximately $20\text{-}25^\circ$, the observer will see a radio-loud quasar with both BLRs and NLRs in its spectrum. In this situation, only one jet would be visible due to the effects of ‘relativistic beaming’. When a jet is viewed close to the line of sight, the relativistic components ‘catch up’ with the radiation travelling at the speed of light, and superluminal motion is observed whereby the jet appears to be travelling faster than the speed of light. The effect of this motion is that is that the jet becomes ‘beamed’ or ‘Doppler boosted’, resulting in a boost in the luminosity of the component facing towards the observer, and a suppression in the luminosity of the component facing away (Kellermann and Owen 1988; Jones and Lambourne 2004). Relativistic beaming of radio jets is commonly observed in quasars, hence why a quasar would be seen from this orientation. Between approximately $20\text{-}25^\circ$ and 45° from the rotation axis, the observer would see a BLRG as both the high energy and low energy gas clouds surrounding the torus would be visible as well as both jets. An observer viewing the object between 45° and 90° from the rotation axis would see a NLRG due to the fact that the BLR is obscured by the dusty torus. Both jets and lobes would also be visible in a NLRG.

1.2.3 Radio Emission from Normal Galaxies

Global Radio Emission

The majority of galaxies within our local universe are small, low luminosity types which includes low luminosity ellipticals, lenticular and dwarf elliptical galaxies with low star-formation rates (SFRs) (Gallagher 1991). Dwarf galaxies are generally defined by having an absolute magnitude of $M_B \geq -16$. The diversity of galaxies in the local universe also extends to late-type spirals, irregular galaxies and starburst galaxies which exhibit higher SFRs.

Normal galaxies with ongoing star formation have higher radio luminosities than those with lower SFRs, and so those with compact ($D \leq 1$ kpc) central

starbursts dominate at higher luminosities (Condon 1992). Central regions in interacting systems become compacted due to the gravitational effects of the interactions, and the result is the formation of massive stars and their SNe which cause thermal and non-thermal radio emission to be produced. Figure 1.7 shows the radio maps of different galaxies to demonstrate the range of radio sizes and morphologies that can be observed in normal galaxies.

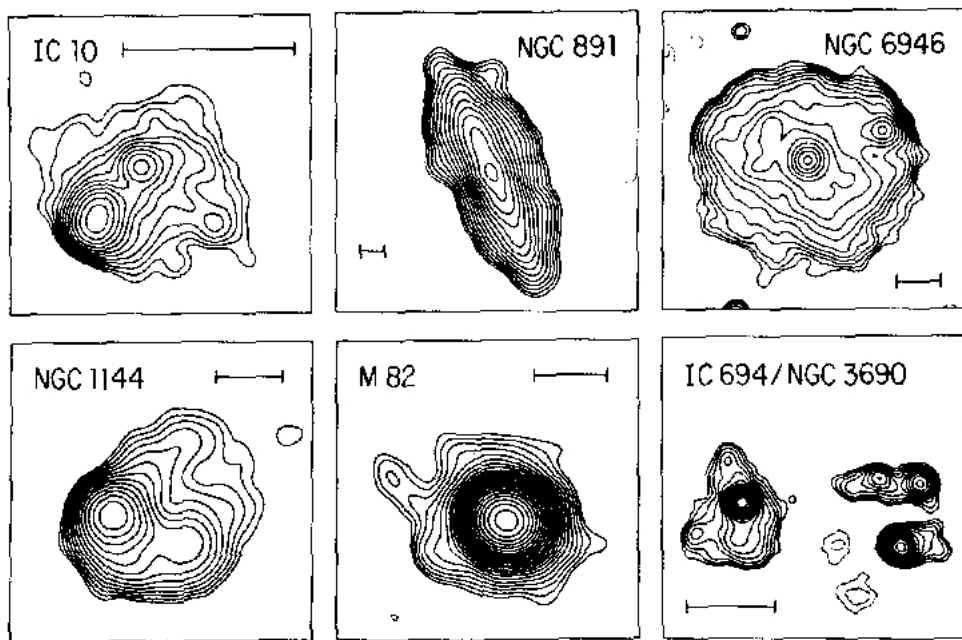


Figure 1.7: Contour maps of a sample of normal galaxies exhibiting a range of morphologies, sizes and luminosities. These galaxies have been observed by the VLA at 1.4 GHz, and the bars are $2 h^{-1} \text{ kpc}$ long. Image taken from Condon (1992).

Jurusik and Chyzy (2014) modelled the low frequency radio emission of a normal galaxy similar to the Milky Way and produced the spectra in Figure 1.8. It represents the global radio emission from the modelled galaxy as opposed to small-scale emission.

1.2. GALAXY TYPES AND SOURCES OF RADIO EMISSION

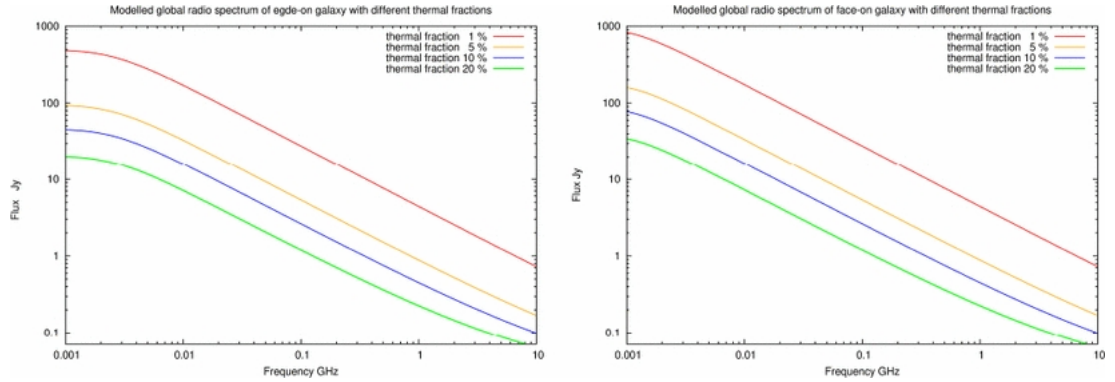


Figure 1.8: These spectra show the modelled global radio emission from a normal galaxy with thermal fractions of 1%, 5%, 10% and 20%. The left panel shows an edge-on galaxy and the right panel shows a face-on galaxy. Image taken from Jurusik and Chyzy (2014).

Small-Scale Radio Emission

When young, massive OB type stars begin to form and evolve, the high flux of UV radiation that is produced is responsible for the emission of free-free radiation. This UV light has a profound effect on the interstellar medium and photoionizes the surrounding material causing regions of ionized hydrogen (Hoare et al. 2007). This causes the compact radio emission that is observed in these regions via free-free radiation, as discussed in section 1.1.1. Compact emission is also observed from supernovae, which are generally classified into two main groups. Type I and type II are differentiated by the presence or lack of hydrogen in their spectra. Type I supernovae are associated with older stars and are characterised by a lack of hydrogen Balmer lines in their spectra and a gradual, predictable decline in luminosity. Type II supernovae are associated with younger stars, and they display an abundance of hydrogen Balmer lines with an irregularly declining luminosity (Phillips 2002).

Type I SNe are further classified as Ia, Ib or Ic depending on the abundance of elements within their spectra. Type Ia SNe are the result of the thermonuclear explosion accredited to degenerate white dwarfs, and they exhibit strong Si II

lines in their spectra. Types Ib and Ic are formed from the core collapse of massive stars $> 8M_{\odot}$ (McDonald 2001). Type Ib exhibit moderately strong He I lines and type Ic contain neither Si II nor He I emission lines (Filippenko 1997). Type II supernovae are also the result of the core collapse of a massive star, and can be further classified as either II-L or II-P depending on the shape of their optical light curve. Type II-P show a plateau feature in the light curve whereas II-L SNe have a linearly declining light curve (McDonald 2001).

In the case of radio astronomy, SNe are generally classified depending on the progenitor system that created them. Type Ia SNe are the result of a thermonuclear explosion from a degenerate white dwarf and can be called thermonuclear SNe. Types Ib/c and type II result from the core collapse of massive stars and are so called core-collapse SNe (CCSNe). Radio emission has not yet been observed from thermonuclear SNe (Beswick 2006; Perez-Torres et al. 2015) but CCSNe are often considered to be radio loud. In the case of Type I CCSNe, the radio turn-on/turn-off is very rapid and the spectrum is typically steep ($\alpha < -1$) with a 5GHz peak before the optical maximum (Beswick 2006). Type II CCSNe have longer turn-on timescales and are generally longer lived. They have a relatively flat radio spectrum ($\alpha > -1$) with a 5GHz peak after optical maximum (Weiler 1989; Beswick 2006). Radio emission from supernovae is predominantly non-thermal synchrotron radiation which is produced as shock waves propagate through the circumstellar material (CSM) produced by the mass-loss process from the progenitor system (Panagia 2006). A cartoon illustrating the components of a CCSNe can be seen in Figure 1.9.

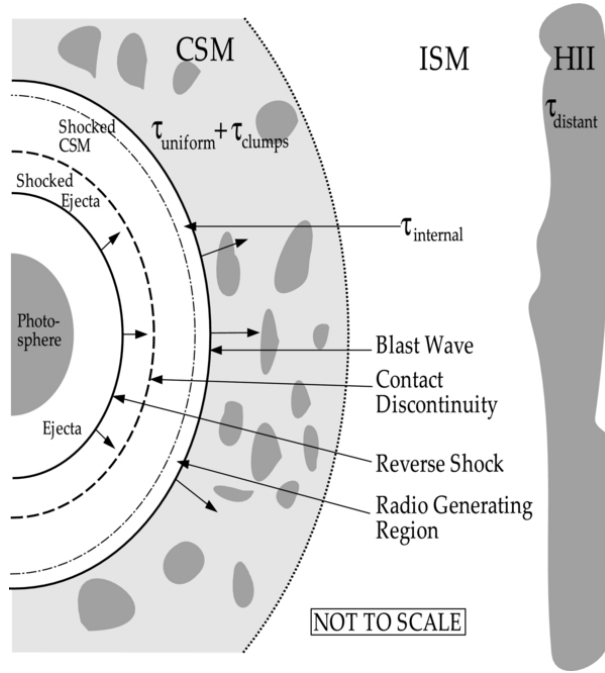


Figure 1.9: A cartoon of the main components of a SNe. The image shows the ‘radio generating region’ near the blast wave, as well as the other shocked and unshocked components of SNe and the ionized HII region. Image taken from Weiler et al. (2001)

The point at which a SN becomes a SNR has been described by Fesen (2001) as the point when non-thermal emission and UV/optical flux fall below that which is generated by the interaction with the surrounding material, or that of the compact stellar remnant.

1.2.4 Radio Emission from Active Galactic Nuclei

In the case of both extended and compact sources in AGN, synchrotron is the dominant radiation mechanism that accounts for most of the observed radio emission. The extended sources such as jets and lobes have relatively low luminosity at optical wavelengths whereas compact sources often have optical counterparts with high luminosities. The spectra of compact sources is generally flat with $\alpha \leq 0.5$, whereas the spectrum of an extended source is steeper (Peterson 1997).

Extended Sources

Jets are extended linear features observed from both radio-loud quasars and radio galaxies. These jets are relativistic and can project up to several hundred kiloparsecs from the nucleus to the extended radio lobes (Jones and Lambourne 2004). It is generally accepted that jets are aligned with the rotation axis of an AGN, but the production mechanisms are not yet fully understood. It is clear that quasars and the more powerful radio galaxies only appear to have one jet, and this is thought to be due to the process of relativistic beaming. Jets are strong emitters of synchrotron radiation, and the emitted light is highly polarized.

Radio lobes are exhibited by FR II galaxies and are usually symmetrically dispersed on either side of the galaxy and aligned with the rotation axis. They can stretch into the intergalactic medium as far as megaparsecs from the galaxy itself (Peterson 1997). ‘Hot spots’ are found at the outer edges of lobes in powerful FR II galaxies which are characterised by a high surface brightness. Intense synchrotron emission is observed from these hot spots as a result of the dissipation of kinetic energy from the relativistic jets that feed the lobes (Meisenheimer et al. 1997).

Compact Sources

The argument for SMBHs at the centres of AGN is strong as they are the only object that would generate $\geq 10^{61}$ ergs within the nucleus that can then be transferred in the form of jets. SMBHs would account for the luminosity, compactness and overall stability of active nuclei (Begelman et al. 1984). SMBHs are stable enough to power an AGN by accretion given an accretion rate of $\sim 1\text{--}100 M_{\odot}\text{yr}^{-1}$ for the brightest quasars (Frank et al. 2002).

1.3 The Far Infrared-Radio Correlation

Thermal and non-thermal radio continuum observations can provide excellent tracers of star formation in galaxies due to the nature of the objects that emit via free-free and synchrotron emission. There is a strong relationship between the radio continuum at 1.4 GHz and far infrared (FIR) light at $\lambda=10\ \mu\text{m}$ over a wide range of galaxy types and redshifts (Condon 1992; Randriamampandry et al. 2015). AGN cannot be included in the FIR-Radio correlation as the non-thermal component is not indicative of star formation, but is instead attributed mostly to jets and radio lobes. Figure 1.10 clearly shows the FIR-radio correlation.

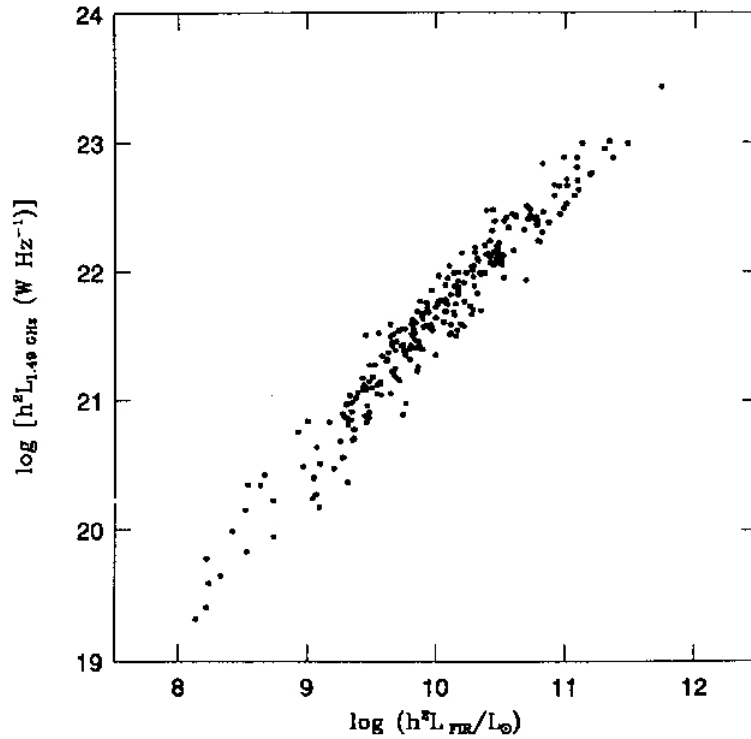


Figure 1.10: The FIR-radio correlation is shown with FIR luminosity on the x-axis and radio luminosity on the y-axis. The objects have been observed at both $\lambda=60\ \mu\text{m}$ and 1.49 GHz and do not contain an active nucleus. Image taken from Condon (1992).

The correlation is ultimately driven by the star formation within the galaxy. The radio continuum at 1.4 GHz is the result of RSNe and SNRs by means

of synchrotron radiation, as is discussed in section 1.1.2. The FIR emission is radiated from dusty HII regions, where ultraviolet light emitted by massive young stars is absorbed and re-radiated at infrared wavelengths by dust.

There is some discussion of the reliability of the FIR-radio correlation due to the nature of galaxies in the local universe. The case proposed by Condon (1992) makes the assumption that all galaxies within the sample act as a calorimeter. The calorimeter theory was first proposed by Völk (1989) and states that all CREs from SNe will lose their energy in the form of synchrotron emission before escaping a galaxy. Galaxies that exhibit this phenomenon are called ‘electron calorimeters’. The theory also states that calorimetric galaxies must be optically thick to UV light from young stars which is re-radiated by dust at infrared wavelengths. These are called ‘UV calorimeters’. If a galaxy is an electron and UV calorimeter, then the total starlight produced is directly proportional to the total energy of the CREs; the FIR-radio correlation. The main issue stems from the fact that not all galaxies in the local universe abide by the calorimeter theory, and the assumption that the energy expelled from SNe will remain constant is ‘naive’ (Lacki et al. 2010).

The observed synchrotron spectral index for normal galaxies is $\alpha \sim 0.7-0.8$. If electron calorimetry is true for normal galaxies, then the synchrotron cooling timescale is much less than the escape timescale in order for the total CRE energy to be dissipated. This would induce a steep spectral index of $\alpha \sim 1.0-1.2$, which is steeper than observed. This shows that, contrary to what the calorimeter theory says, CREs escape the galaxy before losing all of their energy. In this case, normal galaxies are considered to be ‘leaky boxes’. Lisenfeld and Völk (2000) suggest that the observed flattening results from the presence of SNRs, although other non-calorimetric models have since been proposed (Helou and Bicay 1993; Niklas and Beck 1997) that use other methods to maintain the tightness of the FIR-R correlation (Lacki et al. 2010).

The most widely accepted current theory was written by Lacki et al. (2010)

1.3. THE FAR INFRARED-RADIO CORRELATION

and concludes that the calorimetric model does not hold true for all normal galaxies, but can be assumed to be true for most starburst galaxies. They find that as well as calorimetry, additional factors such as the relative fractions of primary and secondary CREs, inverse Compton cooling and ionisation must be considered to gain a tight FIR-radio correlation for normal galaxies.

1.4 Radio Observations of Compact Objects

To be able to identify sources of radio emission in nearby galaxies, both the spectra and radio maps of the compact sources must be considered. Figure 1.11 shows the 5 GHz MERLIN and 15 GHz VLA radio maps for sources within M82. Figure 1.12 shows the spectra of a selection of radio sources in the same galaxy.

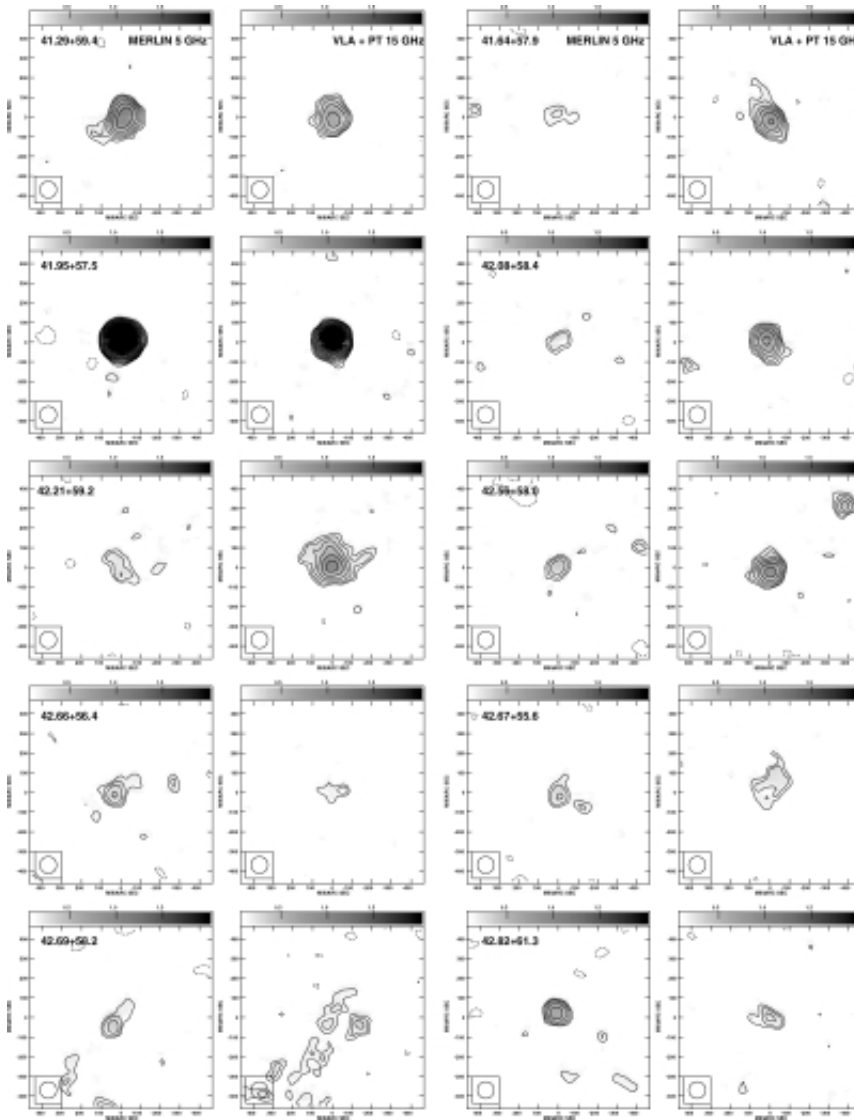


Figure 1.11: 5 GHz MERLIN and 15 GHz VLA observations of compact radio sources within M82. Image taken from McDonald et al. (2002).

1.4. RADIO OBSERVATIONS OF COMPACT OBJECTS

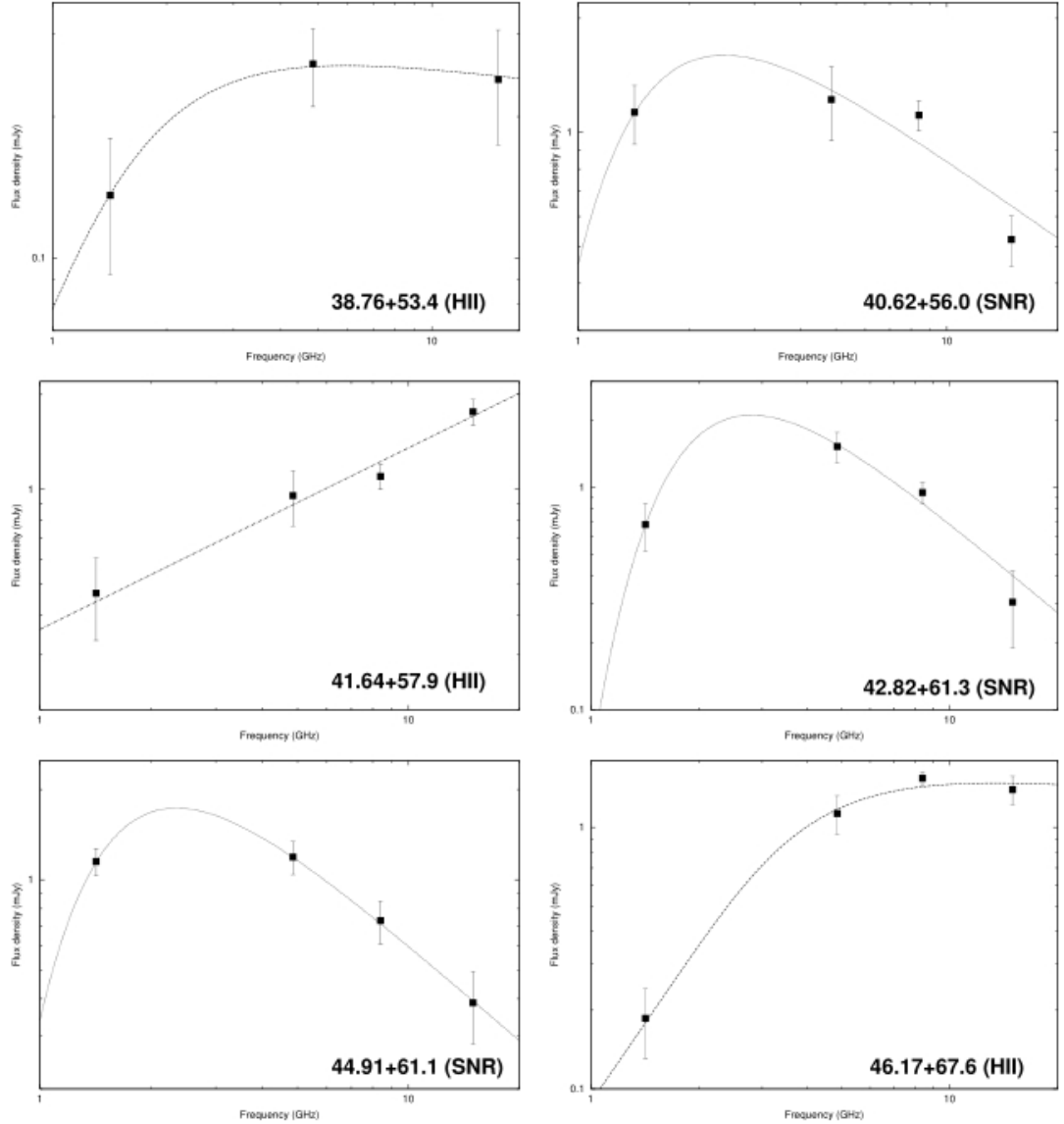


Figure 1.12: The radio continuum spectra of six compact sources in M82. They are classified and labelled depending on the thermal and non-thermal components of the spectra. The dashed line is the best fit of the flux densities measured from low-resolution maps, which enables identification of the compact source. Image taken from McDonald et al. (2002).

By looking at the spectral index of the sources it is possible to determine the presence of either thermal or non-thermal emission. The type of emission indi-

cates the type of emitting region and the radio sources can then be distinguished.

As well as the SNe, SNRs and HII regions shown in Figures 1.11 and 1.12, radio-loud AGN such as quasars, radio galaxies and blazars can also be classified by comparing the radio observations and spectral indices of the emitting regions.

1.5 LeMMINGs

One of the current projects looking at radio emission from galaxies is the LeMMINGs project, which is the Legacy e-MERLIN Multi-Band Imaging of Nearby Galaxies survey. The project utilises the high resolution of the e-MERLIN interferometer to study a selection of galaxies in the nearby universe. The project contains a sample of 286 galaxies, 280 of which are selected from the Palomar Bright Galaxies Survey. It is hoped that the sample size is sufficient to represent galaxies of a wide range of luminosities, scales and galaxy types (Beswick and McHardy 2008). The observation time for the sample galaxies at L-band (1.2 - 1.7 GHz) and C-band (4 - 8 GHz) can be seen in Table 1.1.

Tier	Band	Number of Targets	Sensitivity ($\mu\text{Jy/bm}$)	Luminosity (W/Hz)	Time on Source (hours)
Shallow	L	280	38	1.8×10^{18}	0.8
Shallow	C	280	15	7.2×10^{17}	0.8
Deep	L	6	8	7.5×10^{16}	4.8
Deep	C	6	3	2.8×10^{16}	4.8

Table 1.1: The observation schedule of the LeMMINGs project with the expected observational capabilities. Table taken from Beswick et al. (2014a).

1.5.1 Scientific Goals

The core scientific themes of the LeMMINGs project are to study both SF and accretion as well as and the fuelling mechanisms of these phenomena. The key scientific goals of the LeMMINGs project are as follows;

(i) To measure star-formation activity in a wide variety of galaxies in the nearby Universe, as selected by the Palomar Sky Survey. The objects within these galaxies such as RSNe, SNR and HII regions can be used as direct tracers of star-formation.

(ii) AGN activity and jet structure in AGN of all types will be correlated with levels of ongoing star-formation to determine any relationship between the two.

(iii) The cold interstellar medium (ISM) can be imaged on parsec scales using HI absorption and maser emission, which will enable the analysis of the content and composition of cold gas in the nuclear regions of galaxies, as well as its movement within the galaxy. Research of this type has not yet been done on this scale, and these observations will be available before the SKA is fully operational.

1.5.2 LeMMINGs Galaxy Sample

The galaxies included within the LeMMINGs sample can be seen in a sky plot in Figure 1.13.

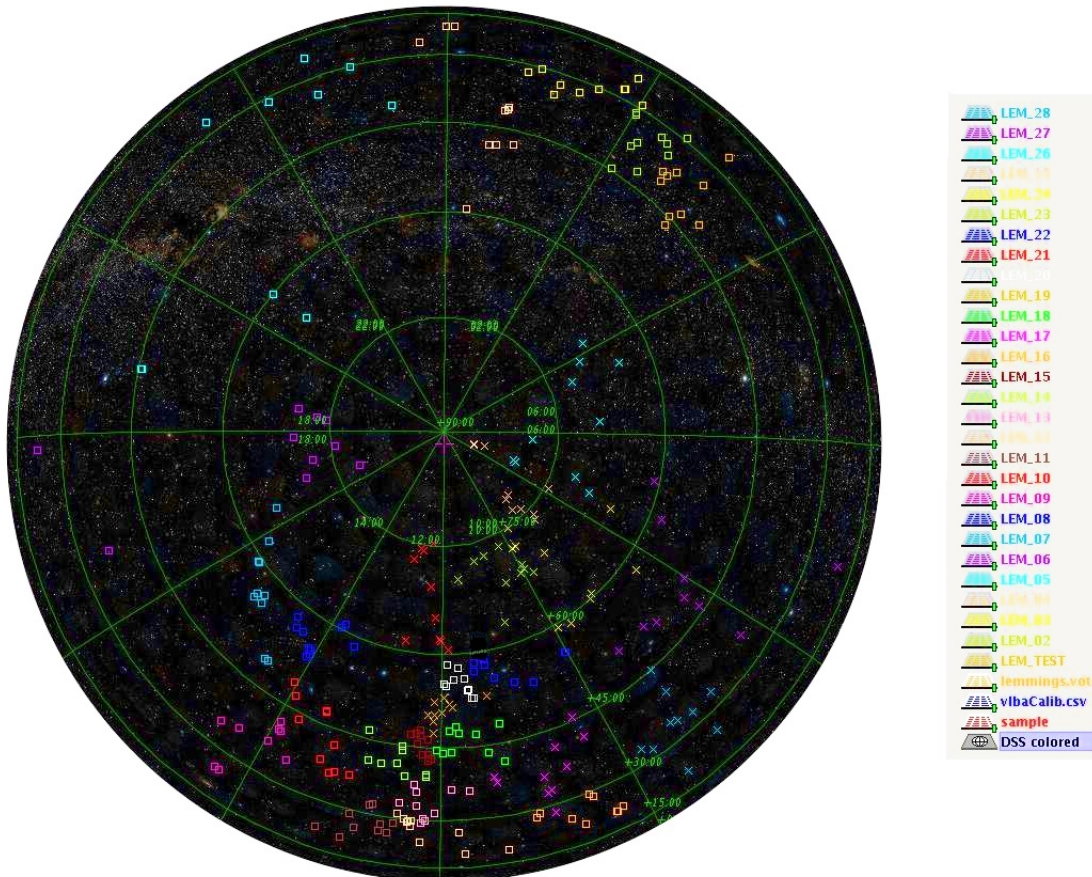


Figure 1.13: A sky plot of the LeMMINGs galaxy sample including the 280 galaxies selected from the Palomar Sky Survey. The different colours represent different blocks of observations, as can be seen by the legend, which each include 10 galaxies. Image taken from Argo (2014).

At this time, shallow tier observations have been made of around 130 sources which make up 13 of the LeMMINGs observation blocks. 5 blocks have been observed at both L and C-bands, 7 have been observed at L-band and one block

has been observed at C-band. By observing at both frequency bands it is hoped that the observations can be used together to gain a greater understanding of the processes occurring within the galaxies. These data will also be used in conjunction with observations at other wavelengths using data from infrared, optical and X-ray telescopes to obtain a better understanding of the sources over a large selection of wavelengths.

1.6 Scientific Goals of this Thesis

The purpose of this thesis is to utilise the high resolution of the e-MERLIN array to study star formation in a small sub-sample of ten target galaxies from the LeMMINGs project sample. Wide-field images will be produced from the observations to identify any compact objects or AGN activity within the target galaxies and the surrounding field, and we will use these objects to gain star formation and radio supernovae rates for each target. Chapter 2 gives an introduction to radio interferometry and the different ways in which images can be produced from radio observations. Chapter 3 presents images that have been produced and gives observed values for each detected object, and Chapter 4 discusses these results with respect to previous studies of each galaxy. The thesis is then summarised in Chapter 5.

Chapter 2

Radio Interferometry

2.1 Interferometry

This chapter gives a brief introduction to radio interferometry and the required techniques to produce images from interferometric data. For a more detailed description of radio interferometry, note the works of Thompson (1999) and Thompson et al. (2007) on which this chapter is based.

Astronomy requires high resolution observations to produce images of objects in the universe with small angular sizes, but the angular resolution of a single radio telescope is limited by

$$\Theta = \frac{\lambda}{D} \quad (2.1)$$

where Θ is the angular resolution in radians, λ is the wavelength in metres and D is the diameter of the dish, also in metres.

By using two or more antennas to observe simultaneously, it is possible to extend this limit to

$$\Theta = \frac{\lambda}{B} \quad (2.2)$$

where B is the length of the baseline between the telescopes in metres. This

entails that the largest baseline of an interferometric array is equal to a single, large antenna of diameter B by means of aperture synthesis which is discussed in section 2.1.2.

Figure 2.1 shows a simple two-element interferometer in which both dishes are pointed at the same source.

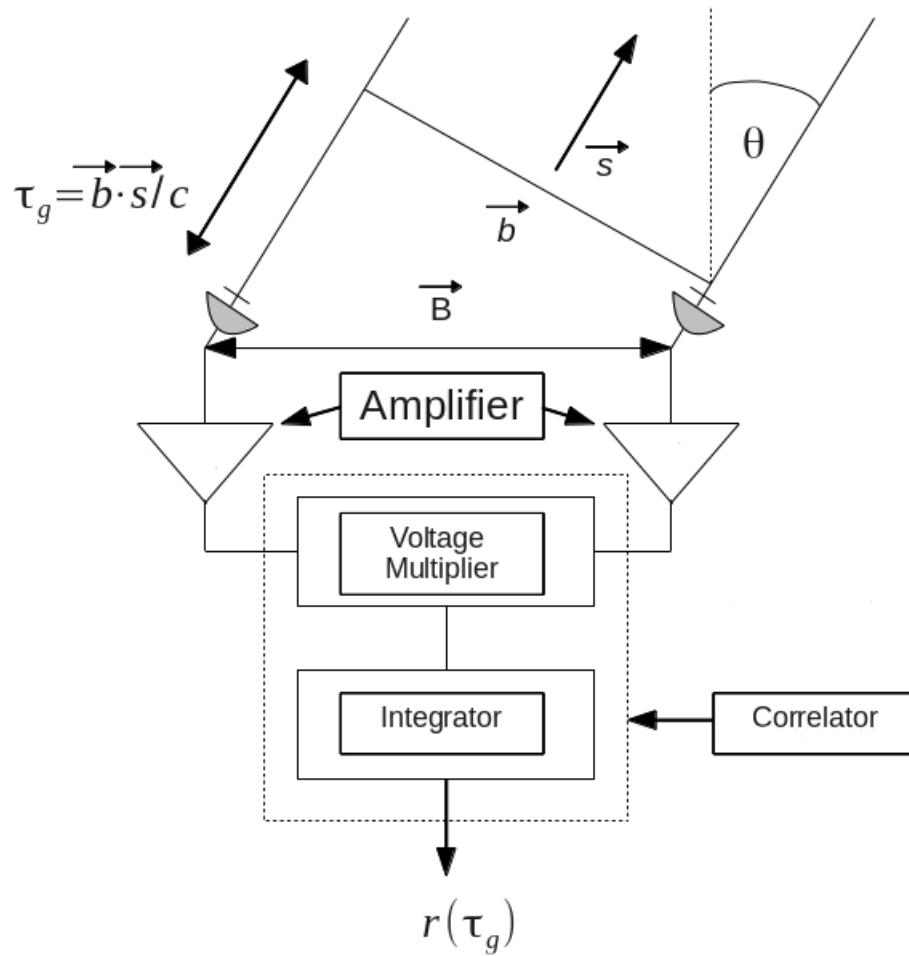


Figure 2.1: A simplified diagram of a two-element interferometer.

In this diagram, B is the baseline vector, b is the projected baseline vector, s is the directional vector to the source and c is the velocity of the incoming photons. τ_g is the geometric time delay measured by the array as a result of the

source and telescope position.

Consider these two antennas placed on a flat surface of the Earth which is not rotating. If the observed source is located at the zenith, the coherence of the antennas is only measured as a function of the baseline distance. If, however, the source is not located at the zenith, then the wave-fronts from the source will not reach each antenna simultaneously, and therefore the delay in the signal must be accounted for (Thompson 1999).

The correlator system combines these signals coherently to produce an output voltage in which the delays have been subtracted, and a visibility function can be obtained. The system is composed of a voltage multiplier and an integrator which is a time averaging circuit. If the incoming voltages received by the antenna are $V_1(t)$ and $V_2(t)$, then the correlator provides

$$\langle V_1(t)V_2(t) \rangle \quad (2.3)$$

where the pointed brackets indicate time averaging. The voltages can be represented as Fourier components of the frequency via $V_1(t) = \nu_1 \cos 2\pi\nu(t - \tau_g)$ and $V_2(t) = \nu_2 \cos 2\pi\nu t$. The corresponding output from the correlator system is therefore

$$r(\tau_g) = \nu_1 \nu_2 \cos(2\pi\nu\tau_g) \quad (2.4)$$

where $r(\tau_g)$ is the output as seen in Figure 2.1 and is known as the visibility function. This visibility function is the quantity that all interferometer systems measure, and is the spatial coherence function of the incoming wave field (Saha 2011). It is not the same at different co-ordinates of the Fourier transformed sky due to the brightness distribution of the target source which varies with respect to the Fourier co-ordinates.

If σ is the offset of a source from the phase reference centre, it is possible to measure the intensity, I , as seen from this offset point via the basic equation

$$I = e^{ik\bar{B}\cdot\hat{s}} \int I_0(\bar{\sigma}) e^{ik\bar{b}\cdot\bar{\sigma}} d\bar{\sigma} \quad (2.5)$$

where $I = e^{ik\bar{B}\cdot\hat{s}}$ is the geometry term and $I_0(\bar{\sigma})e^{ik\bar{b}\cdot\bar{\sigma}}d\bar{\sigma}$ is the source term. The source term represents the fringe visibilities from the source which are later used to produce an image.

2.1.1 The (u,v) Plane

A single antenna measures the brightness of a source as a function of the plane of the sky, $I(x, y)$. When two or more antennas are connected in the form of an interferometer, the baseline projected onto a plane perpendicular to the line of sight has the co-ordinates u and v . This is therefore called the (u, v) plane ($I'(u, v)$) which is the Fourier transform of the (x, y) plane, hence $I'(u, v) = FT(I(x, y))$.

The spacial coherence as a function of u and v , $S(u, v)$, can be obtained by multiplying the Fourier transform of the (x, y) brightness distribution with the (u, v) sampling function, which can be seen by

$$V(u, v) = I'(u, v) \times S(u, v) \quad (2.6)$$

where $S(u, v)$ is the sampling function. $S(u, v)$ describes the sampling of the spatial coherence function as measured by the interferometer, and values of $S(u, v)$ are zero where no data have been taken. The convolution theorem can be used to convert the spacial coherence function to the (x, y) plane via

$$I^D(x, y) = I(x, y) * B(x, y) \quad (2.7)$$

where I^D is the inverse-Fourier transform of the data (the ‘dirty map’) and $B(x, y)$ is the inverse-Fourier transform of the sampling function, known as the point-spread function or ‘dirty beam’.

2.1.2 Aperture Synthesis

The purpose of aperture synthesis aims to fill in the ‘gaps’ in the (u,v) plane where the values for the sampling function are zero. The number of baselines of an interferometer is given by $N(N-1)/2$ where N is the number of telescopes. If the number of baselines is sufficient to cover a large area of the (u,v) plane then it is possible to image the source. When the (u,v) plane is under-sampled, high sidelobes become apparent in the dirty beam where there are no visibilities. Better (u,v) coverage reduces the sidelobes and produces images with a higher signal to noise ratio.

Earth-rotation synthesis utilizes the rotation of the Earth with respect to the target source to ensure a good (u,v) coverage for imaging. As the orientation of the baseline is changed with the Earth’s rotation, the co-ordinates of u and v also rotate through the plane and a greater coverage is achieved without moving the antennas individually.

As well as Earth-rotation synthesis, it is possible to sample more of the (u,v) plane by changing the frequency relative to time by means of multi-frequency synthesis, which was first theorised by Conway et al. (1990). Figure 2.2 shows the (u,v) coverage of the target source NGC 7817 at a single frequency of 1.7026 GHz. There is little sampling of the (u,v) plane which results in high sidelobes in the dirty beam and therefore more noise. Figure 2.3 shows the same source at a range of frequencies between 1.25 and 1.71 GHz with more of the (u,v) plane being sampled.

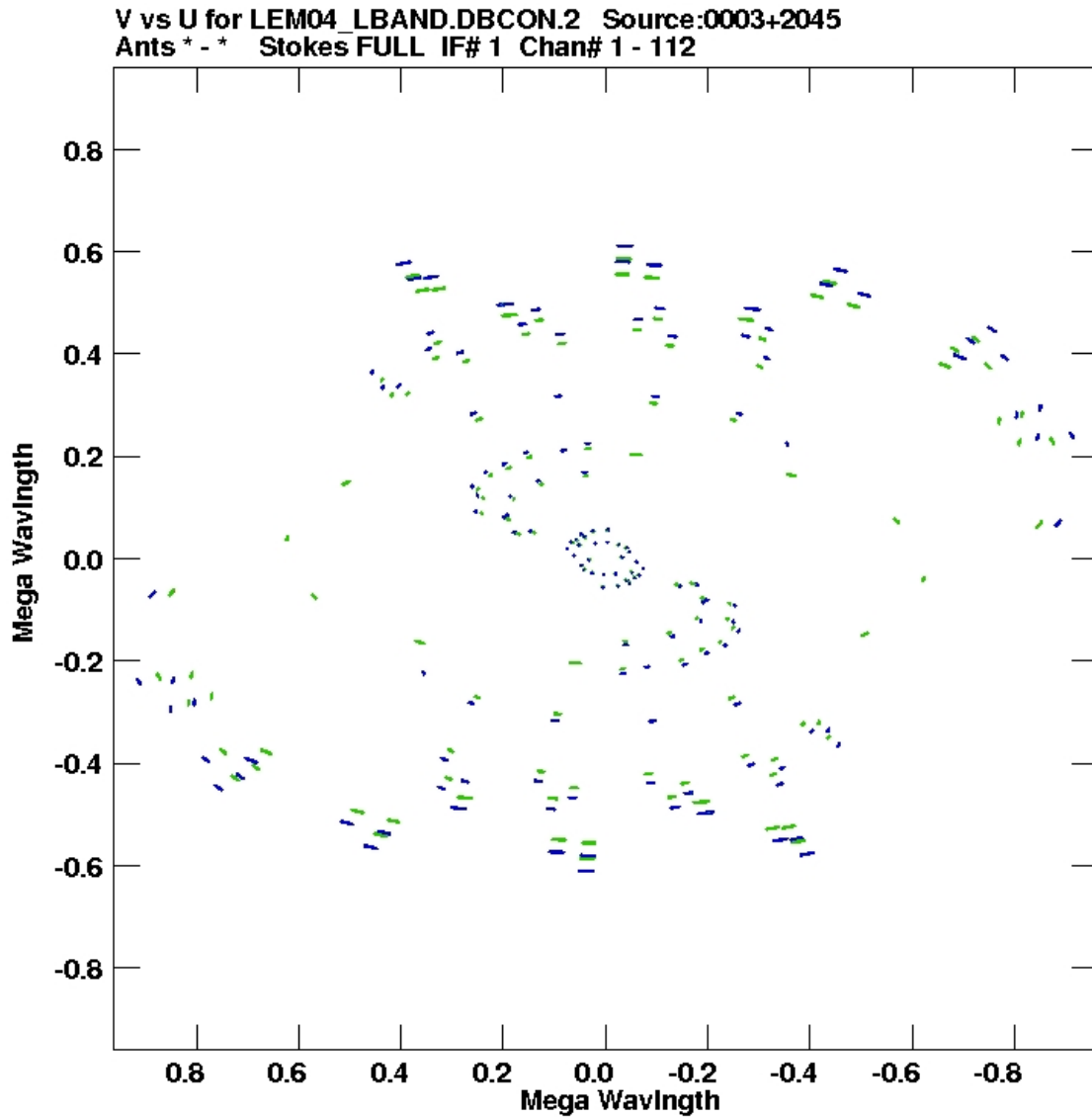


Figure 2.2: UV coverage of the target source NGC 7817 using IF 1 with a width of 64 MHz. The mean frequency of this IF is 1.7026 GHz. Note that these observations have been taken in a ‘snapshot mode’ with multiple observation cuts in order to cover a wide range of observable hour angles.

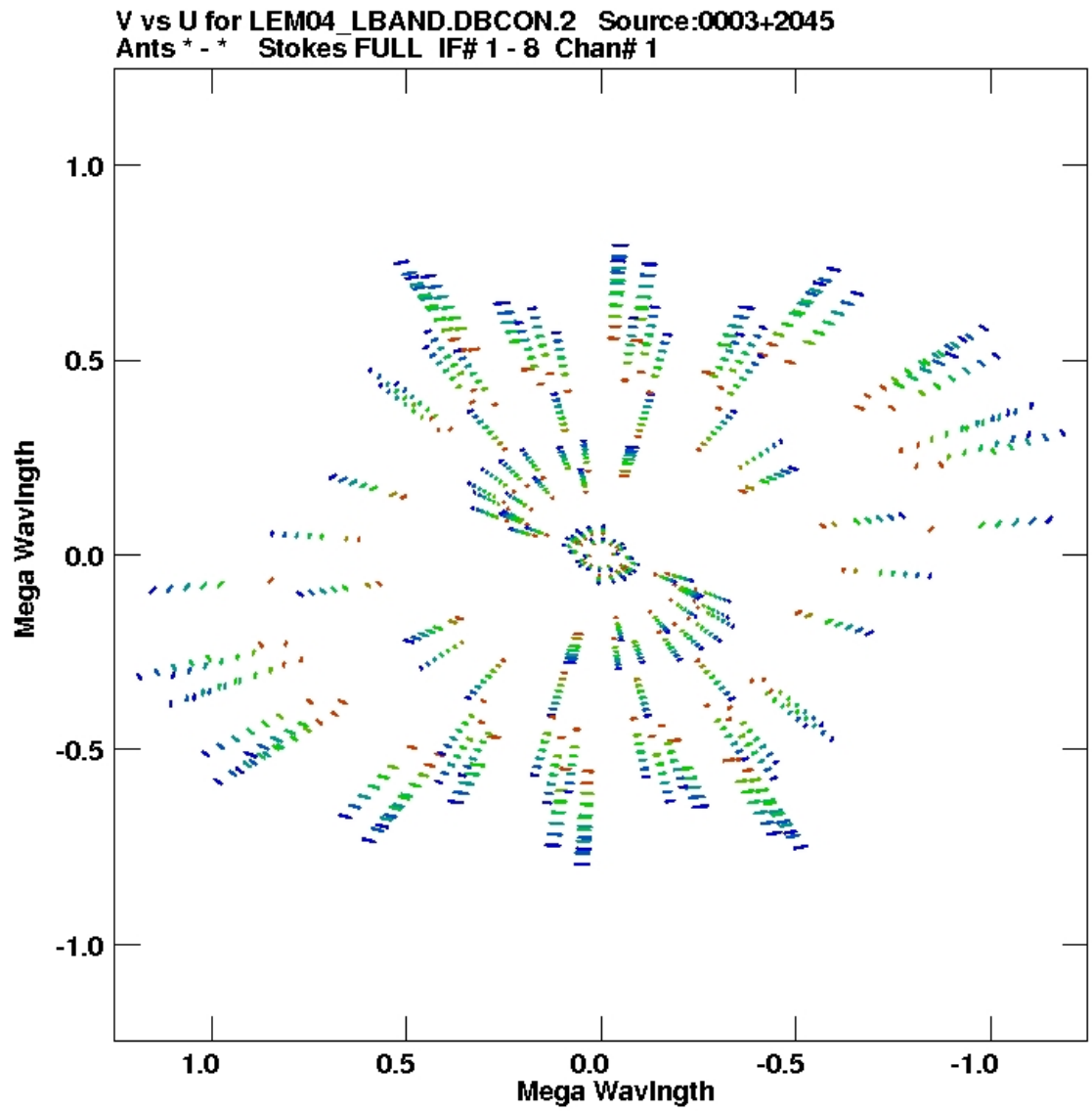


Figure 2.3: UV coverage of the target source NGC 7817 with continuous coverage between 1.25 GHz and 1.71 GHz.

2.1.3 Antenna Weighting

Weighting an antenna allows the amplification of a signal received at an antenna by an amount depending on its sensitivity. In the case of e-MERLIN, sensitive baselines are weighted up and less sensitive baselines are weighted down which can make a difference of a factor of two on the noise levels. Weighting is usually done after the calibration process so that the less sensitive antennas are included.

2.1.4 Deconvolution Methods

CLEAN

The CLEAN algorithm was developed by Högbom (1974) to image the true brightness distribution of the source from the dirty map (McDonald 2001) and is the most commonly used method to produce images from interferometric data. The process of CLEANing involves finding areas of the dirty map with the highest flux density and iteratively removing them from the dirty map to be stored as ‘CLEAN components’, noting the location that they are removed from. A model of the brightness distribution is produced via this method. After the CLEAN components have been removed, the resulting map is called the ‘residual map’ in which the flux density is replaced after convolving the CLEAN components with the ‘CLEAN beam’. Due to the under-sampling of the (u,v) plane, some areas of the brightness distribution are missed and therefore not all of this distribution can be imaged using the CLEAN algorithm. The quality of images is also hindered by ‘resolving out’ the sources, which is a result of too few short baselines. The shortest baselines of an interferometer limit the scale of the structure which can be removed, and a lack of short baselines will mean that not all flux density from a source can be detected (McDonald 2001).

The CLEAN algorithm also makes the assumption that the source is composed of a collection of point sources in an otherwise empty field of view. For a field with predominantly isolated point sources, this is a fair assumption to make. But

for a source with extended features, the algorithm becomes confused and the resulting images have high sidelobes. To overcome this problem, it is possible to estimate the area over which the flux is present in the residual map, and remove the feature of the corresponding area rather than removing the peak. Another way to alter the beam is to introduce artificial delta functions to the middle of the main beam which suppresses the sidelobes and reduce stripes in the final image (Steer et al. 1984).

Maximum Entropy Method

The Maximum Entropy Method (MEM) was developed by Ables (1974) to restore a spectrum from the partially known Fourier components to enable the suppression of sidelobes and improve resolution in interferometric imaging (Nityananda and Narayan 1982). The CLEAN algorithm is a procedural convolution method and therefore cannot be described by a simple mathematical formula. The MEM, however, is not procedural and the final image is the most probable image consistent with the data (Narayan and Nityananda 1986; Cornwell and Bridle 1996). The method requires a ‘default’ image which is often a low resolution image of the same source, which incorporates a priori knowledge of the object. The default should be flat with a total flux density equal to that specified during the deconvolution process (Cornwell and Bridle 1996). The most prominent issue with this deconvolution method is that there are an infinite number of solutions, and it is not always simple to identify which solution is most consistent with the data and has maximum entropy (Honma et al. 2014). When the entropy is maximised, a positive image is produced with a compressed range in pixel values which ultimately produces a ‘smooth’ image (Cornwell and Bridle 1996). Unlike the CLEAN algorithm which is most suited for imaging point sources, MEM is beneficial in the imaging of extended emission.

Compressed Sensing Techniques

The Shannon-Nyquist theorem implies the assumption that the signal will be sampled at a rate at least twice the observing bandwidth to ensure the complete signal is sampled. The compressed sensing theorem relies instead on the assumption that the signal vector exhibits ‘sparse representation’, and relies on the basis that signals from astronomical sources are often ‘sparse’ or ‘compressible’. The term ‘sparse’ implies that a signal contains a small number of non-zero elements, and the term ‘compressible’ describes a signal which contains few *significant* elements (i.e. a large number of the values are negligible) (Wiaux et al. 2009).

The compressed sensing and MEM techniques are alternative methods by which radio images can be produced from the data. For the purposes of this thesis, the CLEAN method was used as it is better suited to the data in which we will expect to primarily detect compact sources rather than extended emission.

2.1.5 Image Weighting

Weighting functions are used during the imaging process to change the effective shape of the beam and sidelobe level. The weighting functions are proportional to the number of (u,v) measurements in a gridded cell. ‘Natural’ weighting results in a lower angular resolution but the signal-to-noise ratio is improved, making it a better function with which to image fainter, low surface brightness sources. ‘Uniform’ weighting is higher resolution and therefore is less sensitive to extended emission. It minimizes the minimum point-spread function sidelobe levels (Yatawatta 2014), but decreases the signal-to-noise ratio. The ‘robust’ weighting method was developed by Briggs (1995) to provide an intermediate weighting that balances the resolution and sensitivity. At a robust level of 0, the signal-to-noise ratio is greatly improved with little cost to the resolution. A higher robustness level results in more natural weighting, and a lower level provides a

more uniform weighting scheme.

2.1.6 Wide-Field Imaging and Limitations

Wide-field imaging is a beneficial technique to obtain as much information about a field as possible by imaging a large area of the sky whilst maintaining the high resolution of observations. There are, however, a number of restrictions that arise when using wide-field imaging techniques.

Firstly, the field of view (FOV) is limited by the primary beam of the individual antennas. For the 25 m antennas included in the e-MERLIN array, the primary beam (and therefore FOV) is limited to approximately 27.5 arcminutes at L-band using Equation 2.1.

More restrictive limitations to the FOV are the occurrence of image aberrations which are a result of the observing bandwidth or time resolution, and the smearing effects these have on the observations.

Both time and bandwidth smearing act to distort the image of a source by spreading out its flux density over a large size. The magnitude of these effects are proportional to the source's angle and distance from the phase reference centre of the data.

Bandwidth smearing is apparent in the radial direction of the (u,v) plane. Although wide bandwidths are advantageous as they increase the sensitivity of observations, the FOV is limited if all frequency information is isolated in to one channel with respect to bandwidth smearing. This can be seen in the following equation;

$$\frac{\Delta\nu}{\nu} \ll \frac{\theta_b}{\theta_{FOV}}, \quad (2.8)$$

where $\Delta\nu$ is the bandwidth, θ_b is the resolution and θ_{FOV} is the FOV limit. It is therefore recommended to keep data in multi-channel format to utilise the large FOV possible with the e-MERLIN array.

The integration time taken for each visibility averages a portion of the spatial frequency coverage which results in orbicular aberration in the (u,v) plane (McDonald et al. 2002). Each visibility is assigned a central co-ordinate on the (u,v) plane during the correlation process which, upon averaging, is not necessarily valid at different points of the visibility. This again limits the FOV as can be seen in the following equation;

$$\tau \ll \frac{\theta_b/\theta_{FOV}}{\omega_{\oplus}}, \quad (2.9)$$

where τ is the integration time of the observations and ω_{\oplus} is equal to the angular rotation speed; 7.27×10^{-5} radians s^{-1} .

The observations in this thesis utilise the wide-field imaging capabilities of the e-MERLIN array. The galaxies used in this project have a median distance of 20 Mpc, hence wide-field images are advantageous to include compact sources that might have otherwise been missed in galaxies with large angular scales.

2.2 e-MERLIN

The e-MERLIN (e-Multi-Element Remote Linked Interferometer Network) array is a high-resolution radio interferometer which consists of seven radio telescopes spanning 217 km across the UK and is able to image objects with resolutions of much less than an arcsecond. e-MERLIN currently observes at L-band (1.2-1.7 GHz), C-band (4-8 GHz) and K-band (22-24 GHz). e-MERLIN is a common user facility with applications ranging from solar physics, planet formation, through to star-formation, galaxy evolution and cosmology. This includes areas such as (i) the history of star-formation and black hole growth as galaxies evolve, (ii) the physical processes that govern the formation of stars, (iii) the modes of activity in nearby galaxies, (iv) the energetic processes in relativistic outflows from jets generated by black holes and compact objects.

The high sensitivity and angular resolution provided by e-MERLIN make it one of the best radio facilities in the world. With C-band linear resolutions of less than 4 pc at a distance of 20 Mpc, HII regions and SNe will be resolved, as will AGN on sub-torus scales (Beswick and McHardy 2008). The field of view of the array is up to 27.5 arcmin at L-band, enabling wide-field imaging and the observation of the optical extent of most galaxies.

The resolution of e-MERLIN is vital to the improvement of our knowledge of galaxies and the processes within them, as it enables the identification of objects within galaxies to better understand the processes of both SF and accretion separately.

A full list of the technical capabilities of e-MERLIN is given in Table 2.1.

	1.5 GHz (L-Band)	5 GHz (C-Band)	22 GHz (K-Band)	Comments
Resolution (mas)	150	40	12	Uniform weighting at central frequency
Field of View (arcmin)	30	7	2.0	FWHM of 25-m dishes; reduced when Lovell Telescope included at 1.5 or 5 GHz
Frequency Range (GHz)	1.3-1.7	4-8	22-24	
Bandwidth (GHz)	0.4	2	2	Max. bandwidth per polarization. Can use 4 GHz, single plzn, at 5 or 22 GHz
Sensitivity (μ Jy/bm) in full imaging run	5-6	1.8-2.3	~ 15	Final performance will depend on usable bandwidth, final receiver optimization, Lovell Telescope performance. These figures are for e-MERLIN with the Lovell Telescope
Surface Brightness Sensitivity (K)	~ 190	~ 70	~ 530	As above
Astrometric Performance (mas)	~ 2	~ 1	~ 2	typical 3-deg target-calibrator separation using VLBA Calibrator Survey
	~ 0.5	~ 0.2	~ 1	Day-to-day repeatability using surveyed or in-beam sources, and assuming full imaging run
Amplitude Calibration	2%	1%	10%	Targets for day-to-day repeatability

Table 2.1: The technical capabilities of the e-MERLIN array in L, C and K-bands. Table taken from Beswick (2013).

2.3 Observations and Data Reduction

e-MERLIN L-band observations of the 4th LeMMINGs block were completed on the 28th December 2014, with a total observing time of ~ 11.5 hours. Within this time, a total of 6.7 hours was spent observing the ten target sources, with 40 minutes on each. 8 sub-bands were used, each with a bandwidth of 64 MHz containing 512 channels per sub-band and an average frequency of 1.51 GHz, and the integration time for the observations was 1 second. During implementation of the e-MERLIN pipeline, the data are averaged to 128 channels with 2 second integrations to reduce the data volume while avoiding smearing effects.

As well as the ten target sources that were observed as part of the LeMMINGs project, a total of seven calibrator sources were also observed to complete the data reduction process. They include the flux calibrator 3C 286 (or 1331+305) whose true flux is well documented, the point-source calibrator OQ 208 (or 1407+284) which is used to apply a bandpass calibration, and 5 phase calibrators. During the observations, the telescopes observed the phase calibrators at 8 minute intervals for 1 minute each. A list of these calibrators can be seen in Table 2.2.

3C 286 is heavily resolved by the e-MERLIN array which means that it cannot be assumed to be a point source. As a result, some of the flux is resolved out and is only detected by the shorter baselines. To overcome this issue, L and C-band models have been made available that have been scaled to the correct flux density.

Six of the possible 7 antennas were used for these observations, excluding the 76 m Lovell telescope. The other antennas are listed in Table 2.3 along with their identification numbers, dish diameter and location. The data are sent remotely to the Jodrell Bank Observatory where they are correlated, then assembled and pre-processed to average the data and remove the worst of the interference.

Object Name	Type
1331+305	Flux Calibrator
1407+284	Point Source Calibrator
0027+5958	Phase Calibrator
0038+4137	Phase Calibrator
0039+4900	Phase Calibrator
2343+2339	Phase Calibrator
0004+2019	Phase Calibrator

Table 2.2: List of calibrator sources and their purposes when calibrating the LEM04 data.

Telescope Name	Telescope Number	Diameter	Location
Mk 2	2	25 m	Jodrell Bank, Cheshire
Knockin	5	25 m	Shropshire
Defford	6	25 m	Worcestershire
Pickmere	7	25 m	Cheshire
Darnhall	8	25 m	Cheshire
Cambridge	9	32 m	Cambridgeshire

Table 2.3: List of telescopes that were included in observations and their respective numbers for identification.

2.3.1 e-MERLIN Data Reduction

Data reduction was carried out using the National Radio Astronomy Observatory (NRAO) Astrophysical Image Processing System (AIPS).

Flagging

The FITS data was first loaded into AIPS using the FITLD task. Once the data had been uploaded, a list of sources and their observing properties were retrieved using the LISTR command. UVFLG allows the user to flag any bad data in (u,v) co-ordinates, and SPFLG is used to flag data at specific time ranges or channels by reviewing the spectral data. All calibrator sources should be flagged to remove bad visibilities which may later hinder the quality of calibrations.

Calibrations

1. Confirming Stokes and Flux Density Values

The first calibration step was to run the PRTAB task which is used to view information about each individual source including the relevant flux densities and polarization measurements. Stokes values for I, Q, U and V polarizations are produced during the running of PRTAB, which must be confirmed. All I values must be either 1 or 0, and any unknown Q, U and V values should all be set to 0. If any of these values are incorrect, the task SETJY must be run to reset the flux density and stokes values for the observations. This task produces a new set of values for the flux density, which for the flux calibrator should increase with decreasing frequency as it has a negative spectral index. If the flux density values are still incorrect, SETJY can be run again but with some changes to the input parameters. In this case, the *OPTYPE* parameter (an adverb that specifies the operation type) should be set to ‘*CALC*’ which calculates new flux density values from a catalog.

2. Fringe Fitting and Delay Solutions

Once the flux calibrator values are correctly inputted, any delays from the calibrator sources must be removed. The task FRING implements fringe fitting which creates a modified data set in a SN (solution) table, in which any modifications are stored. The calibrator delays can be visualised using the task SNPLT which plots the solutions from the first round of fringe fitting. In this case, *OPTYPE* is set to ‘DELA’ to plot specifically the calibrator delays. Any obvious outliers were then removed using the task SNEDT which allows the user to edit the current SN table and remove any bad visibilities whilst creating a new, modified SN table.

CLCAL was the next task used, which interpolates the solutions in a SN table and writes them to a new table which contains calibration (CL) information. CLCAL was applied to each source to ensure that the corrected solutions were transferred to the appropriate CL table.

3. Phase Calibration and Initial Bandpass

The next step of the procedure was to calibrate the phases of each source and run an initial bandpass. To complete the phase calibrations, a model image of the flux calibrator 3C 286 was uploaded using FITLD as before. The task CALIB automatically calibrates the observations to the model of 3C 286 and determines how many good solutions there are. If enough good solutions are available (which implies the observations match the model well), the same calibration can be run on all other calibrator sources.

If a large number of solutions fail, the visibilities should be re-assessed to check for areas of bad data that could be affecting the calibration. If this is not the case, the CALIB parameters can be altered to force the software to accept

points of lower quality, by decreasing the signal to noise ratio limit or reducing the number of antennas required for a good solution, for example.

Otherwise, the phases can then be visualised using SNPLT again to plot phase against time with *OPTYPE* set to ‘*PHAS*’ (which displays phase as opposed to delays when using ‘*DELA*’). By running the CLCAL task again, the solutions from the phase calibration will be copied from the SN table (with the corrected phase solutions) to a new CL table. The initial bandpass can then be run using the task BPASS which creates a bandpass (BP) table with all of the corrected and calibrated data.

4. Amplitude and Phase Calibration

The next round of calibrations corrects both the phases and amplitudes of the data. The process is much the same as before, but the fact that amplitude is also being calibrated must be stated in the CALIB menu. The parameter *SOLMODE* modifies the solution mode during a calibration, which must be changed from the default to ‘*AMP*’ (Amplitude & Phase).

5. Derive Flux Densities and Final Bandpass

At this point the fluxes were derived for OQ 208 and the phase calibrators using the task GETJY which determines flux density values for each source based on the calibrated data. The task SOUSP takes these values and plots them as spectra with amplitude against frequency so that a spectral index can be calculated. A second bandpass is also run to smooth the amplitude and phases and a final round of calibration applies the solutions to all calibrator sources and targets.

Figure 2.4 shows an example spectral plot of OQ 208 after flagging, fringe-fitting and bandpass calibrations. A summary of the AIPS data reduction and

calibration procedure used for the data in this thesis can be seen in the flowchart in Figure 2.5.

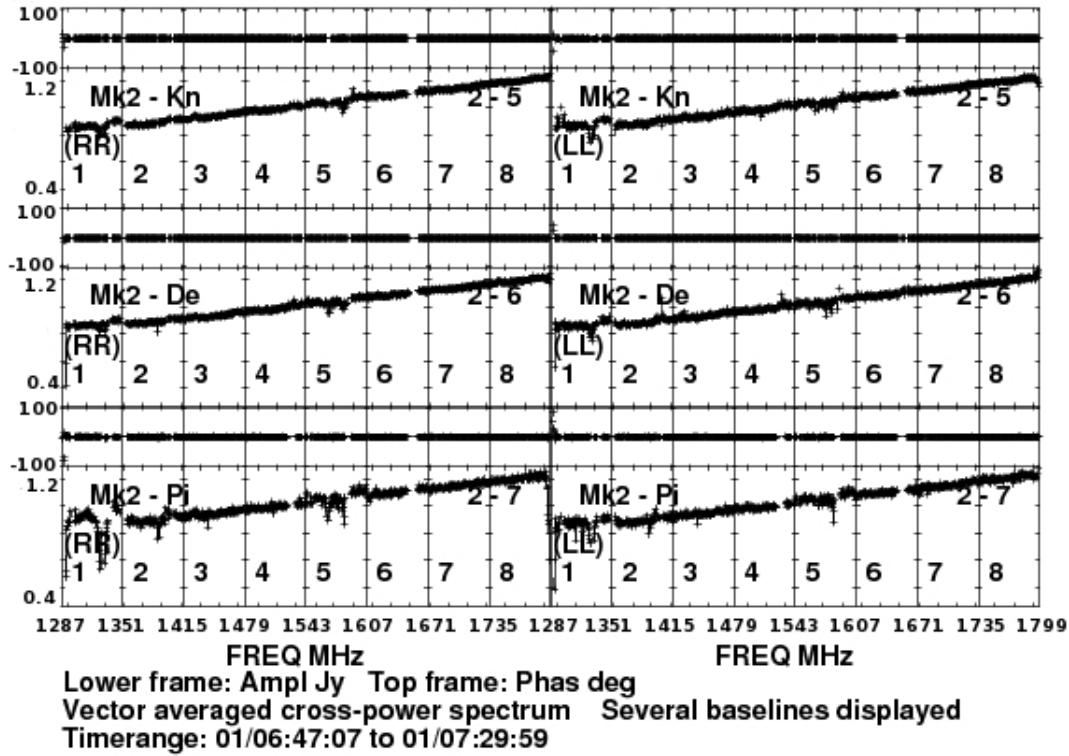


Figure 2.4: Example spectral plot of flagged, fringe-fitted and bandpass-calibrated data for the point source calibrator OQ 208, using the POSSM task in AIPS. Note that there is some radio frequency interference (RFI) in the lowest two spectral windows.

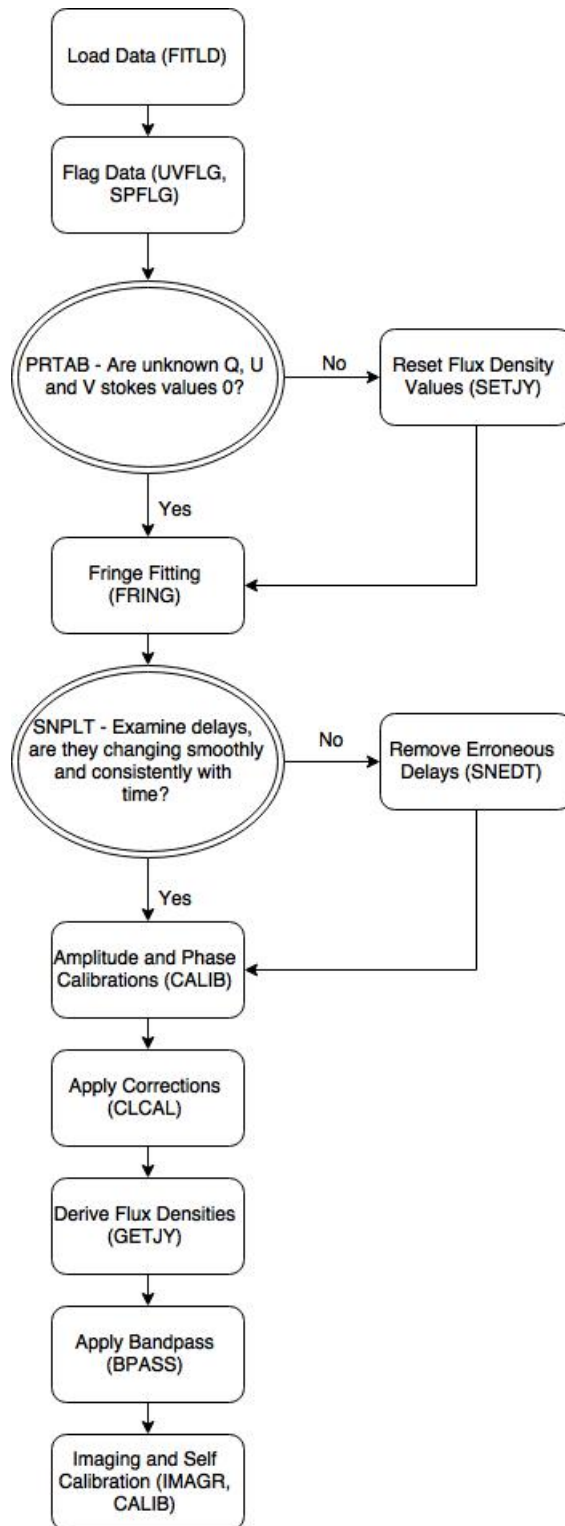


Figure 2.5: Flowchart of the data reduction and calibration procedure used in AIPS.

2.3.2 Imaging and Self-Calibration

Before imaging the target sources, the phase calibrators were calibrated after the most recent bandpass. To self-calibrate, an image was first produced of the phase calibrators using the IMAGR task. The cellsize was set to $0''.045$ to ensure that the beam was Nyquist sampled, and the image size (*IMSIZE*) was set to 512×512 pixels. A natural weighting function was used due to the point-like nature of the sources, and the number of CLEAN iterations (*NITER*) was set to 300. A CLEAN box can be drawn around the source and CLEANing can commence.

The data were then self-calibrated by using the CLEANed image as a model in much the same way as the flux calibrator, by running CALIB and CLCAL to interpolate the solutions.

The target data were then plotted in amplitude against uv-distance using the UVPLT task and any outliers were removed via CLIP, specifying a maximum amplitude value.

The targets were then imaged using IMAGR. Because of the wide field that is utilised in e-MERLIN observations, the preliminary image size and cell size were set to large values of 8192×8192 pixels and $0''.2$ respectively to find any bright sources in the field.

Co-ordinates of specific points in the field where there was suspected flux were written in a ‘boxfile’ to image multiple fields in a single pass of IMAGR. These fields were then imaged to a greater degree of accuracy, with the *CELLSIZE* changed to $0''.045$ and the *IMSIZE* changed to 512×512 pixels to create smaller images of each source and speed up the CLEANing process.

Initially, sources were imaged using a robustness of 0, to implement high resolution imaging without compromising the signal-to-noise ratio too much. For some sources, the robustness and weighting functions were altered depending on whether they exhibited extended or compact emission.

The number of CLEAN iterations was set initially to 1000, again this was

altered depending on the morphology and brightness of the sources. For many sources the first intermediate frequency (IF) was excluded, as IF 1 exhibited lots of interference that wasn't eradicated during the various rounds of flagging (this effect can also be seen for OQ 208 in Figure 2.4).

The target sources with a signal-to-noise ratio of greater than 5 were also self-calibrated to reduce the noise in the images, although most of the targets and confusing sources in this thesis had lower signal-to-noise ratios and so were not self-calibrated.

Confusing Sources

A number of the observations had bright, confusing sources within the field that create a stirping effect in the images due to the sidelobes from the object. The problem occurs when the confusing source is present in the antenna primary beam, and the resulting contamination decreases the quality of any subsequent images where the confusing source has not been deconvolved. The method used to reduce these effects for this thesis was to deconvolve the source using CLEAN and remove the CLEAN components from the data using the UVSUB task.

2.4 Summary

This chapter has explained the basics of radio interferometry that have been utilised in the e-MERLIN observations for this thesis. As well as the basic mechanisms behind how interferometers work and the specifications for e-MERLIN and the LeMMINGS project, the calibration methods have also been explained from the point where the pipeline has been run to final imaging. The results from the observations can be seen in Chapter 3.

Chapter 3

Results

The galaxy sample for this thesis includes the 4th block of LeMMINGS targets which consists of ten optically selected galaxies with a median distance of 20 Mpc. A review of the LeMMINGS project can be seen in section 1.5. Of the ten galaxies that were included in the sample, just one exhibited a high enough flux density to be detected in the e-MERLIN observations (IC10). This section looks at the results of these observations, including the nine galaxies that were not detected and the field sources in the observations. All values and images quoted as being from the NVSS are taken from 1.4 GHz NRAO VLA Sky Survey (Condon et al. 1998), and if not otherwise stated, all spectral index values have been taken from NED (2015). *Spitzer* 24 μm infrared images have been included for background purposes, and unless otherwise stated are taken from the *Spitzer* Heritage Archive (SHA). These infrared observations were undertaken by the *Spitzer Space Telescope*, which is operated by the Jet Propulsion Laboratory, California Institute of Technology under contract with NASA.

The list of target sources can be seen in Table 3.1 with their observational properties taken from previous studies.

Observation Identifier	Alternative Name	Morphology	1.4 GHz Total Flux Density** (mJy)	Distance to Centre (Mpc)	Apparent Major Axis* (")	Apparent Minor Axis* (")	Linear Major Axis* (kpc)	Linear Minor Axis* (kpc)
0003+2045	NGC 7817	Sb/c (edge on)	33.6 ± 2.1	25.95	165.00	43.00	20.81	5.41
0020+5917	IC10	dIrr	129.3 ± 4.5	0.89	701.00	427.61	3.03	1.85
0033+4830	NGC 147	dE5 pec	-	0.78	651.80	319.38	2.43	1.19
0038+4820	NGC 185	dE3 pec	-	0.74	651.80	567.07	2.34	2.04
0040+4141	NGC 205	dE5 pec	-	0.81	1151.00	713.62	4.53	2.81
0042+4051	NGC 221	compact dE2	-	0.78	458.40	398.81	1.71	1.50
0042+4116	M31	SA(s)b	81.0 ± 4.6	0.79	6200.00	3472.00	23.57	13.20
0052+4733	NGC 278	SAB(rs)b	142.2 ± 5.0	11.80	149.3	146.31	8.54	8.37
2343+2604	NGC 7741	SB(s)cd	15.0 ± 2.4	14.28	169.60	74.62	11.74	5.17
2359+2045	NGC 7798	SBc	37.5 ± 1.8	32.60	107.50	77.40	16.99	12.23

Table 3.1: List of sources within the LEM04 sample with their alternate names, morphologies, radio flux at 1.4 GHz and apparent and linear sizes assuming the distance to the source.

* Data taken from the 2MASS Large Galaxy Atlas (Jarrett et al. 2003).

** Data taken from the NRAO VLA Sky Survey (Condon et al. 1998).

3.1 NGC 7817 (0003+2045)

NGC 7817 is an edge-on spiral (Sb/c) galaxy at a distance of 26 Mpc. Observations show strong H α emission throughout the galaxy, as well as bright HII regions associated with the disk (Miller and Veilleux 2003). These HII regions emit light at radio frequencies, and the corresponding 1.4 GHz NVSS values for the flux density are 33.6 mJy.

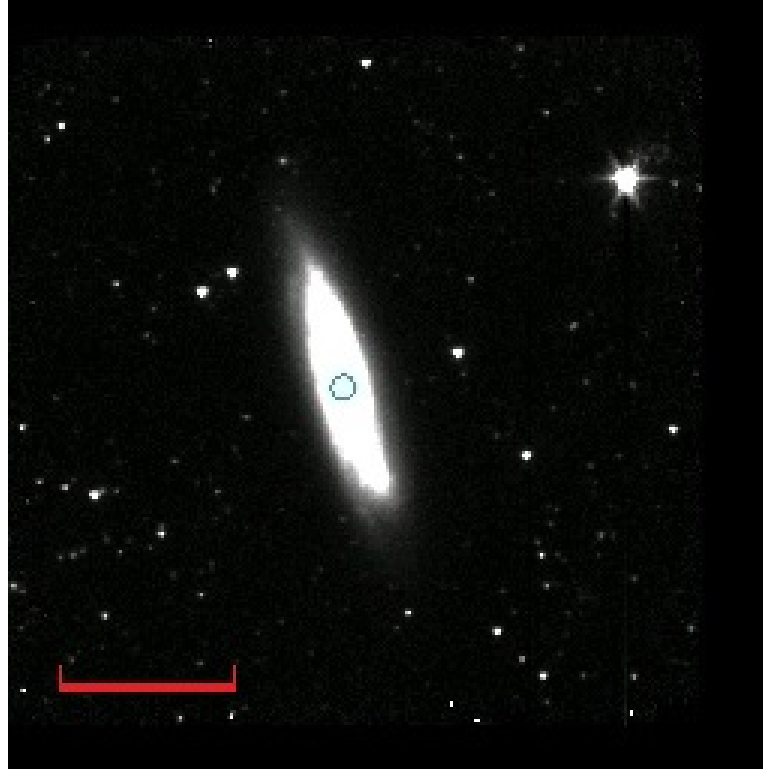


Figure 3.1: A *Spitzer* 3.6 μm image of NGC 7817. The red scale bar indicates an angular distance of 0.02.

Figure 3.1 shows a 3.6 μm image of NGC 7817 taken by *Spitzer* in 2009. This was the only one of the ten target galaxies with no 24 μm data available, hence the smaller wavelength image has been used. The bright regions of the disk indicate regions of star formation, whereby re-radiation of dust from massive O and B-type stars causes thermal emission in the galaxy.

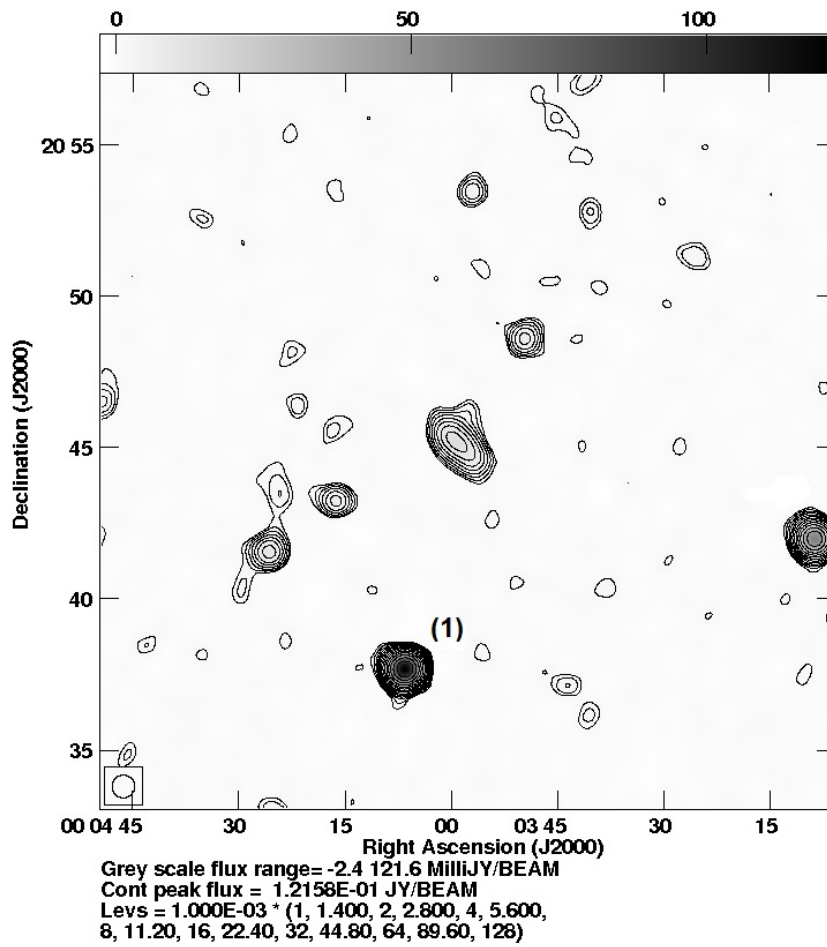


Figure 3.2: NVSS field of NGC 7817. The contours are 1, 1.4, 2, 2.8, 4, 5.6, 8, 11.2, 16, 22.4, 32, 44.8, 64, 89.6, 128 mJy/beam. The circle at the bottom left corner represents the beams size which is $45'' \times 45''$.

Figure 3.2 shows the 1.4 GHz NVSS field of NGC 7817 with an equivalent field of view of the e-MERLIN array ($\sim 23'$). As well as the target, a field source is clearly visible as a bright point which has been labelled (1). Both the target galaxy and the field source were imaged, and a contour map of the field source can be seen in Figure 3.3.

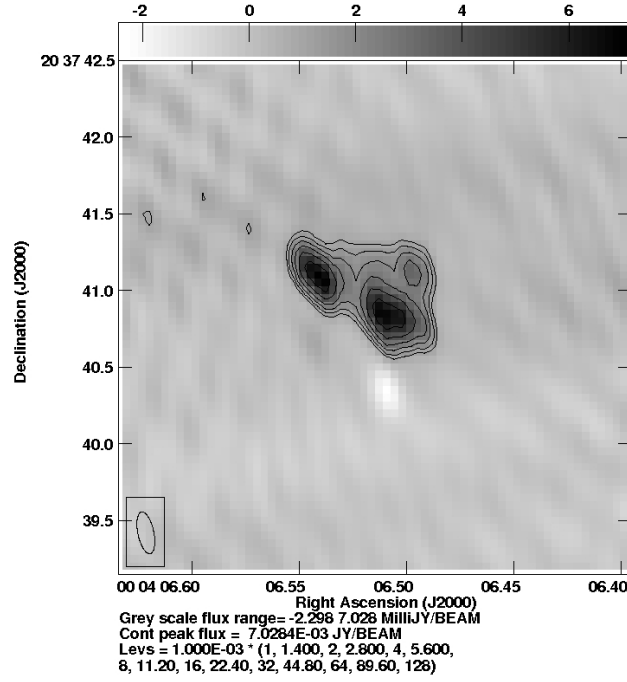


Figure 3.3: A source in the field of NGC 7817, labelled (1) in Figure 3.1. The contours 1, 1.4, 2, 2.8, 4, 5.6, 8, 11.2, 16, 22.4, 32, 44.8, 64, 89.6, 128 mJy/beam. The ellipse in the bottom left corner represents the beam size which is $0''.22 \times 0''.46$

This field source is described as being a ‘symmetrical double’ radio source with a spectral index of -0.7 (Becker et al. 1991; Douglas et al. 1996). The total flux density value from the NVSS observations is around 127.1 mJy, and the observed values from the e-MERLIN observations can be seen in Table 3.2.

RA (HH:MM:SS.s)	00 04 06.52 \pm 3.44 s
DEC (DD:MM:SS.s)	20 37 40.9 \pm 32".18
Angular Distance from Pointing Centre (')	7.68
Peak Flux IMAGR (mJy/beam)	7.028
Total Flux NVSS (mJy)	127.1 \pm 8.8
RMS Noise (mJy/beam)	0.1640
Resolved?	Yes
Gaussian 1:	
Peak Flux JMFIT (mJy/beam)	5.94 \pm 0.10
Total Flux JMFIT (mJy)	35.81 \pm 0.66
Gaussian 2:	
Peak Flux JMFIT (mJy/beam)	7.06 \pm 0.09
Total Flux JMFIT (mJy)	16.87 \pm 0.32

Table 3.2: Observed values for the source in the field of NGC 7817.

The peak flux density from IMAGR was taken from the value observed by the KNTR task, which was used to create Figure 3.3 by fitting contours to the source image. The second peak flux density measurement was observed using the JMFIT task, which fits a Gaussian distribution to the source and calculates peak flux, total flux and gives precise information about the location and size of the object. As the field source exhibits a double radio structure, two Gaussian components were fitted to calculate values for both peaks. The purpose of using the JMFIT measurements was to test the validity of fluxes observed by IMAGR which does not give error values, and to confirm that the JMFIT values are accurate so that the total flux density measurements can be considered credible. As the IMAGR measurements are within 1σ of the JMFIT values, it is possible to deduce that these are accurate and the JMFIT total flux density values are

valid. The NVSS total flux measurement of the field source, however, is much higher than the measured value from these observations. As the object is resolved in the observations, it is likely that the emission is being resolved out due to the high resolution of the e-MERLIN observations.

NGC 7817 itself was undetected in the observations. The NVSS values for the total flux density are 33.6 mJy, whereas the values for the field source are 126.6 mJy. As the field source is almost four magnitudes brighter than the target galaxy itself, the clean components from the field source were removed during the imaging stage to see whether this emission was obscuring the observations of NGC 7817. After removing the flux from the field source, it was still not possible to detect NGC 7817, hence no images were produced.

3.2 IC10 (0020+5917)

IC 10 is a dwarf irregular galaxy (dIrr) at a distance of 0.89 Mpc. It exhibits a high star formation rate (SFR) due the irregular nature of the galaxy which is a result of a recent interaction or merger (Nidever et al. 2014). The SFR of IC10 from $H\alpha$ measurements is $0.04\text{--}0.08\text{ M}_{\odot}\text{ yr}^{-1}$ (Thronson et al. 1990; Magrini and Gonçalves 2009). HII regions are prominent within the galaxy as are RSNe, which are observed as the high-mass stars created in these regions end their lives. These result in the radio emission that we observe from the galaxy, and the NVSS total flux density value for the galaxy at 1.4 GHz is 129.3 mJy. Figure 3.4 shows a high resolution EVLA image of the galaxy. The compact sources within IC 10 are clearly visible within the EVLA image, and these radio sources make it an excellent galaxy from which to study star formation.

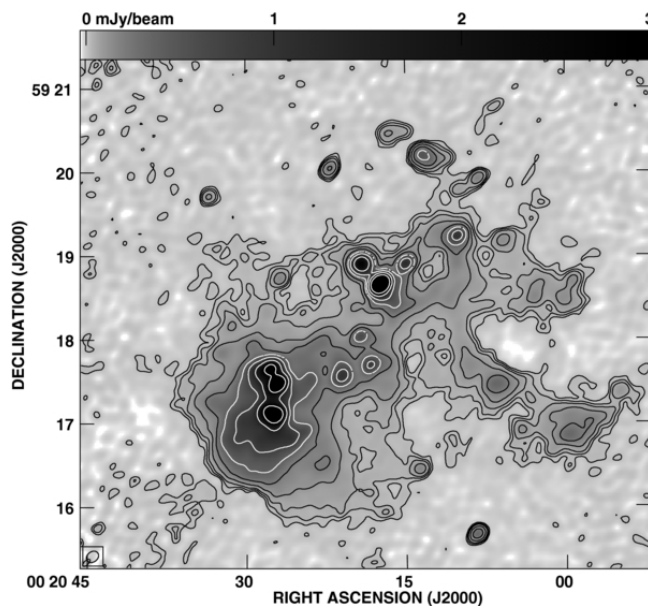


Figure 3.4: An EVLA observation of the dwarf irregular galaxy IC 10 at 5 GHz. The resolution of the image is $9''.4 \times 7''.3$ and the contours are 3, 6, 10, 20, 40, 80, 150, 300 and $600 \times 5\text{ }\mu\text{Jy/beam}$. Image taken from Heesen et al. (2011).

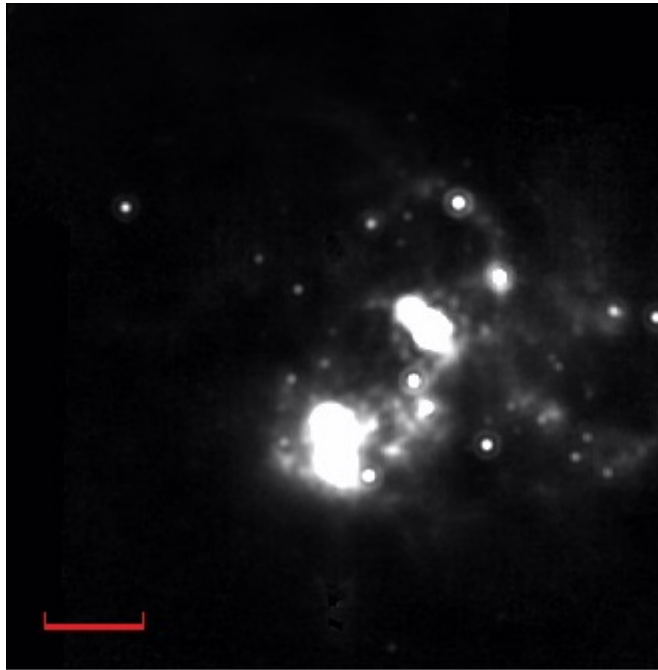


Figure 3.5: 24 μm *Spitzer* MIPS image of IC10, courtesy of Bendo et al. (2012). The red scale bar indicates an angular distance of 0 "02.

Figure 3.5 shows a 24 μm *Spitzer* MIPS (Multiband Imaging Photometer for *Spitzer*) image of IC10 processed by G. J. Bendo via the same methods as in Bendo et al. (2012). The bright areas of the galaxy indicate regions of star formation, whereby thermal re-radiation of dust from massive O and B-type stars causes emission at infrared wavelengths. These bright regions also correspond to the areas of high flux density at radio frequencies, as can be seen in the VLA image in Figure 3.4.

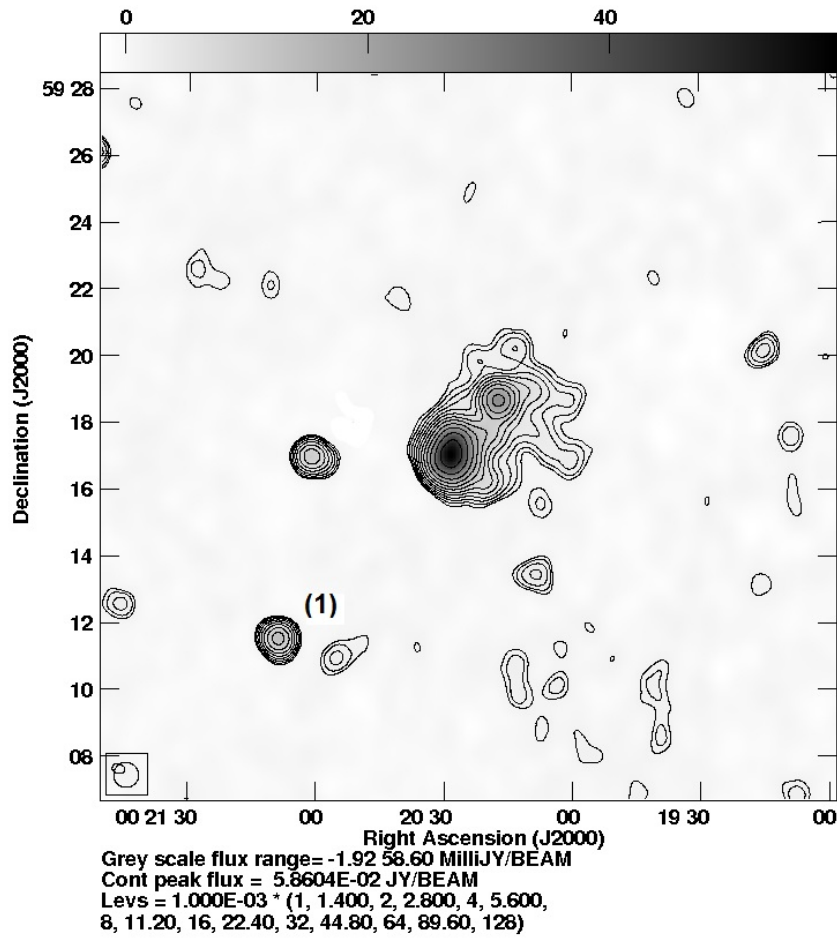


Figure 3.6: NVSS field of IC10. The contours are 1, 1.4, 2, 2.8, 4, 5.6, 8, 11.2, 16, 22.4, 32, 44.8, 64, 89.6, 128 mJy/beam. The circle at the bottom left corner represents the beams size which is $45'' \times 45''$.

Figure 3.6 shows a 1.4 GHz NVSS image of IC10 with an equivalent field of view of e-MERLIN and hence includes any field sources that have been detected in the observations, such as the bright source labelled (1).

Of the many compact objects in IC10 itself, just one has been detected in these observations which can be seen in Figure 3.7, and observed values for this object can be seen in Table 3.3.

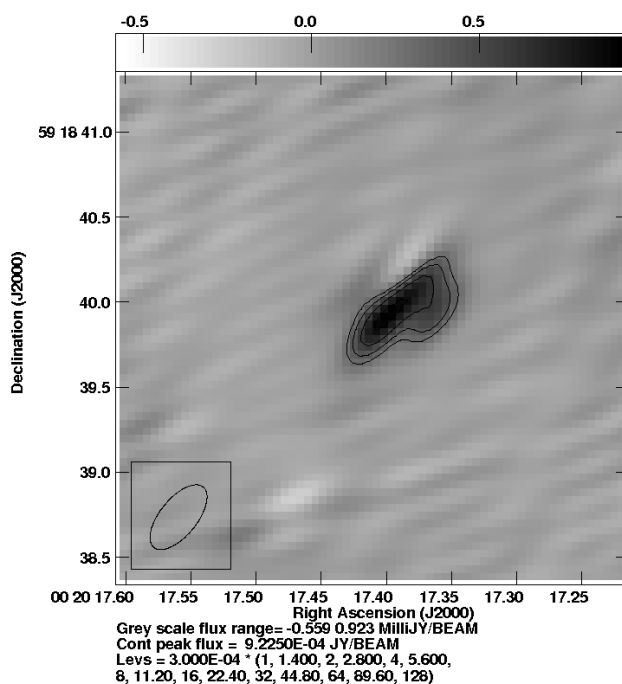


Figure 3.7: A compact object in IC10. The contours are $0.3 \times 1, 1.4, 2, 2.8, 4, 5.6, 8, 11.2, 16, 22.4, 32, 44.8, 64, 89.6, 128$ mJy/beam. The ellipse in the bottom left corner represents the beam size which is $0''.46 \times 0''.22$.

RA (HH:MM:SS)	00 20 17.389 \pm 12.98 s
DEC (DD:MM:SS)	59 18 39.94 \pm 78''01
Angular Distance from Pointing Centre (')	1.404
Peak Flux IMAGR (mJy/beam)	0.923
Peak Flux JMFIT (mJy/beam)	0.87 \pm 0.10
Total Flux NVSS (mJy)	20.8 \pm 0.8
Total Flux JMFIT (mJy)	1.610 \pm 0.272
RMS Noise (mJy/beam)	0.1080
Resolved?	Yes

Table 3.3: Observed values for the compact object in IC10.

The NVSS total flux density value for this compact object is 20.8 mJy. As

before, the total flux density for the e-MERLIN observations was observed by fitting a Gaussian distribution to the object using JMFIT. The peak flux density values from IMAGR are within 1σ of those observed by JMFIT, so both values are deemed to be accurate for these observations.

The NVSS value for the total flux density of this compact source is much higher than the measured value of 1.61 mJy. This indicates that not all of the flux from the compact object is being detected in the e-MERLIN observations. It is probable that this is due to the high resolution of the e-MERLIN observations which means the object is resolved, which results in the resolving out of some of the emission.

As well as the compact object, a field source in the field labelled (1) in Figure 3.6 has also been imaged and can be seen in Figure 3.8.

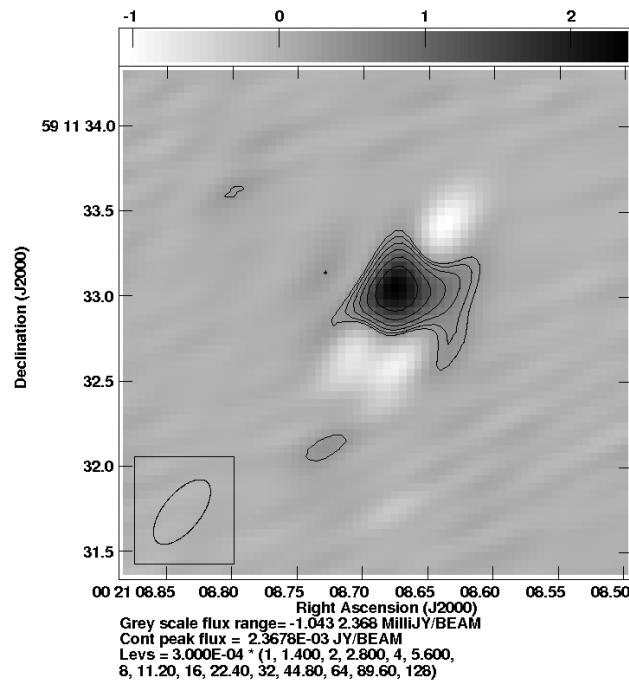


Figure 3.8: A source in the field of IC10, labelled (1) in Figure 3.4. The contours are $0.3 \times 1, 1.4, 2, 2.8, 4, 5.6, 8, 11.2, 16, 22.4, 32, 44.8, 64, 89.6, 128$ mJy/beam. The ellipse in the bottom left corner represents the beam size which is $0''.46 \times 0''.22$.

There are some large negatives in Figure 3.8 which indicate a problem with

the short spacings of the interferometer itself. In an array, it is not possible to have a zero baseline as this would require observations from a single antenna. The minimum (u,v) distance of the e-MERLIN array is $30 \text{ k}\lambda$ which is the most probable cause of the negative areas around the field source. The NVSS total flux density value for the field source is 13.6 mJy , and the observed values for this object can be seen in Table 3.4.

RA (HH:MM:SS)	$00 \ 21 \ 08.676 \pm 4.55 \text{ s}$
DEC (DD:MM:SS)	$59 \ 11 \ 33.29 \pm 29''.92$
Angular Distance from Pointing Centre (')	8.28
Peak Flux IMAGR (mJy/beam)	2.368
Peak Flux JMFIT (mJy/beam)	2.11 ± 0.11
Total Flux NVSS (mJy)	13.6 ± 0.6
Total Flux JMFIT (mJy)	3.4400 ± 0.2620
RMS Noise (mJy/beam)	0.1111
Resolved?	Yes

Table 3.4: Observed values for the field source in IC10.

The peak flux density value observed by IMAGR is within 3σ of the value observed by JMFIT, so both values are deemed to be accurate for these observations. The NVSS total flux value, however, is much higher than the JMFIT observed value of 3.44 mJy which again indicates that the e-MERLIN observations are not detecting a large proportion of the flux from these objects. Again this could be due to some of the emission from the source being resolved out in the observations due to the high resolution.

3.3 NGC 147 (0033+4830)

NGC 147 is a peculiar dwarf elliptical (dE5 pec) satellite galaxy of M31 that resides at a distance of 0.77 Mpc (Geha et al. 2010). The galaxy exhibits very little star formation, and early observations by Mould et al. (1983) showed no evidence of stars younger than 1 Gyr (Davidge 2005). The galaxy is considered to have no dust clouds or centrally concentrated blue stars (Han et al. 1997), although Davidge (1994) and Han et al. (1997) found a collection of moderately bright carbon-rich asymptotic giant branch stars distributed throughout the main body of the galaxy, indicating that there is an intermediate-age population of stars. A 21 cm study undertaken by Young and Lo (1997) detected no HI emission from the galaxy, which makes it an unlikely candidate to exhibit emission in L-band observations.

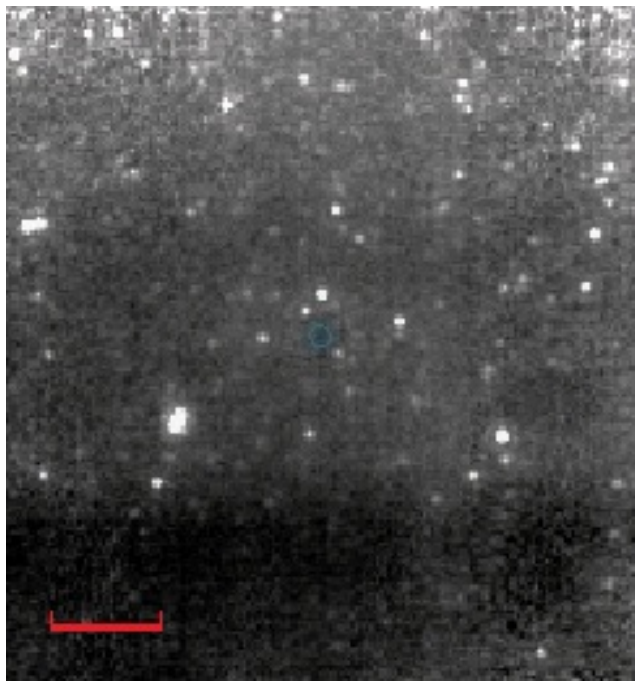


Figure 3.9: 24 μm *Spitzer* MIPS image of NGC 147. The red scale bar indicates an angular distance of 0''.02.

Figure 3.9 shows a 24 μm MIPS image of NGC 147 taken by *Spitzer* in 2006.

There appears to be no bright areas associated with the galaxy, which is in agreement with the lack of recent star formation of less than 1 Gyr. There are no bright O or B type stars which would have caused infrared emission via thermal re-radiation of dust so that galaxy itself is undetected in the *Spitzer* observations.

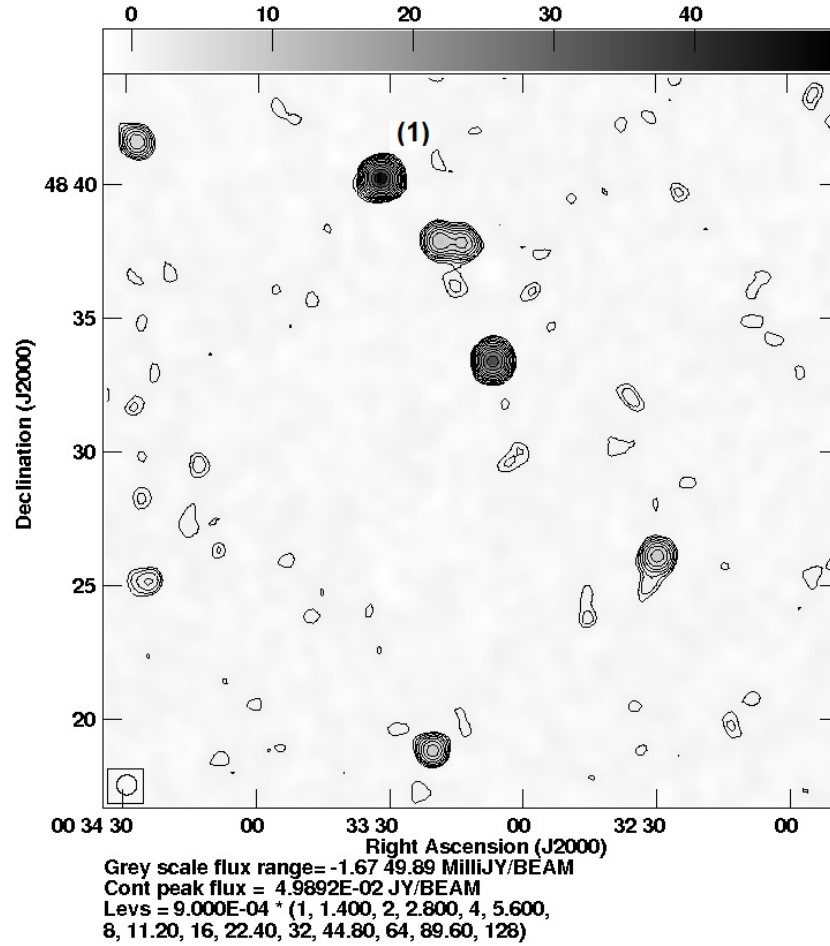


Figure 3.10: NVSS field of NGC 147. The contours are $0.9 \times 1, 1.4, 2, 2.8, 4, 5.6, 8, 11.2, 16, 22.4, 32, 44.8, 64, 89.6, 128$ mJy/beam. The circle at the bottom left corner represents the beams size which is $45'' \times 45''$.

Figure 3.10 shows the 1.4 GHz NVSS field of NGC 147. Although there is little evidence of emission from the galaxy at 1.4 GHz, there are field sources that have been detected. One of these has been labelled (1) in Figure 3.10 and the e-MERLIN image can be seen in Figure 3.11.

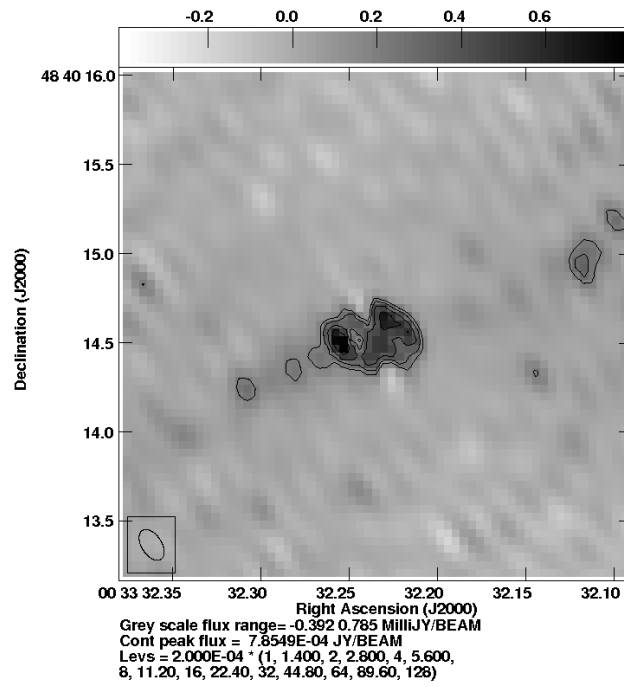


Figure 3.11: A source in the field of NGC 147, labelled (1) in Figure 3.7. The contours are $0.2 \times 1, 1.4, 2, 2.8, 4, 5.6, 8, 11.2, 16, 22.4, 32, 44.8, 64, 89.6, 128$ mJy/beam and the ellipse represents the beam size which is $0''.19 \times 0''.11$.

The total flux density value of the source from the NVSS is 53.9 mJy, and the spectral index is -0.8. The observed values from the e-MERLIN observations can be seen in Table 3.5.

RA (HH:MM:SS)	00 33 32.240 \pm 9.83 s
DEC (DD:MM:SS)	48 40 14.51 \pm 50".15
Angular Distance from Pointing Centre (')	10.44
Peak Flux IMAGR (mJy/beam)	0.7856
Peak Flux JMFIT (mJy/beam)	0.55 \pm 5.86 $\times 10^{-2}$
Total Flux NVSS (mJy)	53.9 \pm 1.7
Total Flux JMFIT (mJy)	0.4384 \pm 0.5220
RMS Noise (mJy/beam)	0.0811
Resolved?	Yes

Table 3.5: Observed values for the field source in NGC 147.

The peak value from the IMAGR task are within 3σ of those observed from JMFIT and so both values are deemed to be accurate from the observations. There is a large discrepancy between the NVSS and JMFIT total flux density values, however, which indicates that much of the flux from the source is not being detected in the observations. Again this could be due to some of the emission from the source being resolved out in the observations due to the high resolution.

NGC 147 itself was undetected in the observations. The NVSS does not give a value for the total flux density of the galaxy at 1.4 GHz, indicating that there is no emission from the galaxy at this frequency. This is also confirmed by the lack of 21 cm emission in the study by Young and Lo (1997).

3.4 NGC 185 (0038+4820)

NGC 185 is a peculiar dwarf elliptical (dE3 pec) satellite galaxy of M31 with a mean star formation rate of $6.6 \times 10^{-4} M_{\odot} \text{ yr}^{-1}$ (Martínez-Delgado et al. 1999). The youngest stars are ~ 400 Myr and are concentrated within the central 150 pc of the galaxy, which equates to an apparent diameter of $41''$ at a distance of 0.74 Mpc. A study by Kang et al. (2005) found a total of 73 carbon-rich asymptotic giant branch stars from mid-infrared observations within these central regions indicating an intermediate-age stellar population. This number is similar to the number of C stars in NGC 147, although they are more centrally located in NGC 185 (Davidge 2005).

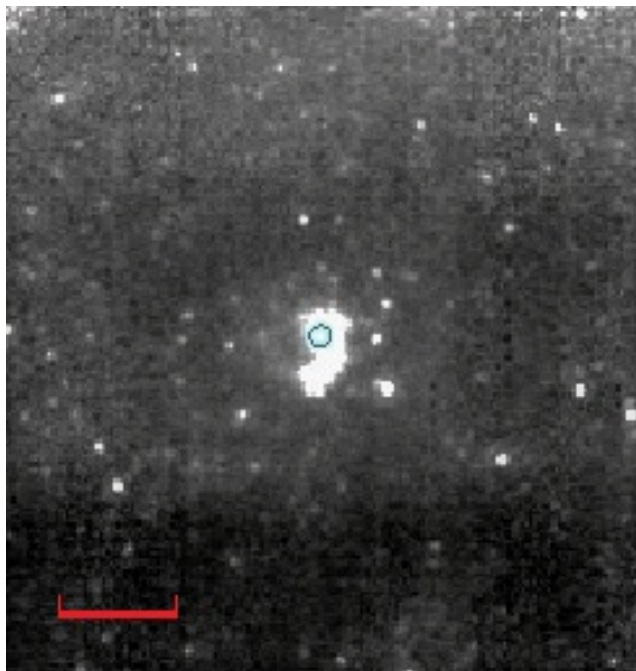


Figure 3.12: A $24 \mu\text{m}$ *Spitzer* MIPS image of NGC 185. The red scale bar indicates an angular distance of $0''.02$.

Figure 3.12 shows a $24 \mu\text{m}$ MIPS image taken by *Spitzer* in 2006. The bright area towards the central region of the galaxy corresponds to the intermediate age stars concentrated in the centre. This indicates that there are younger stars

that are emitting light at infrared wavelengths via thermal re-radiation of dust. This bright region is not seen at 1.4 GHz as can be seen in Figure 3.13.

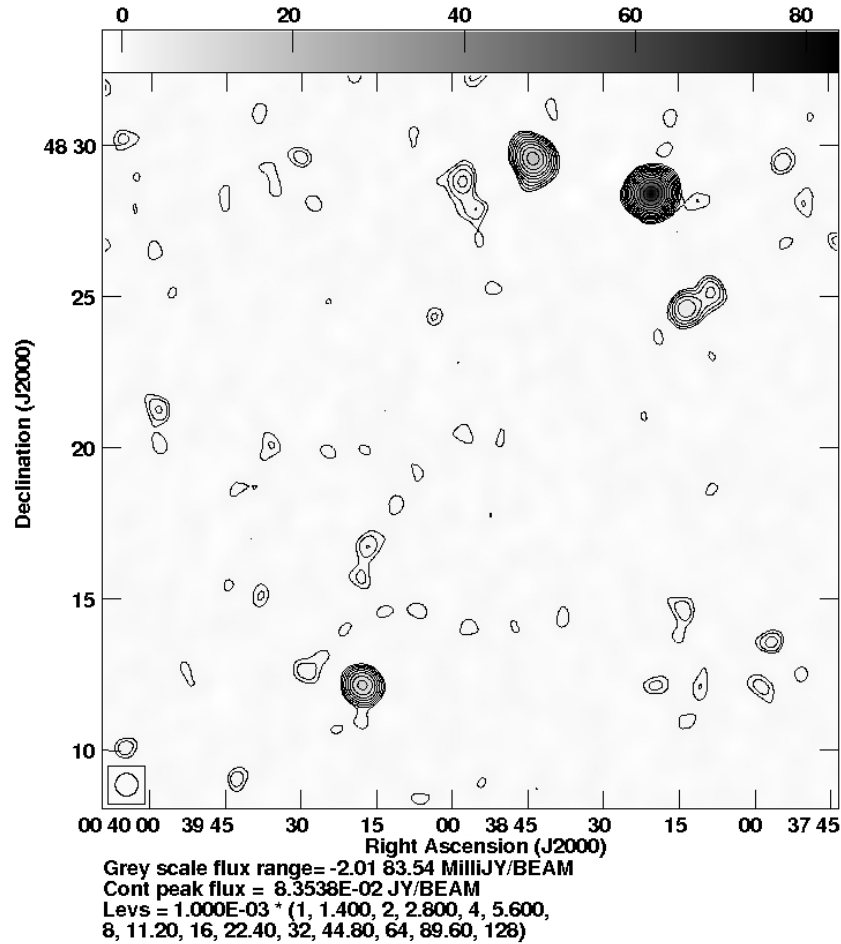


Figure 3.13: NVSS field of NGC 185. The contours are $0.9 \times 1, 1.4, 2, 2.8, 4, 5.6, 8, 11.2, 16, 22.4, 32, 44.8, 64, 89.6, 128$ mJy/beam. The circle at the bottom left corner represents the beam size which is $45'' \times 45''$.

Figure 3.13 shows the 1.4 GHz NVSS field of NGC 185 with a field of view equivalent to that of the e-MERLIN array. There appears to be little flux associated with the galaxy at 1.4 GHz unlike in the infrared image.

NGC 185 was undetected in the e-MERLIN observations, as were the field sources. The NVSS does not provide a total flux density for NGC 185 indicating that there were no detections in their observations. A 20 cm VLA study (Lucero

CHAPTER 3. RESULTS

and Young 2007) detected 0.3 mJy from NGC 185 which may explain why the galaxy has not been detected in the e-MERLIN observations due to the low flux density.

3.5 NGC 205 (0040+4141)

NGC 205 is another satellite galaxy of M31 at a distance of 0.81 Mpc, and is also a peculiar dwarf elliptical (dE5 pec). Like NGC 185, the carbon-rich stars are more centrally concentrated than those in NGC 147 and a younger population of stars is present with ages ~ 50 -100 Myr in the central regions. NGC 205 is over 3 times closer to M31 than NGC 147, and over 4 times closer than NGC 185. The close proximity to M31 has resulted in interactions which could have resulted in the most recent star formation episode that is not apparent in NGC 147 or NGC 185 (Davidge 2005).

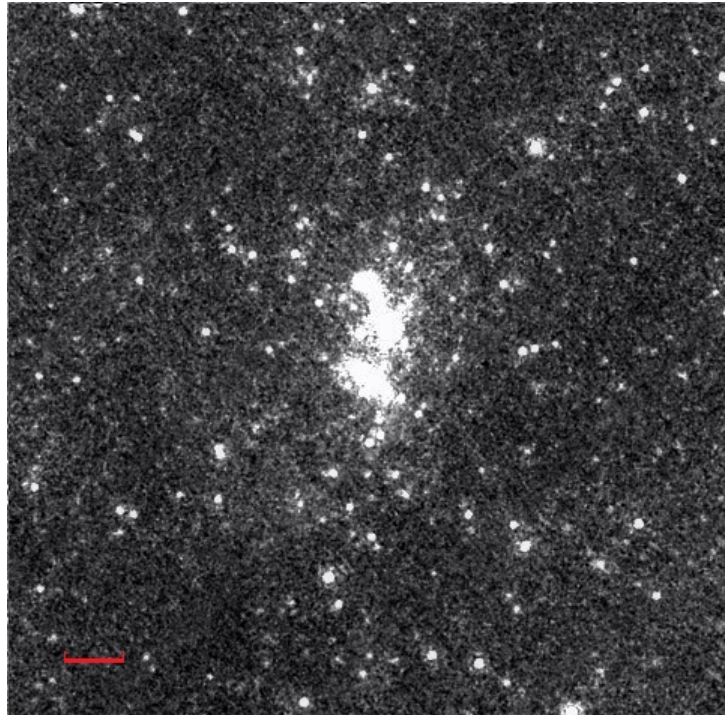


Figure 3.14: A $24\ \mu\text{m}$ MIPS image of NGC 205. This image is courtesy of Bendo et al. (2012). The red scale bar indicates an angular distance of $0''.02$.

Figure 3.14 shows a $24\ \mu\text{m}$ MIPS image taken by *Spitzer* in 2012 which was processed by G.J. Bendo via the same methods as in Bendo et al. (2012).

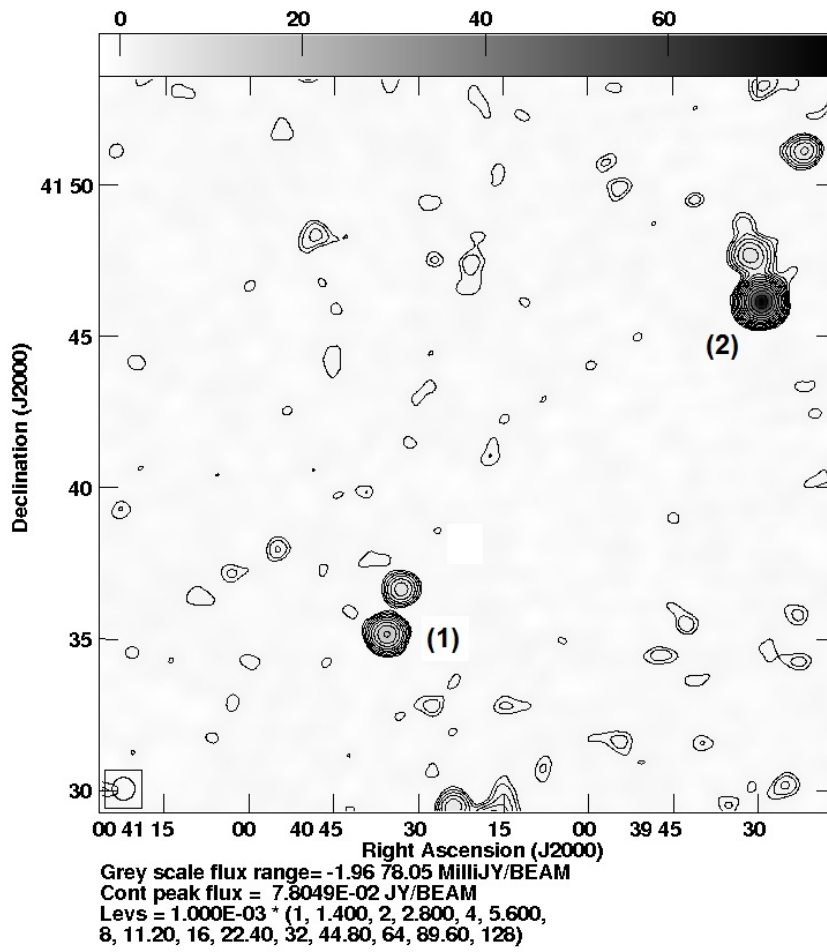


Figure 3.15: NVSS field of NGC 205. The contours are $0.9 \times 1, 1.4, 2, 2.8, 4, 5.6, 8, 11.2, 16, 22.4, 32, 44.8, 64, 89.6, 128$ mJy/beam. The circle at the bottom left corner represents the beams size which is $45'' \times 45''$.

Figure 3.15 shows the 1.4 GHz NVSS field for NGC 205 with an equivalent field of view to that of the e-MERLIN array. Again there is little flux associated with the galaxy at this frequency, although two of the field sources labelled (1) and (2) have been imaged and can be seen in Figures 3.16 and 3.17 respectively.

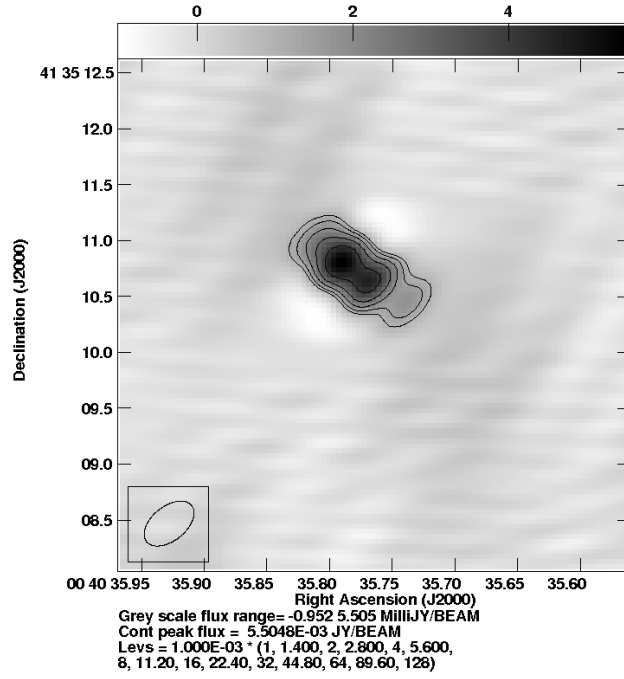


Figure 3.16: A source in the field of NGC 205, labelled (1) in Figure 3.115. The contours are 1, 1.4, 2, 2.8, 4, 5.6, 8, 11.2, 16, 22.4, 32, 44.8, 64, 89.6, 128 mJy/beam. The ellipse in the bottom left corner represents the beam size which is $0''.52 \times 0''.31$.

Figure 3.16 shows a source within the field of NGC 205. The flux density value from the NVSS is 17.9 mJy and the observed values from the e-MERLIN observations can be seen in Table 3.6.

RA (HH:MM:SS)	00 40 35.782 \pm 4.36 s
DEC (DD:MM:SS)	41 35 10.75 \pm 37''55
Angular Distance from Pointing Centre (')	6.71
Peak Flux IMAGR (mJy/beam)	5.505
Peak Flux JMFIT (mJy/beam)	5.20 \pm 0.21
Total Flux NVSS (mJy)	17.9 \pm 0.7
Total Flux JMFIT (mJy)	11.930 \pm 0.672
RMS Noise (mJy/beam)	0.1428
Resolved?	Yes

Table 3.6: Observed values for the source (1) in the field of NGC 205.

The peak flux density values from the IMAGR task are within 2σ of the JMFIT values, indicating that both methods are reliable for this image. The total flux density of 1.193 mJy, however, is much less than the NVSS value of 17.9 mJy which indicates that a lot of the flux is not being picked up in the observations. Again this could be due to some of the emission from the source being resolved out in the observations due to the high resolution.

As well as this object, a second field source labelled (2) in Figure 3.15 was imaged and can be seen in Figure 3.17.

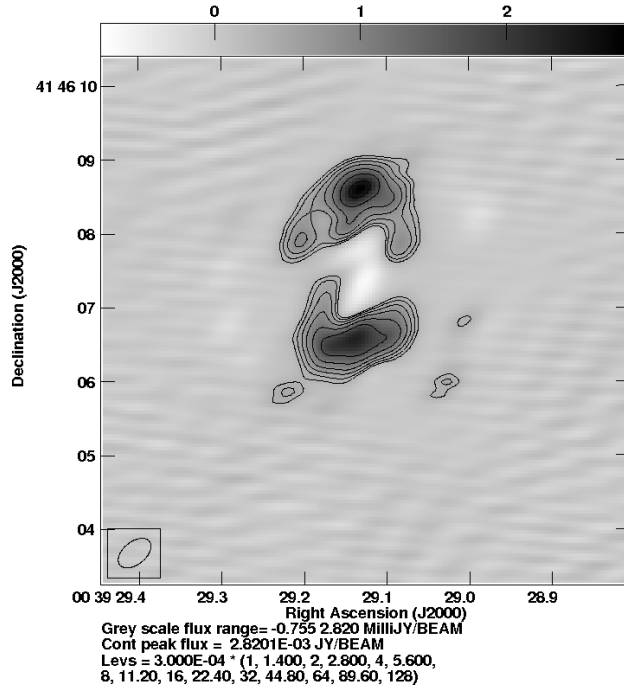


Figure 3.17: A source in the field of NGC 205, labelled (2) in Figure 3.15. The contours are $0.3 \times 1, 1.4, 2, 2.8, 4, 5.6, 8, 11.2, 16, 22.4, 32, 44.8, 64, 89.6, 128$ mJy/beam. The ellipse in the bottom left corner represents the beam size which is $0''.51 \times 0''.31$.

The NVSS total flux density value is 85.3 mJy with a spectral index of -0.8, and the observed values from the e-MERLIN observations can be seen in Table 3.7.

RA (HH:MM:SS)	00 39 29.132 \pm 4.95 s
DEC (DD:MM:SS)	41 46 08.53 \pm 42''34
Angular Distance from Pointing Centre (')	10.94
Peak Flux IMAGR (mJy/beam)	2.820
Total Flux NVSS (mJy)	85.3 \pm 3.1
RMS Noise (mJy/beam)	0.1225
Resolved?	Yes
Gaussian 1:	
Peak Flux JMFIT (mJy/beam)	1.08 \pm 0.04
Total Flux JMFIT (mJy)	50.51 \pm 1.91
Gaussian 2:	
Peak Flux JMFIT (mJy/beam)	2.51 \pm 0.09
Total Flux JMFIT (mJy)	5.83 \pm 0.29

Table 3.7: Observed values for the source (2) in the field of NGC 205.

The peak flux values observed by IMAGR are within 4σ of the JMFIT values, so are less accurate than other observations within this dataset. These calculations cannot be deemed to be completely accurate and so will not be included in any further analysis of the field source.

NGC 205 itself was not detected in the e-MERLIN observations. The NVSS does not provide a value for the total flux density of the galaxy at 1.4 GHz indicating that there were no detections in those observations. A 1.4 GHz VLA study (Brown et al. 2011) detected a small flux density of 0.1 mJy from NGC 205 which may explain why the galaxy has not been detected in the e-MERLIN observations as the observed flux is so low.

3.6 NGC 221 (0042+4051)

NGC 221 is another dwarf elliptical (E2) satellite galaxy of M31 at a distance of 0.78 Mpc. There are two main populations of stars within the galaxy; an intermediate-age population of around 2-8 Gyr and an older population of around 8-10 Gyr. There are also a smaller collection of younger stars distributed at all radii of ages 0.5-2 Gyr (Jones et al. 2015).

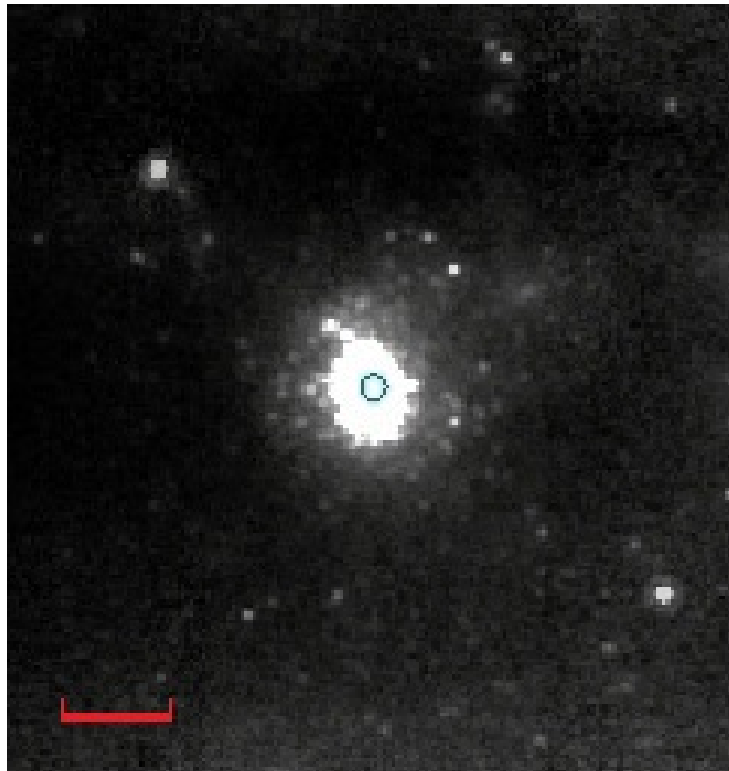


Figure 3.18: A $24\ \mu\text{m}$ *Spitzer* MIPS image of NGC 221. The red scale bar indicates an angular distance of $0''.02$.

Figure 3.18 shows a $24\ \mu\text{m}$ MIPS image of NGC 221 taken by *Spitzer* in 2004. The image shows some centrally concentrated infrared emission which is a result of thermal re-radiation of dust from young, hot stars in the central regions. This emission does not, however, correspond to radio emission from the galaxy as can be seen in Figure 3.19.

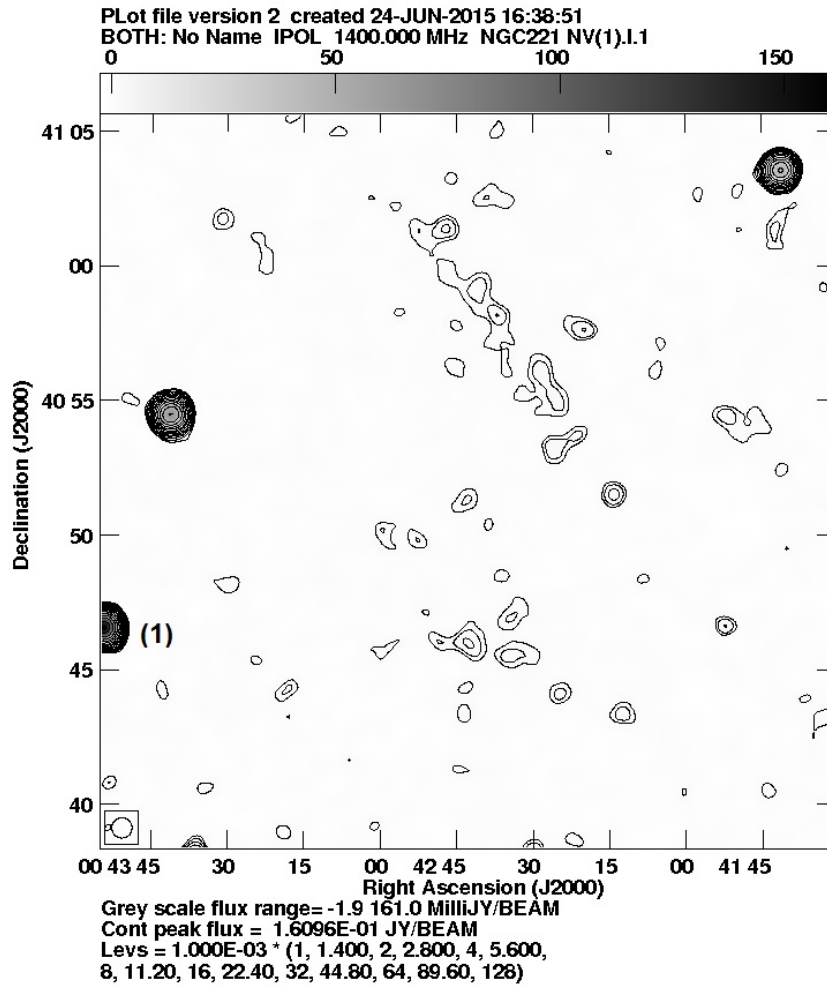


Figure 3.19: NVSS field of NGC 221. The contours are $0.9 \times 1, 1.4, 2, 2.8, 4, 5.6, 8, 11.2, 16, 22.4, 32, 44.8, 64, 89.6, 128$ mJy/beam. The circle at the bottom left corner represents the beams size which is $45'' \times 45''$.

Figure 3.19 shows the 1.4 GHz NVSS field of NGC 221 with a field of view equivalent to that of the e-MERLIN array. Again there appears to be little flux from the galaxy itself, but the field source labelled (1) has been imaged and can be seen in Figure 3.20.

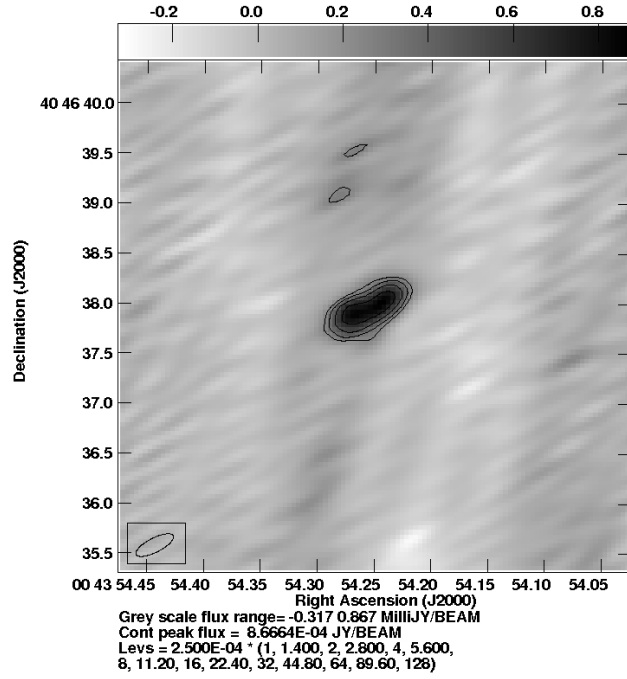


Figure 3.20: A source in the field of NGC 221, labelled (1) in Figure 3.19. The contours are $0.25 \times 1, 1.4, 2, 2.8, 4, 5.6, 8, 11.2, 16, 22.4, 32, 44.8, 64, 89.6, 128$ Jy/beam. The ellipse in the bottom left corner represents the beam size which is $0''.42 \times 0''.14$.

According to a study by Gelfand et al. (2005), this field source is a powerful compact radio source with a steep spectrum (compact steep-spectrum, or CSS) that turns over at low frequencies (around 500 MHz). It has a spectral index of -0.58 and is classified as a high-redshift radio galaxy. The NVSS total flux measurement is 167.9 mJy, and the observed values for the object can be seen in Table 3.8.

RA (HH:MM:SS)	00 43 54.256 \pm 6.22 s
DEC (DD:MM:SS)	40 46 37.94 \pm 49".64
Angular Distance from Pointing Centre (')	14.45
Peak Flux IMAGR (mJy/beam)	0.867
Peak Flux JMFIT (mJy/beam)	0.93 \pm 0.07
Total Flux NVSS (mJy)	167.9 \pm 5.1
Total Flux JMFIT (mJy)	3.877 \pm 0.329
RMS Noise (mJy/beam)	0.0574
Resolved?	Yes

Table 3.8: Observed values for the source in the field of NGC 221.

The peak flux density value observed by IMAGR is within 2σ of that observed by JMFIT, so the JMFIT values for the total flux density are deemed to be accurate. Compared to the NVSS total flux density of 167.9 mJy, our value of 3.877 mJy is very low and again indicates that a lot of the flux from the object is not being detected in our observations. Again this could be due to some of the emission from the source being resolved out in the observations due to the high resolution.

NGC 221 itself was not detected in the e-MERLIN observations. The NVSS does not provide a value for the total flux density of the galaxy at 1.4 GHz indicating that there were no detections in those observations. A 1.4 GHz VLA study by Brown et al. (2011) detected a small flux density of 0.7 mJy from NGC 221 which may explain why the galaxy has not been detected in the e-MERLIN observations as the observed flux density is so low.

3.7 M31 (0042+4116)

M31 resides at a distance of ~ 0.78 Mpc from the Milky Way, making it the closest spiral (SA(s)b) galaxy to our own (Galvin and Filipovic 2014). Star-formation rates in the galaxy are approximately $0.8 M_{\odot} \text{ yr}^{-1}$ (Robles-Valdez et al. 2014), which results in a radio flux at 1.4 GHz of 81 mJy due to the presence of HII regions and RSNe which are associated with the massive star formation. Lee and Lee (2014) carried out an optical study of the galaxy and confirmed a total of 156 SNR candidates, 77% of which are CC SNRs and therefore should exhibit radio emission. The majority of these reside in the spiral arms of the galaxy where the bulk of star formation occurs. Figure 3.21 shows a 1.4 GHz image of the central regions of M31.

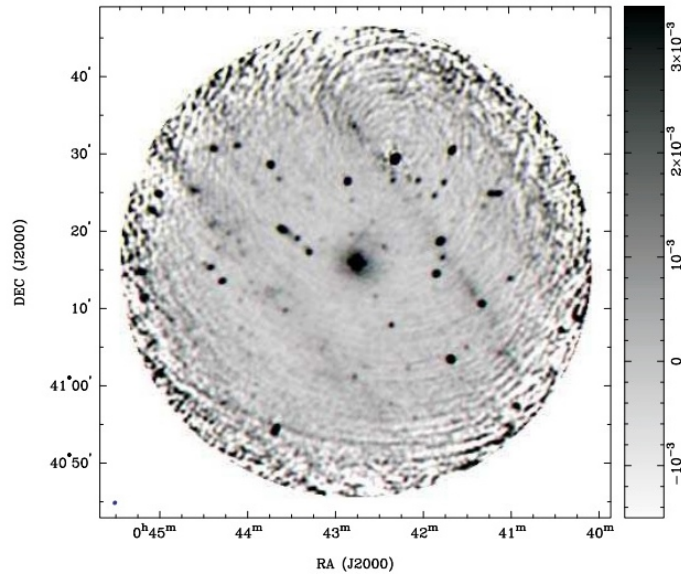


Figure 3.21: A 20 cm VLA image of the central regions of M31. The ellipse in the bottom left corner represents the beam size which is $35'' \times 32''$ and the rms noise is 0.12 mJy/beam. Image taken from Galvin et al. (2012).

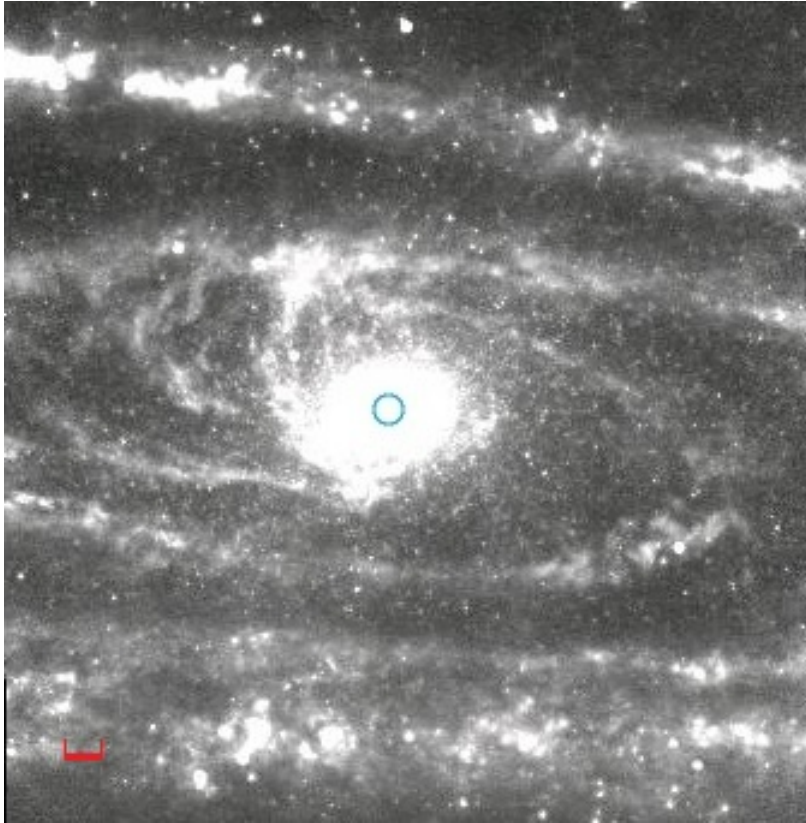


Figure 3.22: A $24\ \mu\text{m}$ *Spitzer* MIPS image of M31. The red scale bar indicates an angular distance of $0''.02$.

Figure 3.22 shows a $24\ \mu\text{m}$ MIPS image taken by *Spitzer* in 2004. Both the central regions and spiral arms are clearly visible as bright areas of infrared emission. These regions of the galaxy indicate the areas where recent star formation has occurred and therefore suggest the presence of young, hot stars.

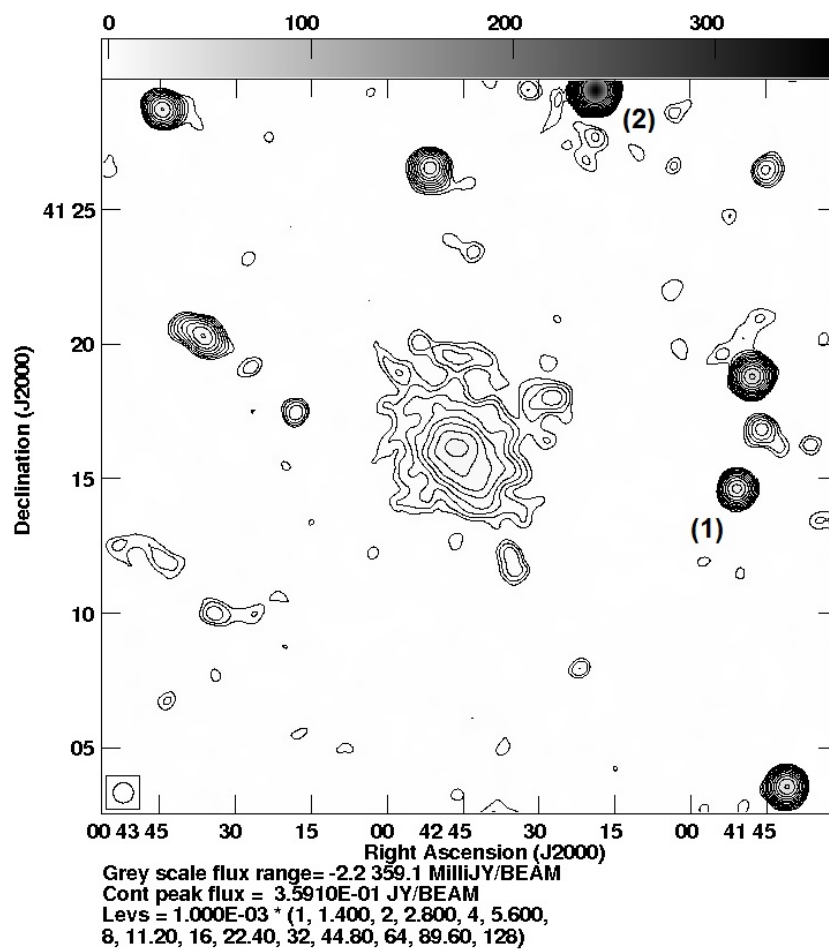


Figure 3.23: NVSS field of M31. The contours 1, 1.4, 2, 2.8, 4, 5.6, 8, 11.2, 16, 22.4, 32, 44.8, 64, 89.6, 128 mJy/beam. The circle at the bottom left corner represents the beams size which is $45'' \times 45''$.

Figure 3.23 shows the 1.4 GHz NVSS field of M31 with an equivalent field of view of the e-MERLIN array. Field sources have been labelled (1) and (2) within this map, and these sources have been imaged and can be seen in Figures 3.24 and 3.25 respectively.

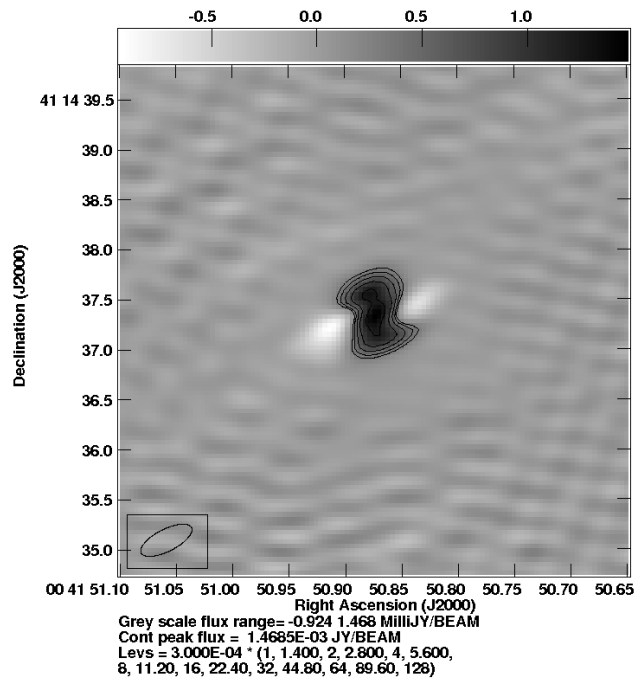


Figure 3.24: A source in the field of M31, labelled (1) in Figure 3.23. The contours are $0.3 \times 1, 1.4, 2, 2.8, 4, 5.6, 8, 11.2, 16, 22.4, 32, 44.8, 64, 89.6, 128$ mJy/beam. The ellipse in the bottom left corner represents the beam size which is $0''.56 \times 0''.22$.

The source (1) in Figure 3.24 is a possible AGN candidate in the field of M31. The NVSS total flux density value for the field source is 26.7 mJy and the observed values for the object can be seen in Table 3.9.

RA (HH:MM:SS)	00 41 50.873 \pm 3.37 s
DEC (DD:MM:SS)	41 14 37.36 \pm 69.91
Angular Distance from Pointing Centre (')	10.13
Peak Flux IMAGR (mJy/beam)	1.469
Peak Flux JMFIT (mJy/beam)	1.55 \pm 0.11
Total Flux NVSS (mJy)	26.7 \pm 0.9
Total Flux JMFIT (mJy)	2.849 \pm 0.287
RMS Noise (mJy/beam)	0.1372
Resolved?	Yes

Table 3.9: Observed values for the source (1) in the field of M31.

The IMAGR values for the peak flux density are within 1σ of the values observed by JMFIT, and are therefore deemed to be accurate for this observation. The JMFIT total flux density measurement is lower than the previous NVSS value, which again indicates that much of the flux is not being detected in the e-MERLIN observations. Again this could be due to some of the emission from the source being resolved out in the observations due to the high resolution.

A second field source within the field of M31 was also imaged, and can be seen in Figure 3.25.

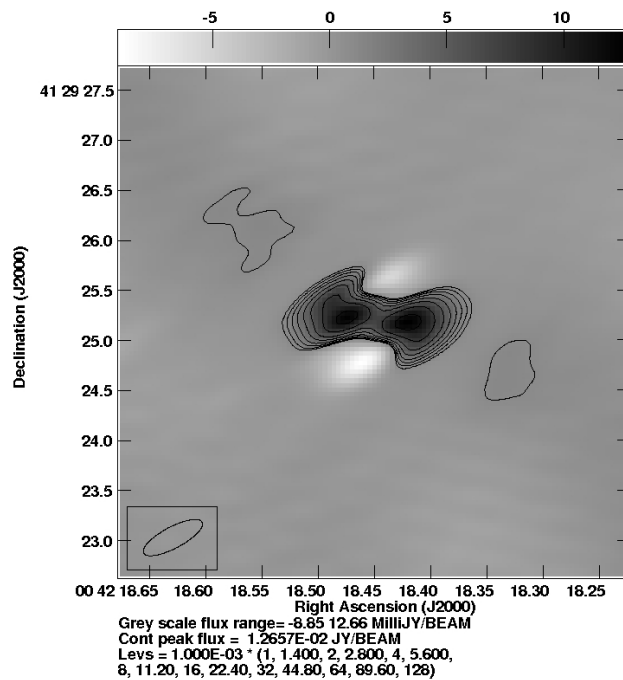


Figure 3.25: A source in the field of M31, labelled (2) in Figure 3.23. The contours are 1, 1.4, 2, 2.8, 4, 5.6, 8, 11.2, 16, 22.4, 32, 44.8, 64, 89.6, 128 mJy/beam. The ellipse in the bottom left corner represents the beam size which is $0''.66 \times 0''.21$.

The field source (2) is a compact steep-spectrum radio source with two components indicating a double-lobed structure (Rossetti et al. 2006) making the object a possible AGN candidate. This object has been previously observed at frequencies of 15 GHz and 8.5 GHz as part of the B3 - VLA CSS (Compact Steep Spectrum) sample, and Figure 3.26 shows the VLA image of the source.

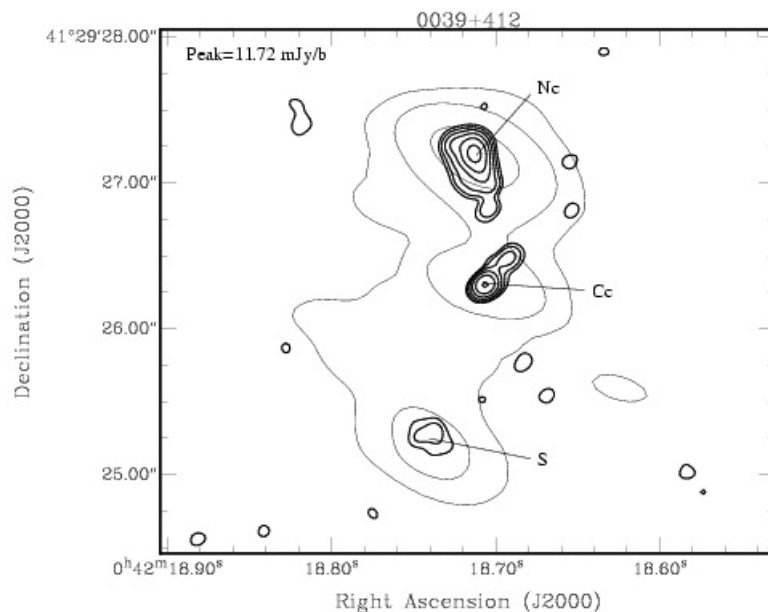


Figure 3.26: A source in the field of M31, labelled (2) in Figure 3.23. The thick contours represent 15 GHz observations, with the first contour representing 3 times the average rms noise level in the image (0.3 mJy/beam), and the contour levels increase by a factor of 2. The thin contours are representative of the 8.5 GHz observations, and the first contour is three times the average rms noise level (0.2 mJy/beam) with contour levels increasing by a factor of 8. The beam is circular with a size of $0''.12 \times 0''.12$. The peak flux density value is from observations at 15 GHz. Image taken from Rossetti et al. (2006)

Previous NVSS observations of the source give a total flux density value of 371.9 mJy, and the observed values for this field source can be seen in Table 3.10.

RA (HH:MM:SS)	00 42 18.447 \pm 7.11 s
DEC (DD:MM:SS)	41 29 25.21 \pm 19".43
Angular Distance from Pointing Centre (')	14.14
Peak Flux IMAGR (mJy/beam)	12.660
Total Flux NVSS (mJy)	371.9 \pm 11.2
RMS Noise (mJy/beam)	0.2101
Resolved?	Yes
Gaussian 1:	
Peak Flux JMFIT (Jy/beam)	9.90 \pm 0.44
Total Flux JMFIT (mJy)	7.43 \pm 0.63
Gaussian 2:	
Peak Flux JMFIT (mJy/beam)	11.74 \pm 0.39
Total Flux JMFIT (mJy)	62.99 \pm 2.48

Table 3.10: Observed values for the source (2) in the field of M31.

The IMAGR peak flux density values are within 3σ of the peak JMFIT value, and the measurements are therefore deemed to be accurate for this observation. The JMFIT value for the total flux density is very low in comparison to the NVSS value of 371.9 mJy however, which again implies that not all of the flux is being detected in the observations. This is confirmed by the 15 GHz VLA observations in which a peak flux of 11.72 was detected. According to Rossetti et al. (2006), the object has a spectral index greater than 0.5. If this is assumed to be correct, the peak flux density value at 1.4 GHz must be greater than 37.06 mJy, which is a larger value than was detected in the e-MERLIN observations. Again this could be due to some of the emission from the source being resolved out in the observations due to the high resolution.

M31 itself was undetected. The NVSS values for the total flux density are 81

mJy, whereas the value for the field source (2) is 371.9 mJy. As the field source is over four magnitudes brighter than the target galaxy itself, the clean components from the field source were removed during the imaging stage to see whether this emission was obscuring the observations of M31. After removing the flux from the field source, it was still not possible to detect the galaxy hence no images were produced.

3.8 NGC 278 (0052+4733)

NGC 278 is spiral galaxy (SAB(rs)b) that resides at a distance of 11.8 Mpc. It has a very compact structure and tightly wound spiral arms with a large presence of $H\alpha$ throughout the optical disk which indicates recent star formation in the form of HII regions (Garrido et al. 2003). The star formation rate of the galaxy from $H\alpha$ observations is $0.5 M_{\odot} \text{ yr}^{-1}$ (Mazzuca et al. 2008), which corresponds to a total flux density value of 142.2 mJy as a result of these HII regions and radio supernovae.



Figure 3.27: A $24 \mu\text{m}$ *Spitzer* MIPS image of NGC 278. The red scale bar indicates an angular distance of $0''.02$.

Figure 3.27 shows a $24 \mu\text{m}$ MIPS image of NGC 278 taken by *Spitzer* in 2004. The bright area includes both the spiral arms and the core of the galaxy, corresponding to its tightly wound morphology. The galaxy appears very bright at infrared wavelengths indicating the presence star forming regions within the

galaxy.

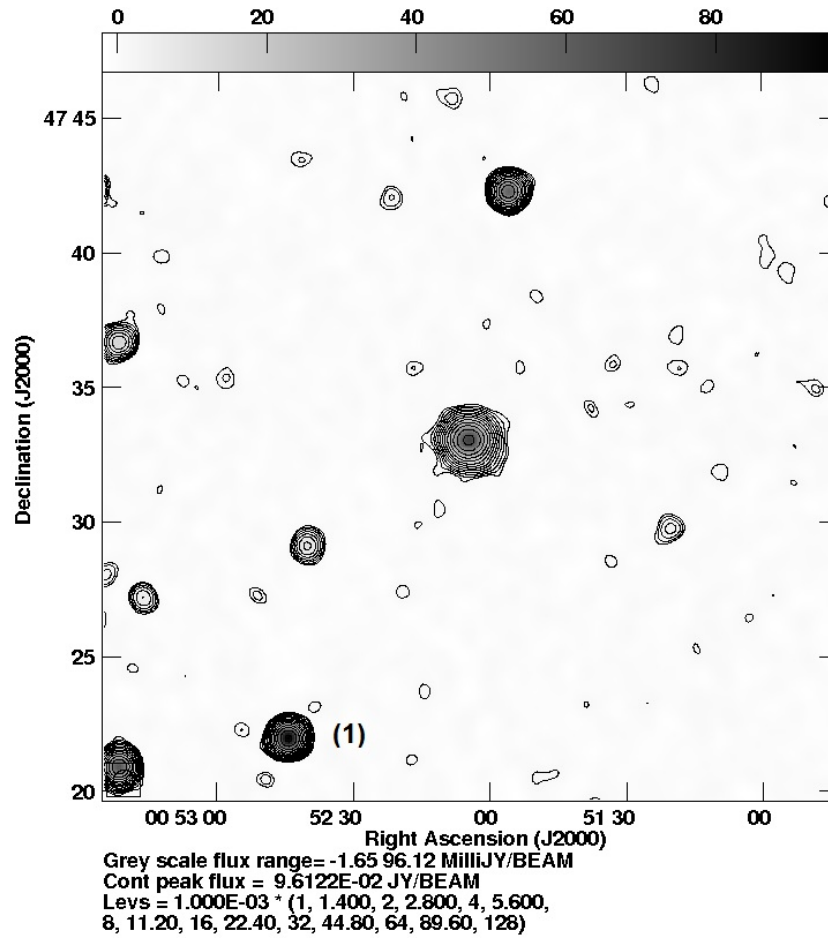


Figure 3.28: NVSS field of NGC 278. The contours are $0.9 \times 1, 1.4, 2, 2.8, 4, 5.6, 8, 11.2, 16, 22.4, 32, 44.8, 64, 89.6, 128$ mJy/beam. The circle at the bottom left corner represents the beams size which is $45'' \times 45''$.

Figure 3.28 shows the 1.4 GHz NVSS field of NGC 278 with an equivalent field of view to the e-MERLIN array. The compact, bright radio emission from the galaxy corresponds to the infrared emission in Figure 3.27, where star formation is occurring and hence HII regions and supernovae are present. A field source has been labelled (1) in this figure which has been imaged and can be seen in Figure 3.29.

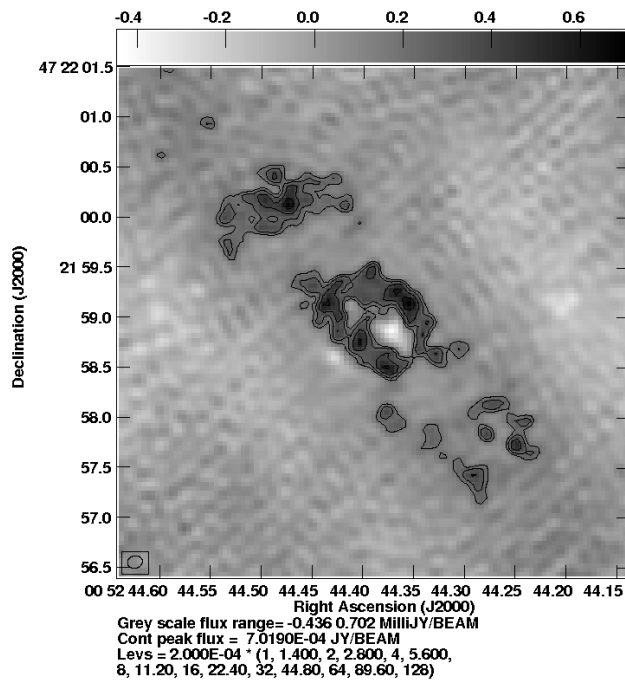


Figure 3.29: A source in the field of NGC 278, labelled (1) in Figure 3.28. The contours are $0.2 \times 1, 1.4, 2, 2.8, 4, 5.6, 8, 11.2, 16, 22.4, 32, 44.8, 64, 89.6, 128$ mJy/beam. The ellipse in the bottom left corner represents the beam size which is $0''.15 \times 0''.12$.

According to the CRATES (the Combined Radio All-sky Targeted Eight GHz Survey) study carried out by Healey et al. (2007), the field source (1) in Figure 3.29 is a flat-spectrum radio source with a spectral index of -0.4. The NVSS value for the total flux density is 100 mJy, and the observed values for this source can be seen in Table 3.11.

RA (HH:MM:SS)	00 52 44.715 \pm 537.84 s
DEC (DD:MM:SS)	47 22 02.83 \pm 644''40
Angular Distance from Pointing Centre (')	12.95
Peak Flux IMAGR (mJy/beam)	0.702
Peak Flux JMFIT (mJy/beam)	0.73 \pm 0.09
Total Flux NVSS (mJy)	100 \pm 3
Total Flux JMFIT (mJy)	77.31 \pm 4.63
RMS Noise (mJy/beam)	0.0624
Resolved?	Yes

Table 3.11: Observed values for the source in the field of NGC 278.

The peak flux value created by IMAGR is within 1σ of that observed by the JMFIT task and so both values are deemed to be accurate for this observation. The total flux value, however, is lower than the expected value from the NVSS measurement of 100 mJy. This again confirms that the e-MERLIN observations are not detecting all of the flux from these objects. Again this could be due to some of the emission from the source being resolved out in the observations due to the high resolution.

NGC 278 itself was undetected in the observations. Although the total flux density from NVSS measurements for the galaxy is 142.2mJy compared to 100 mJy for the field source, NGC 278 has a larger angular scale of $149''3 \times 146''3$ compared to $6''3 \times 1''0$. This may explain why the field source has been detected despite having a lower total flux density value than NGC 278 as the emission is being resolved out.

3.9 NGC 7741 (2343+2604)

NGC 7741 is a barred spiral galaxy (SB(s)cd) at a distance 14.3 Mpc. The galaxy has short spiral arms, within which are bright HII regions indicating areas of recent star formation and $H\alpha$ emission is present throughout the disk (Garrido et al. 2002). The star formation rate of the galaxy from $H\alpha$ observations is $1.8 M_{\odot} \text{ yr}^{-1}$ (Martinet and Friedli 1997) which results in a radio flux density of 15 mJy.

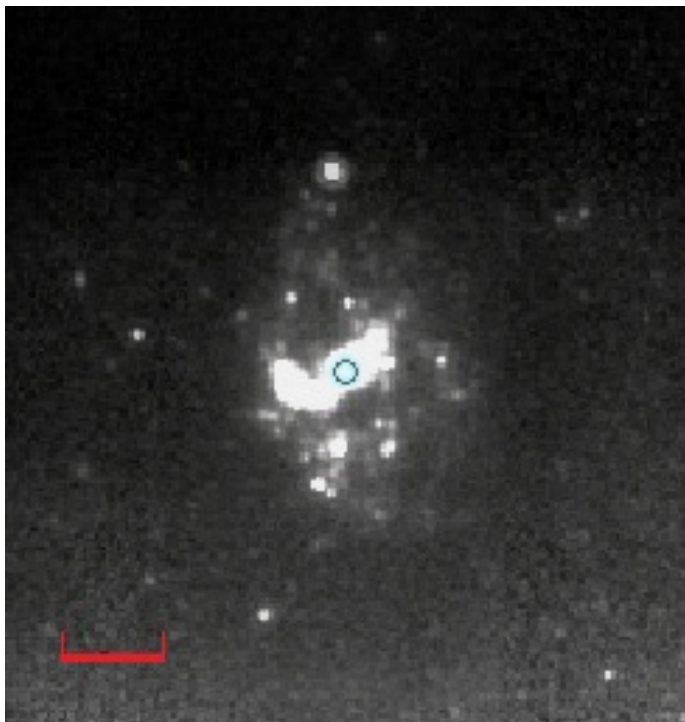


Figure 3.30: A 24μ *Spitzer* MIPS image of NGC 7817. The red scale bar indicates an angular distance of $0''.02$.

Figure 3.30 shows a $24 \mu\text{m}$ MIPS image of NGC 7741 taken by *Spitzer* in 2004. The central regions are clearly visible within the infrared observations, and diffuse emission corresponding to the spiral arms is also apparent in the image. These bright areas indicate recent star formation as thermal re-radiation of dust from young, massive O and B-type stars causes emission at infrared wavelengths.

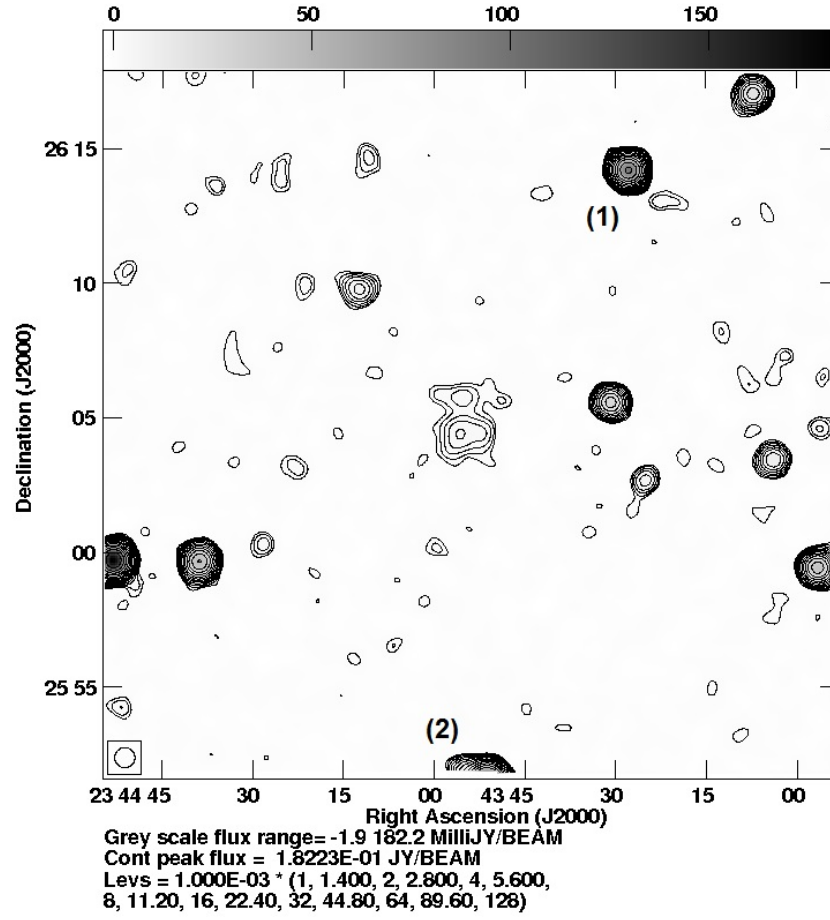


Figure 3.31: NVSS field of NGC 7741. The contours are $0.9 \times 1, 1.4, 2, 2.8, 4, 5.6, 8, 11.2, 16, 22.4, 32, 44.8, 64, 89.6, 128$ mJy/beam. The circle at the bottom left corner represents the beams size which is $45'' \times 45''$.

Figure 3.31 shows the 1.4 GHz NVSS field of NGC 7741, with a corresponding field of view to that of the e-MERLIN array. There is clearly some radio emission from the central regions of the galaxy, although emission from the spiral arms is less apparent at this frequency. Two field sources have been labelled (1) and (2) within the figure which have been imaged and can be seen in Figures 3.32 and 3.33 respectively.

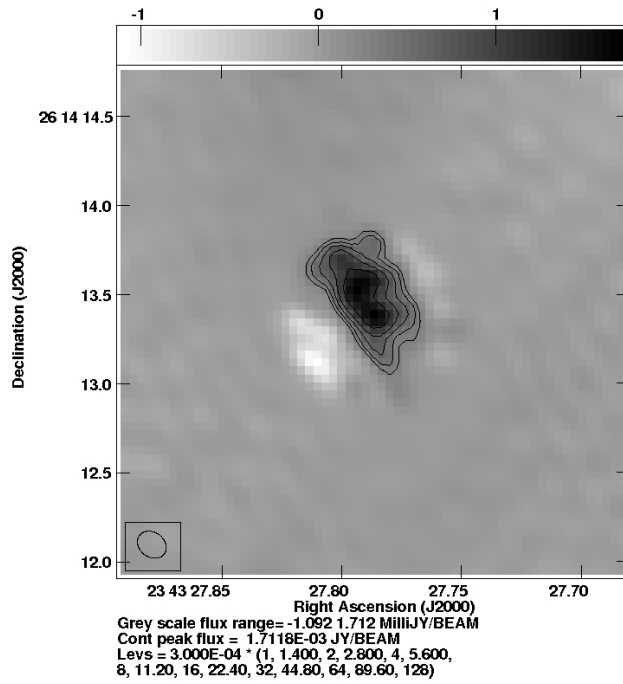


Figure 3.32: A source in the field of NGC 7741 labelled (1) in Figure 3.31. The contours are $0.3 \times 1, 1.4, 2, 2.8, 4, 5.6, 8, 11.2, 16, 22.4, 32, 44.8, 64, 89.6, 128$ mJy/beam. The ellipse in the bottom left corner represents the beam size which is $0''.17 \times 0''.14$.

According to the CRATES survey carried out by Healey et al. (2007), the field source (1) is a flat-spectrum radio source with a spectral index of -0.36. The NVSS value for the total flux density is 100.6 mJy, and the observed values for the object can be seen in Table 3.12.

RA (HH:MM:SS)	23 43 27.790 \pm 1.84 s
DEC (DD:MM:SS)	26 14 13.50 \pm 32''63
Angular Distance from Pointing Centre (')	11.35
Peak Flux IMAGR (mJy/beam)	1.712
Peak Flux JMFIT (mJy/beam)	1.71 \pm 0.08
Total Flux NVSS (mJy)	100.6 \pm 3.1
Total Flux JMFIT (mJy)	9.379 \pm 0.509
RMS Noise (mJy/beam)	0.0883
Resolved?	Yes

Table 3.12: Observed values for the source (1) in the field of NGC 7741.

The IMAGR values for the peak flux density are within 1σ of the JMFIT values and therefore the calculations are deemed to be accurate for these observations. The total flux density value of 9.4 mJy, however, are much lower than the NVSS value of 101 mJy. This, again, implies that not all of the flux from the object is being detected in the e-MERLIN observations. This could be due to some of the emission from the source being resolved out in the observations due to the high resolution of the e-MERLIN observations.

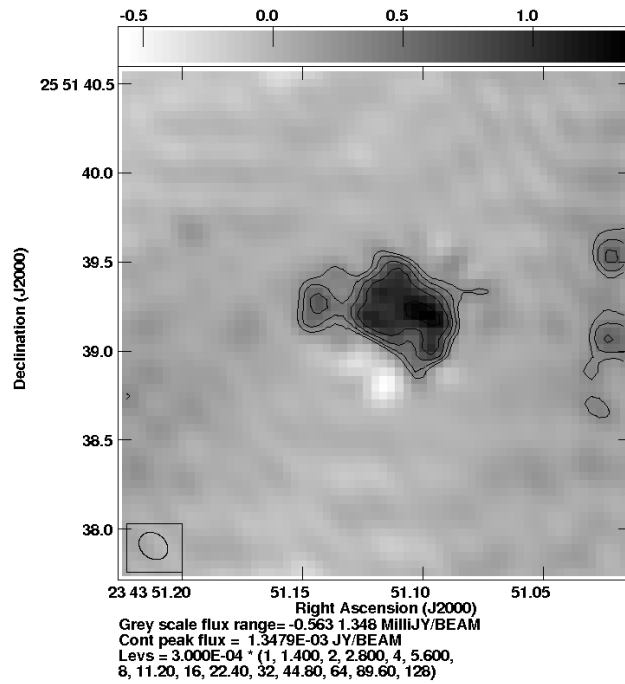


Figure 3.33: A source in the field of NGC 7741 labelled (2) in Figure 3.31. The contours are $0.3 \times 1, 1.4, 2, 2.8, 4, 5.6, 8, 11.2, 16, 22.4, 32, 44.8, 64, 89.6, 128$ mJy/beam. The ellipse in the bottom left corner represents the beam size which is $0''.17 \times 0''.14$.

Figure 3.33 shows the source (2) in the field of NGC 7741. A spectral index of -0.7 was observed from the NVSS 1.4 GHz and Green Bank 4.85 GHz observations (Gregory and Condon 1991). The NVSS total flux density value is 116.3 mJy and the observed values from the e-MERLIN observations can be seen in Table 3.13.

RA (HH:MM:SS)	23 43 51.110 \pm 5.28 s
DEC (DD:MM:SS)	25 51 39.23 \pm 44''82
Angular Distance from Pointing Centre (')	12.92
Peak Flux IMAGR (mJy/beam)	1.348
Peak Flux JMFIT (mJy/beam)	1.28 \pm 0.10
Total Flux NVSS (mJy)	116.3 \pm 4.5
Total Flux JMFIT (mJy)	11.80 \pm 1.00
RMS Noise (mJy/beam)	0.0773
Resolved?	Yes

Table 3.13: Observed values for the source (2) in the field of NGC 7741.

The value for the peak flux density from IMAGR is within 3σ of the JMFIT values and so both calculations are deemed to be accurate for this observation. The total flux density value of 11.8 mJy is much lower than the NVSS value of 116.3 mJy, which again indicates that not all of the flux from the object is being detected in the observations. This could be due to some of the emission from the source being resolved out in the observations due to the high resolution.

NGC 7741 itself was undetected in the observations. The NVSS total flux density value of the galaxy is 15 mJy compared to the field sources (1) and (2) which have NVSS flux density measurements of 101 mJy and 116 mJy respectively. Because the field sources have flux densities around 7 magnitudes higher than the target galaxy, their clean components were removed during the imaging stage to see whether this emission was obscuring the observations of NGC 7741. After removing the flux from the field source, it was still not possible to detect the galaxy, hence no images were produced.

3.10 NGC 7798 (2359+2045)

NGC 7798 is a spiral galaxy (SBc) which resides at a distance of 32.6 Mpc. The galaxy exhibits recent star formation along the spiral arms, and $H\alpha$ emission is apparent throughout the galaxy, although radio emission is seen as a strong nuclear point source with some faint diffuse emission corresponding to the spiral arms (Schmitt et al. 2006a). A $H\alpha$ study carried out by Schmitt et al. (2006b) determined a star formation rate for the galaxy of $1.63 M_{\odot} \text{ yr}^{-1}$. The NVSS value for the total flux density of the galaxy is 37.5 mJy.

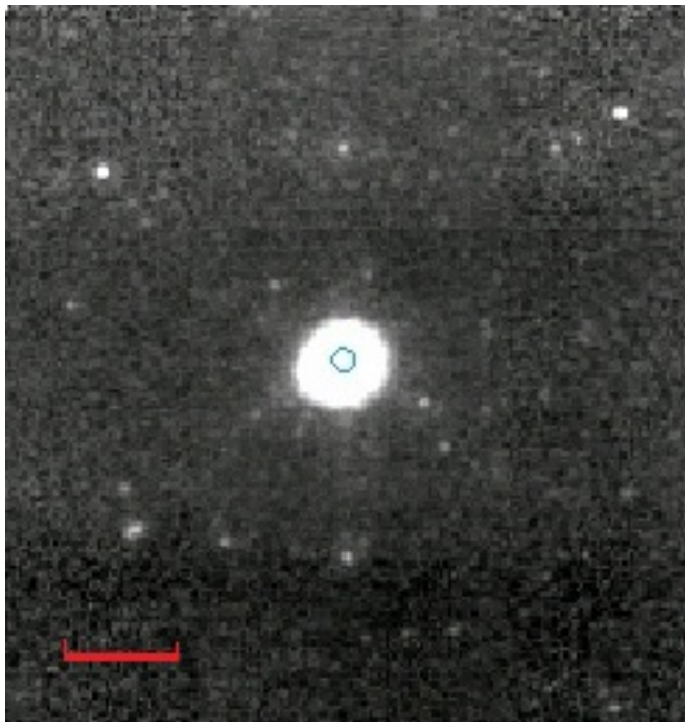


Figure 3.34: A 24 μm *Spitzer* MIPS image of NGC 7798. The red scale bar indicates an angular distance of 0''.02.

Figure 3.34 shows a 24 μm MIPS image of NGC 7798 taken by *Spitzer* in 2006. The spiral arms are not apparent individually, although with a relatively small angular size of $108'' \times 77''$ it is probable that like NGC 278, the spiral arms are included in the bright central region of the image.

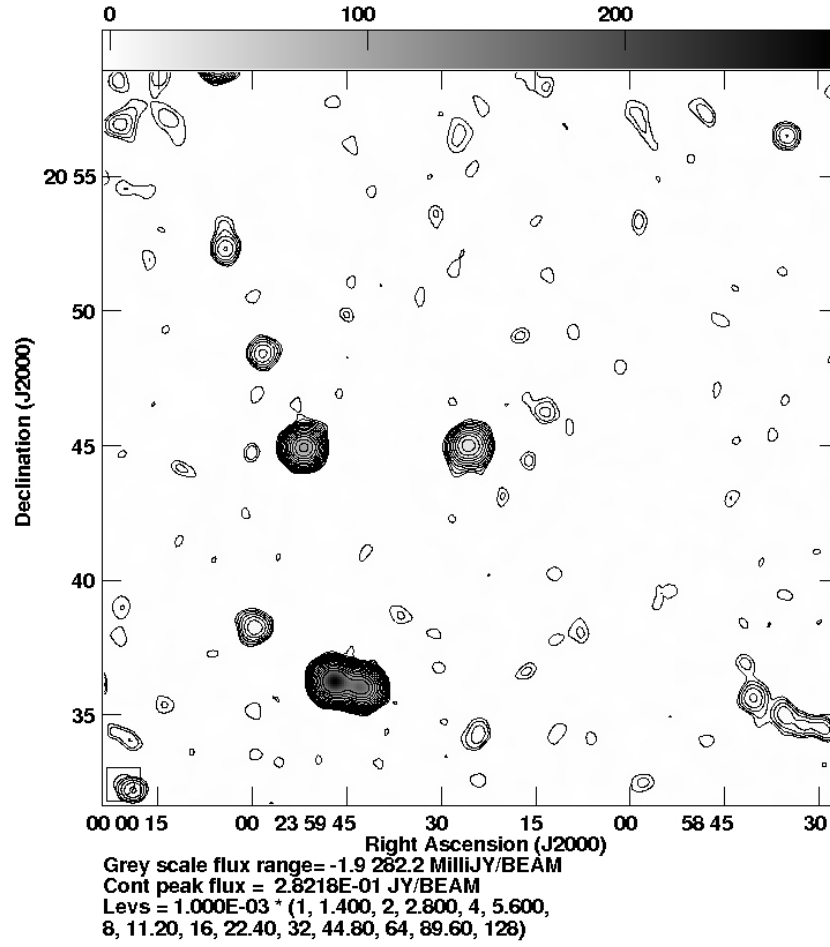


Figure 3.35: NVSS field of NGC 7798. The contours are $0.9 \times 1, 1.4, 2, 2.8, 4, 5.6, 8, 11.2, 16, 22.4, 32, 44.8, 64, 89.6, 128$ mJy/beam. The circle at the bottom left corner represents the beams size which is $45'' \times 45''$.

Figure 3.35 shows the 1.4 GHz NVSS field of NGC 7798 with an equivalent field of view to that of the e-MERLIN array. The morphology of the radio emission appears similar to the infrared image in that the emission is concentrated within a compact region, and the spiral arms are not visible individually. Neither NGC 7798 nor any field sources were detected in the observations.

3.11 Summary

This chapter has presented images and observed properties from the e-MERLIN observations of any compact objects within the target galaxies or surrounding fields.

Of the ten target galaxies, only IC10 was detected in the e-MERLIN observations. To identify a reason for this, the NVSS and e-MERLIN observations were analysed by comparing the beam sizes to the flux densities for each galaxy. Table 3.14 shows the results of the analysis. The flux density per e-MERLIN beam was found by first calculating how many e-MERLIN beams would fit inside one NVSS beam for each observation. Then, assuming that the flux is distributed uniformly throughout the NVSS beam, the total flux density for each galaxy (as seen in Table 3.1) was divided by the number of e-MERLIN beams to identify how much flux is expected.

Galaxy	NVSS Beam Size (")	e-MERLIN Beam Size (")	e-MERLIN Ex- pected Flux per Beam (mJy)	RMS Noise (mJy/beam)
NGC 7817	45×45	0.98×0.11	1.789×10^{-3}	0.1253
IC10	45×45	0.36×0.10	2.299×10^{-3}	0.1194
NGC 147	45×45	0.19×0.11	-	0.0905
NGC 185	45×45	0.13×0.12	-	0.0748
NGC 205	45×45	0.46×0.11	-	0.1450
NGC 221	45×45	0.39×0.11	-	0.1544
M31	45×45	0.36×0.13	1.872×10^{-3}	0.1253
NGC 278	45×45	0.13×0.11	1.004×10^{-3}	0.0727
NGC 7741	45×45	0.17×0.11	1.385×10^{-4}	0.1030
NGC 7798	45×45	0.89×0.11	1.813×10^{-3}	0.0975

Table 3.14: This table shows both the NVSS and e-MERLIN beam sizes for the observations of each galaxy within the sample. The e-MERLIN expected flux per beam can also be seen, as well as the RMS noise level for each observation.

If the RMS noise level is greater than the e-MERLIN flux density expectation for the observations, then we would not expect the galaxy to be detected. In some cases, for example IC10 in which a compact object was detected, the flux limit is still lower than the RMS noise level. Because the limit assumes a uniform distribution of flux, if a compact area is apparent then it may still be detected provided that the peak flux density is greater than the noise level. For this reason, it is possible to assume that for the other 9 galaxies, there are no compact objects present that have a peak flux density greater than the noise levels exhibited in the observations.

The values in Table 3.14 imply that the target galaxies have not been detected in the observations as the emission has been resolved out. The NVSS has a much

CHAPTER 3. RESULTS

lower resolution and therefore has observed values for the galaxies as the flux has not been resolved out in the observations.

Chapter 4 discusses the results of these observations in greater detail and compares the findings to previous studies.

Chapter 4

Discussion

This chapter compares the results from the e-MERLIN observations to previous studies of the galaxies included in the sample. The flux limitations are explored further to include analysis of radio-loud objects such as radio supernovae remnants as well as active galactic nuclei to compare the findings to our expectations of the galaxies. An estimate of the star formation and supernovae rates has also been made using the radio luminosities of the galaxies.

4.1 Galaxy Luminosities

From the calculations in Section 3, Table 3.14, it is possible to state that we would not expect any of the galaxies to be significantly detected at the noise levels achieved in these e-MERLIN observations assuming that the flux is distributed evenly throughout the galaxies that have been detected by the NVSS (Condon et al. 1998). Apart from IC10, none of the galaxies contain compact objects with peak flux densities brighter than the 3σ detection levels of the observations. It is predicted that the non-detections are a result of observations that are too shallow or a too high resolution resulting in the resolving out of much of the emission.

To help understand further why no compact objects have been detected in any galaxies other than IC10, the luminosity of each galaxy can be calculated from both the e-MERLIN and NVSS observations as a comparison. The luminosity values can then be further analysed to place limits on whether any AGN or SNRs should have been detected. It is possible to find the luminosity of each galaxy from the flux density using the equation

$$L_\nu = 4\pi D^2 S_\nu \quad (4.1)$$

where L_ν is the spectral luminosity in W Hz^{-1} , D is the distance to the galaxy in m and S_ν is the flux density in $\text{W m}^{-2} \text{Hz}^{-1}$. The expected luminosity, at the distance of each galaxy, provides a lower limit at which the equivalent flux density could be detected by the e-MERLIN array, if greater than the RMS noise level of the observation. The actual radio luminosities have been calculated as these can be used to determine the number of possible supernova remnants within the galaxies. These values for each galaxy can all be seen in Table 4.1.

4.1. GALAXY LUMINOSITIES

Galaxy	Distance (Mpc)	RMS Noise (mJy/beam)	Expected e-MERLIN Flux Density (mJy/beam)*	Expected e-MERLIN Luminosity (W Hz ⁻¹)*	Known Radio Luminosity (W Hz ⁻¹) **
NGC 7817	25.95	0.1253	1.789×10^{-3}	1.441×10^{17}	2.707×10^{21}
IC10	0.89	0.1194	2.299×10^{-3}	2.179×10^{14}	1.225×10^{19}
NGC 147	0.77	0.0905	-	-	-
NGC 185	0.74	0.0748	-	-	-
NGC 205	0.81	0.1450	-	-	-
NGC 221	0.78	0.1544	-	-	-
M31	0.79	0.1253	1.872×10^{-3}	1.398×10^{14}	6.049×10^{18}
NGC 278	11.80	0.0727	1.004×10^{-3}	1.673×10^{16}	2.369×10^{21}
NGC 7741	14.28	0.1030	1.385×10^{-4}	3.379×10^{15}	3.659×10^{20}
NGC 7798	32.60	0.0975	1.813×10^{-3}	2.306×10^{17}	4.769×10^{21}

Table 4.1: The RMS noise, expected flux density, expected luminosity and actual radio luminosity of each target galaxy, taking into account the distance to each. NGC 147, 185, 205 and 221 have been left blank as the NVSS did not detect these galaxies, and therefore no total flux density values were given.

* Assuming the flux detected by the NVSS is distributed smoothly across the beam, the NVSS flux density values have been compared to an e-MERLIN sized beam to calculate the minimum flux density we would expect to detect with e-MERLIN.

**The known radio luminosity was calculated using the total flux density values from the NVSS with a resolution of $45'' \times 45''$.

The expected luminosity (Table 4.1, column 5) is an equivalent value to the flux densities that we would expect to see with the e-MERLIN telescope if the peak NVSS flux density measures were distributed smoothly over the NVSS beam and observed with the equivalent angular resolution of these e-MERLIN obser-

vations. As this value is much lower than the actual radio luminosity calculated from the NVSS observations, it tells us that much of the emission from the target galaxies is being resolved out in the e-MERLIN observations due to the high resolution of the array.

4.2 Detecting Active Galactic Nuclei

4.2.1 Radio-Loud AGN

A faint radio-loud AGN has a typical 1.4 GHz luminosity of 10^{25} W Hz⁻¹ (Smolcic et al. 2015) which is equivalent to a total flux density of 209 Jy at the median LeMMINGs sample distance of 20 Mpc, although these types of radio sources are usually far more distant. By converting this value to a flux density measurement at the distance to each galaxy it will be possible to determine whether or not we would expect to detect any AGN that may be present in the target galaxies. This can be calculated using the following equation

$$S_{\nu} = \frac{L_{\nu}}{4\pi D^2} \quad (4.2)$$

where L_{ν} is the spectral luminosity, D is the distance to the object and S_{ν} is the flux density.

At the distances to each galaxy in the sub-sample, the typical radio-loud AGN flux density ranges between 7 - 152,000 Jy which are extremely large values. These values are all well above the 3σ noise values for all ten target galaxies and would definitely have been detected in the e-MERLIN observations, as well as in previous studies. The radio galaxy Centaurus A has a distance of 3.69 Mpc and was studied by (Condon et al. 1996) using the VLA at 1.4 GHz. The galaxy has a relatively low luminosity of 9.31×10^{21} W Hz⁻¹ and the study detected a flux density value of 5.7 Jy. The average galaxy distance within this sub-sample is 8.9 Mpc so this confirms that even a relatively low luminosity radio-loud AGN

within the sub-sample median distance should be detected above the sensitivity limits. For this reason it is possible to conclude that there are no radio-loud AGN present in any of the galaxies as none have been detected.

4.2.2 Radio Quiet AGN

Radio quiet AGN have a radio luminosity range of 10^{19} - 10^{22} W Hz⁻¹ (Ho and Peng 2001) at 6 cm. We assume a spectral index of -0.7 for the radio emission from radio-quiet AGN, and therefore the equivalent 20 cm luminosity range is 1.8×10^{18} - 1.8×10^{21} W Hz⁻¹. This value is equal to a flux density range of 0.0376 - 37.6 mJy at the LeMMINGs sample median distance of 20 Mpc. Using the same method as in Equation 4.2, the range of flux densities between the higher and lower luminosity radio-quiet AGN at the distance to each galaxy can be calculated to see if we would expect to detect any in the e-MERLIN observations. The results of these calculations can be seen in Table 4.2.

Galaxy	Distance (Mpc)	RMS Noise (mJy/beam)	Radio-Quiet AGN Flux Density Range (mJy)*
NGC 7817	25.95	0.1253	0.02 - 22.34
IC10	0.89	0.1194	19.00 - 1.90×10^4
NGC 147	0.77	0.0905	25.50 - 2.55×10^4
NGC 185	0.74	0.0748	27.31 - 2.73×10^4
NGC 205	0.81	0.1450	22.81 - 2.28×10^4
NGC 221	0.78	0.1544	25.06 - 2.51×10^4
M31	0.79	0.1253	24.10 - 2.41×10^4
NGC 278	11.80	0.0727	0.11 - 108.00
NGC 7741	14.28	0.1030	0.07 - 73.79
NGC 7798	32.60	0.0975	0.01 - 14.15

Table 4.2: The expected flux density of a radio-quiet AGN if located at the distance of each target galaxy.

*Assuming radio-quiet AGN have radio luminosities in the order of $1.8 \times 10^{18} - 1.8 \times 10^{21} \text{ W Hz}^{-1}$

For NGC 7817, 7741 and 7798 the noise levels are higher than the lowest expected flux density from a radio-quiet AGN. In these cases, it is possible that an AGN may be present but not detected in the observations, although previous studies of the galaxies show that they appear to be normal galaxies and do not contain an active nucleus. A study by Desroches and Ho (2009) concluded that NGC 7817 is not an AGN candidate and therefore we can assume that no radio-quiet AGN is present. According to a study by Hernández-Toledo et al. (2007), NGC 7817 does not contain an active nucleus, and other work by Contini et al. (1998) concluded that NGC 7798 does not exhibit activity in the form of an AGN. From this it is possible to conclude that none of the ten target galaxies contain

a radio-quiet AGN.

4.3 Detecting Supernovae Remnants

The non-thermal radio emission from normal galaxies is primarily from core-collapse supernovae and supernovae remnants in regions of recent star formation. The compactness and typically high flux densities of these objects make them relatively easy to detect in radio observations of nearby galaxies. The spectral luminosity of a supernovae remnant at 20 cm is generally between 10^{16} and 10^{21} W Hz⁻¹ (Chomiuk and Wilcots 2009), and the flux density values have been calculated from this range using the same method as in Equation 4.2. A plot showing SNR flux density against distance for low-luminosity SNRs can be seen in Figure 4.1.

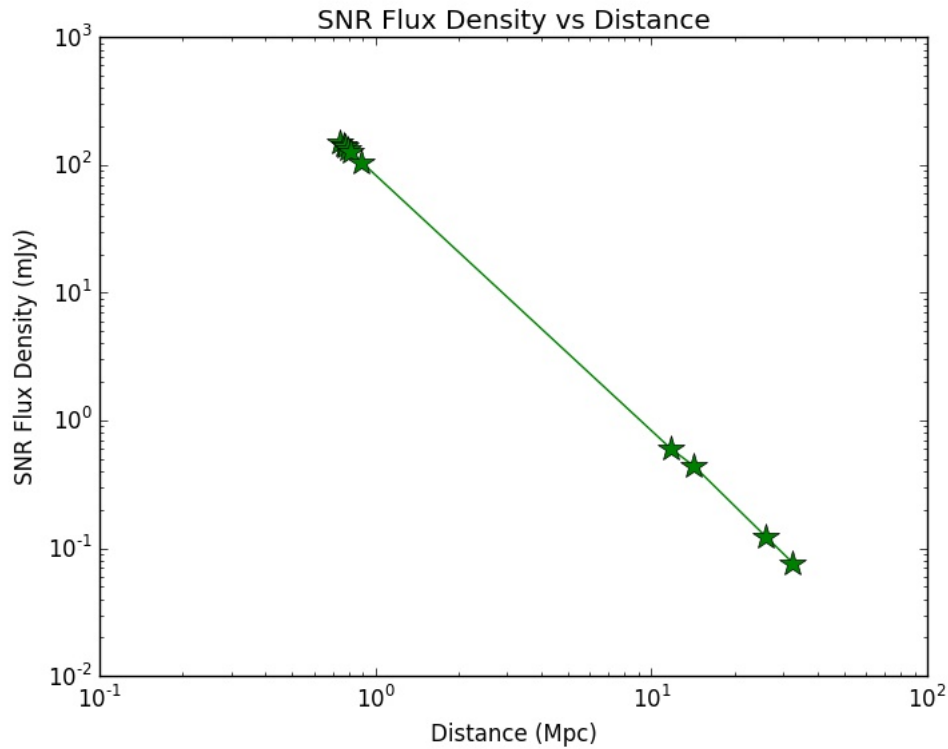


Figure 4.1: A plot of SNR flux density in mJy against distance (assuming a low-luminosity SNR exhibits a luminosity of $10^{16} \text{ W Hz}^{-1}$). Green stars correspond to individual galaxies within the sample for this thesis.

By calculating the flux densities produced from SNRs at the distance of each target galaxy, it is possible to say whether we would expect to detect any SNR emission or not. The results of these calculations, including both low and high luminosity SNRs, can be seen in Table 4.3.

4.3. DETECTING SUPERNOVAE REMNANTS

Galaxy	Distance (Mpc)	RMS Noise (mJy/beam)	SNR Flux Density Range (mJy) *
NGC 7817	25.95	0.1253	$1.241 \times 10^{-4} - 1.241 \times 10^1$
IC10	0.89	0.1194	$1.055 \times 10^{-1} - 1.055 \times 10^4$
NGC 147	0.77	0.0905	$1.417 \times 10^{-1} - 1.417 \times 10^4$
NGC 185	0.74	0.0748	$1.517 \times 10^{-1} - 1.517 \times 10^4$
NGC 205	0.81	0.1450	$1.267 \times 10^{-1} - 1.267 \times 10^4$
NGC 221	0.78	0.1544	$1.392 \times 10^{-1} - 1.392 \times 10^4$
M31	0.79	0.1253	$1.339 \times 10^{-1} - 1.339 \times 10^4$
NGC 278	11.80	0.0727	$6.003 \times 10^{-4} - 6.003 \times 10^1$
NGC 7741	14.28	0.1030	$4.406 \times 10^{-4} - 4.406 \times 10^1$
NGC 7798	32.60	0.0975	$7.683 \times 10^{-5} - 7.683$

Table 4.3: The expected flux density of a SNR if located at the distance of each target galaxy.

*Assuming a SNR luminosity range of 10^{16} to 10^{21} W Hz⁻¹ (Chomiuk and Wilcots 2009).

A major issue when detecting compact objects with the LeMMINGs project is the amount of time spent on each source (i.e. the resultant image sensitivity) as well as image fidelity limitations imposed by the limited (u,v) coverage of the snapshot imaging mode of observation. With just 40 minutes of observing time on each galaxy, not all of the flux will have been detected and some compact objects may remain undetected regardless of the flux density limits of the array due to image fidelity limitations. From both the SNR flux densities in Table 4.3 and the luminosity and flux density expectations of the array, it is possible to speculate whether non-detections are a result of the limitations of the (u,v) coverage, the resulting image sensitivity of each target or high resolution of e-MERLIN observations.

Individual analysis for each galaxy is presented in sections 4.4 to 4.13.

4.4 NGC 7817

The 3σ noise level of the NGC 7817 observation is 0.3759 mJy/beam. At the distance to the galaxy, a SNR must have a luminosity of 3.029×10^{19} W Hz⁻¹ to be accurately detected above the 3σ noise level. The maximum luminosity that is expected from a SNR is 10^{21} W Hz⁻¹ so providing there is no significant diffuse confusing emission in the galaxy, the (u,v) coverage will be sufficient to image a point source such as a young SNR. A study of NGC 7817 by Miller and Veilleux (2003) states that there are bright HII regions within the galaxy, although no SNRs were detected. Another study by Condon et al. (2002) concluded that the main contribution to the 1.4 GHz radio emission is from stellar emission associated with star-formation, and there are no references to SNRs within the galaxy. It is possible that there are SNRs present, although more observations of this galaxy are needed to conclude whether there are no SNRs or whether the e-MERLIN observations were not adequately deep.

4.5 IC10

The 3σ noise level of the IC10 observations is 0.3582 mJy/beam. A SNR at an equivalent distance to the galaxy must have a luminosity greater than 2.760×10^{16} W Hz⁻¹ to be accurately detected. Further analysis of the compact object that was detected in IC10 (Figure 3.7) confirm that the source is a HII region rather than a SNR, as found in a recent study by Westcott (2014). The e-MERLIN observations show it has an equivalent luminosity of 1.526×10^{17} W Hz⁻¹ which is above the detection level. The study by Westcott (2014) found a total of 8 compact objects in IC10 including 4 HII regions and 4 SNRs. Of the SNRs, all had a peak flux density greater than the 3σ noise levels in the e-MERLIN

observations. A recent study of radio sources in M82 by Fenech et al. (2008) found a mean SNR diameter of 2.9 pc which equates to an angular diameter of $0''.67$ at a distance of 0.89 Mpc. The e-MERLIN beam size of $0''.36 \times 0''.1$ in the IC10 observations means that some of the smooth emission from SNRs of this diameter would be resolved out. A SNR of $0''.67$ diameter must have a flux density of 1.07 mJy to be detected given the resolution of the e-MERLIN observations and 3σ sensitivity limit. The SNRs detected by Westcott (2014) have peak flux densities in the range of 0.15-0.93 mJy. This implies that there are no young radio SNRs with flux densities greater than the sensitivity limits and any older SNRs have expanded and the smooth emission is resolved out and therefore not detected.

4.6 NGC 147

The 3σ noise levels of the NGC 147 observation is 0.2715 mJy/beam. A SNR at an equivalent distance would require a luminosity of 1.916×10^{16} W Hz⁻¹ to be accurately detected. No SNRs were detected above this limit although it is possible that lower luminosity SNRs are present within the galaxy but haven't been detected. Previous studies by Mould et al. (1983) and Davidge (2005), however, state that there is little star formation within the galaxy younger than 1 Gyr, by which time any SNRs would will have become undetectable. The mean lifetime of a radio SNR is approximately 60,000 years (Frail et al. 1994; Maoz and Badenes 2010), therefore we wouldn't expect to detect any SNRs regardless of the noise levels, observation duration or SNR flux density.

4.7 NGC 185

The observation of NGC 185 has a 3σ noise level of 0.2244 mJy/beam. A SNR at an equivalent distance would require a luminosity above 1.479×10^{16} W Hz⁻¹ to be accurately detected above the noise level. No SNRs were detected above the

noise level, although it is possible that SNRs with luminosities below this limit are present but have not been detected. Previous studies by Davidge (2005) and Butler and Martínez-Delgado (2005), however, concluded that the most recent star formation was approximately 400 Myr ago. Taking into account the mean SNR lifetime of 60,000 years, any SNRs that were produced in the last round of star formation would now be undetectable. Like NGC 147, we wouldn't expect to detect any SNRs regardless of noise levels, observation duration or SNR flux density.

4.8 NGC 205

The 3σ noise level of the NGC 205 observation is 0.4350 mJy/beam and a SNR at an equivalent distance would need a luminosity greater than $3.433 \times 10^{16} \text{ W Hz}^{-1}$ to be detected. No SNRs greater than this limit have been detected, although it is possible that SNRs within luminosities lower than the limit are present but are below the noise level. However, studies by Cappellari et al. (1999); Davidge (2005) indicate that there is no recent star formation younger than 50-100 Myr. If this is accurate, then any possible SNR would no longer be detectable as this time-scale is greater than the typical lifetime of a radio SNR.

4.9 NGC 221

The 3σ noise level of the NGC 221 observation is 0.4632 mJy/beam. A SNR at the same distance would require a luminosity greater than $3.328 \times 10^{16} \text{ W Hz}^{-1}$ to be detected above this noise level. No SNRs were detected above this limit, although it is a possibility that SNRs with luminosities below this limit could be present without being detected in the observations. Recent work by Jones et al. (2015) found that the youngest stellar population is around 0.5 Gyr, which is outside of the expected lifetime of a SNR. From this it is possible to state that

there are likely not any detectable SNRs within NGC 221.

4.10 M31

The observations of M31 have a 3σ noise level of 0.3759 mJy/beam. A SNR at an equivalent distance must have a luminosity greater than $2.808 \times 10^{16} \text{ W Hz}^{-1}$ to be accurately detected in the observations. Various studies (Sasaki et al. 2012; Lee and Lee 2014; Galvin and Filipovic 2014) confirm that there are a large number of old and extended radio SNRs in M31. An optical study by Lee and Lee (2014) found a total of 156 SNR candidates in the galaxy, 120 of which were considered to be CCSNRs. Galvin and Filipovic (2014) carried out 20 cm observations of the same sample but found only 13 of these candidates were emitting radiation at a wavelength of 20 cm. They also carried out further analysis of 98 candidates throughout the field of M31 and found that 72 of these have the typical spectral properties of SNRs, and so are assumed to be such. Of the 13 confirmed radio SNRs in the 20 cm Galvin and Filipovic (2014) sample, the range in flux densities is between 0.65 and 4.09 mJy and 7 are within the e-MERLIN 27 '5 FOV. The flux density values for these sources are greater than the sensitivity limits and therefore should be detected providing that they are compact sources. The close proximity of M31 means that older SNRs could have expanded to the point where the emission is resolved out in the e-MERLIN observations. Using values from the study of radio sources in M82 by Fenech et al. (2008), the mean SNR diameter of 2.9 pc equates to an angular diameter of 0 '76 at a distance of 0.79 Mpc. The e-MERLIN beam size of 0 '36 \times 0 '13 in the M31 observations means that some of the smooth emission from SNRs of this diameter would be resolved out. A SNR of 0 '76 diameter must have a flux density of 1.13 mJy to be detected given the resolution of the e-MERLIN observations, which is within the range of flux densities for confirmed SNRs in M31. This implies that deeper observations of the galaxy are required to detect the SNRs that are present and above the

observational limits.

4.11 NGC 278

The 3σ noise levels for the observations of NGC 278 are 0.2181 mJy/beam. A SNR at an equivalent distance requires a luminosity greater than $3.633 \times 10^{18} \text{ W Hz}^{-1}$ to be accurately detected in the observations. No SNRs have been detected above this limit, although there may be lower luminosity SNRs within the galaxy that are below the limit and therefore cannot be detected due to the noise levels. However, there are no previously documented SNRs within the galaxy despite its current star formation episode (Knapen et al. 2004), hence more observations of this galaxy must be undertaken to decipher whether there are no SNRs or whether the e-MERLIN observations did not include enough observing time on the galaxy.

4.12 NGC 7741

The observations of NGC 7741 have a 3σ noise level of 0.3090 mJy/beam. A SNR at an equivalent distance would need a luminosity greater than $7.538 \times 10^{18} \text{ W Hz}^{-1}$ to be accurately detected. It is possible that there are SNRs within NGC 7741 of a lower luminosity that have not been detected, which is likely considering the current star formation episode confirmed by numerous studies including Eskridge et al. (2002); Garrido et al. (2002); Hernandez et al. (2005). Therefore, more observation of this galaxy are needed to conclude whether there are no SNRs or whether the e-MERLIN observations did not include enough observing time on the galaxy.

4.13 NGC 7798

The 3σ noise levels of the NGC 7798 observations are 0.2925 mJy/beam, and a SNR at an equivalent distance would require a luminosity greater than $3.720 \times 10^{19} \text{ W Hz}^{-1}$ to be accurately detected in the observations. It is possible that there are SNRs with luminosities lower than this limit within the galaxy that have not been detected. This is supported by previous studies (Considère et al. 2000; Schmitt et al. 2006a) that indicate a current star formation episode within the galaxy which makes it likely that SNRs are present. This implies that more observing time is required to ensure that all flux is detected.

4.14 Determining a Star Formation and Radio Supernova Rate from Radio Observations

Using radio observations to determine star formation and radio supernovae rates is beneficial as it does not require corrections for dust extinction, unlike in infrared or sub-millimetre observations where it must be accounted for (Lenc and Tingay 2006). As the main contributor to radio emission is non-thermal synchrotron emission, SNRs can be used to find both a radio supernova and star formation rate in a galaxy.

As cosmic ray electrons (CREs) continue to emit light at radio frequencies well after the SNR is able to be detected, simply dividing the total galaxy luminosity by a typical SNR luminosity would result in an overestimate of the SFR. The following equations have been adapted from Condon (1992); they account for progenitor stars over $5 M_{\odot}$ and for the CRE problem, and assume the Miller-Scalo initial mass function (IMF) (Miller and Scalo 1979) with a mass range of 5-100 M_{\odot} .

The star formation rate of a galaxy can be found using

$$L_\nu = 5.3 \times 10^{21} \cdot \nu^{-\alpha} \cdot SFR \quad (4.3)$$

where L_ν is the luminosity of the galaxy at a certain frequency in W Hz^{-1} , the SFR is measured in $\text{M}_\odot\text{yr}^{-1}$ and α is the spectral index. By using the typical non-thermal spectral index of ~ 0.8 and a frequency of 1.5 GHz (20 cm), this becomes

$$SFR = \frac{L_{1.5}}{3.83 \times 10^{21}} \quad (4.4)$$

where $L_{1.5}$ is the galaxy luminosity at 1.5 GHz in W Hz^{-1} . From the SFR, it is possible to calculate a radio supernova rate using the equation

$$\nu_{SN} \sim 0.041 \cdot SFR \quad (4.5)$$

where ν_{SN} is the radio supernova rate in yr^{-1} . These equations make it possible to determine both radio supernova and star formation rates in each of the target galaxies given their luminosity limits.

The Galactic supernova remnant Cas A has a 20 cm flux density of 2101 Jy which is equivalent to $2.364 \times 10^{18} \text{ W Hz}^{-1}$, and an age of approximately 330 yr (Fesen et al. 2006). Using this as a typical SNR, it is possible to use this luminosity to determine whether we would expect to have seen any Cas A-type SNRs in the observations. Figure 4.2 shows the 1.4 GHz light curves of 10 SNRs with known ages and luminosities. The luminosity limits for the e-MERLIN observations to detect a SNR are included as red lines as a visual aid to tell whether we would expect to detect any Cas A-type SNRs if present.

4.14. DETERMINING A STAR FORMATION AND RADIO SUPERNOVA RATE FROM RADIO OBSERVATIONS

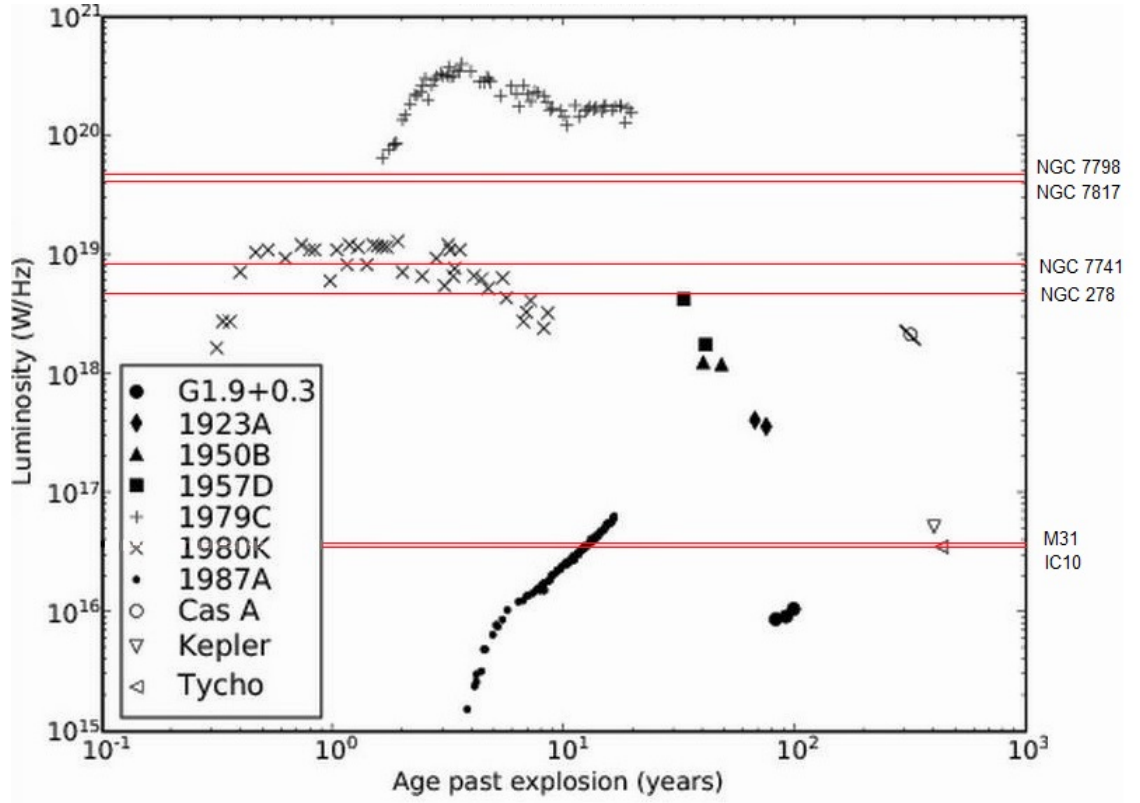


Figure 4.2: 1.4 GHz light curves of 10 SNRs whose ages are luminosities are known, including the galactic SNR Cas A. Red lines indicate the luminosity limit at which a SNR must reach to be detected in the e-MERLIN observations for each galaxy labelled. This value is taken from the 3σ noise level of each observation. Figure adapted from Murphy et al. (2008).

By using a time-frame of 330 years and the radio supernova rate for each galaxy, an estimate of the number of supernovae that have been produced can be calculated. These values can be seen along with star formation and radio supernova rates in Table 4.4. As the e-MERLIN observations did not detect any galaxies apart from IC10, the NVSS measurements have been used to calculate both the SFR and radio supernova rate for each galaxy.

Galaxy	Star Formation Rate from $H\alpha$ ($M_{\odot}\text{yr}^{-1}$)	Radio Derived Star Formation Rate ($M_{\odot}\text{yr}^{-1}$) *	Radio Su- pernova Rate (yr^{-1})	Number of SNRs in the lifetime of Cas A **
NGC 7817	-	0.707	0.0290	9.57
IC10	0.06	0.00320	0.000131	0.043
M31	0.80	0.00158	0.0000647	0.021
NGC 278	0.50	0.619	0.0254	8.48
NGC 7741	1.80	0.0955	0.00392	1.29
NGC 7798	1.63	1.25	0.0510	16.83

Table 4.4: The $H\alpha$ and radio star formation rate and supernova rate for each target galaxy. NGC 147, 185, 205 and 221 have been excluded as there are no total flux density values available from the NVSS and therefore no luminosity values. NGC 7817 does not have a documented $H\alpha$ value for the SFR and so is left blank. References for the $H\alpha$ SFR values are as follows: IC10 value from Magrini and Gonçalves (2009), M31 value from Robles-Valdez et al. (2014), NGC 278 value from Mazzuca et al. (2008), NGC 7741 value from Martinet and Friedli (1997) and NGC 7798 value from Schmitt et al. (2006b).

*Derived from NVSS flux density measurements and calculated using Equation 4.4

**Assuming the age of the Cas A SNR is 330 years

NGC 147, 185, 205 and 221 have been excluded from Table 4.4 as they were undetected in both the e-MERLIN and NVSS observations and therefore could not be used for analysis of star formation or radio supernova rates.

In all included galaxies apart from NGC 278, the SFR has been underestimated by the NVSS measurements. Equations 4.4 and 4.5 assume a mass range of 5-100 M_{\odot} whereas the majority of the $H\alpha$ SFRs assume a Salpeter IMF (Salpeter 1955) with a mass range of 0.1-100 M_{\odot} . The larger mass range in the $H\alpha$ obser-

vations would yield a higher SFR as a greater volume of stars is included in the calculations. The underestimates could also result from incorrect $H\alpha$ extinction corrections which would also result in larger SFRs.

Another cause of the radio SFR underestimates for the target galaxies with large angular scales is the resolving out of flux. In the case of M31 where the SFR is hugely underestimated, there is much extended emission due to the proximity of the galaxy which is not being picked up in the NVSS observations. This is due to the nature of radio interferometry observations, in which a lack of short spacings limits the largest scales that can be detected. As there are no zero baselines in the VLA, not all extended emission is being detected and therefore the galaxy luminosity values will also be underestimated. In the VLA D-configuration the shortest projected baseline is 164λ which corresponds to a maximum angular scale of around $13'$. As M31 has a maximum angular scale of around $103'$, much of the emission from the galaxy is likely to be resolved out.

This effect has also affected the number of supernovae predicted in the lifetime of Cas A for each galaxy. M31, IC10 and NGC 7741 exhibit extended emission that is being resolved out, hence the supernova rate is most likely an underestimate which therefore makes the number of supernovae in the lifetime of Cas A an underestimate. The other galaxies are more compact, which means that their emission is less likely to be resolved out and the calculated values in Table 4.4 are more accurate.

4.15 Summary

In NGC 7817 for which we have more accurate predictions in Table 4.4, approximately 9 radio supernovae are expected to have been created in the lifetime of Cas A which indicates that SNRs do exist in the galaxy with lifetimes less than ~ 330 yr. Due to the distance, a SNR must have a relatively high radio luminosity to be detected in the e-MERLIN observations as can be seen in Figure 4.2.

The luminosity limit is above that of Cas A and therefore we wouldn't expect to detect any Cas A-type SNRs in the observations. As there are no observed SNRs above the luminosity limit, it is possible to conclude that NGC 7817 does not contain any above $3.029 \times 10^{19} \text{ W Hz}^{-1}$ and any lower luminosity SNRs require longer observations to be detected.

IC10 has a lower luminosity limit of $2.760 \times 10^{16} \text{ W Hz}^{-1}$ as can be seen in Figure 4.2. The supernova rate for IC10 calculated in Table 4.4 is likely an underestimate of the true supernova rate, and therefore the number of supernovae created the lifetime of Cas A is also an underestimate. As mentioned in Section 4.5, previous studies such as that by Westcott (2014) show that the galaxy does contain a number of older radio SNRs although any extended emission is resolved out in the e-MERLIN observations.

Like IC10, the supernova rate for M31 is likely an underestimate and therefore so is the number of supernovae created in the lifetime of Cas A. The close proximity of the galaxy means that it has a relatively low luminosity limit of $2.808 \times 10^{16} \text{ W Hz}^{-1}$ which is below the luminosity of Cas A, as can be seen in Figure 4.2. Previous studies mentioned in Section 4.10 show that there are SNRs present with luminosities greater than the point source flux density limit for these e-MERLIN observations, and therefore should have been detected if unresolved. From this it is possible to conclude that deeper observations are needed to detect the SNRs that are presented here.

NGC 278 also has a relatively high luminosity limit of $3.633 \times 10^{18} \text{ W Hz}^{-1}$ as can be seen in Figure 4.2. We expect that approximately 8 supernovae have been created in the lifetime of Cas A which indicates that there are SNRs within the galaxy. The luminosity of Cas A is just below the luminosity limit for the e-MERLIN observations, therefore we wouldn't expect to detect any Cas A-type SNRs. As there are no detections of compact objects above the luminosity limit, it is possible to conclude that there are no SNRs with luminosities greater than $3.633 \times 10^{18} \text{ W Hz}^{-1}$, and longer observations are required to detect objects

below this limit.

NGC 7741 has a luminosity limit of $7.538 \times 10^{18} \text{ W Hz}^{-1}$ which is above the luminosity of Cas A. This means that we do not expect to have detected any Cas A-type SNRs in the e-MERLIN observations. Although the the supernova rate calculated in Table 4.4 is likely an underestimate of the actual supernova rate, the values still imply that at least one supernova should have been created in the galaxy in the last ~ 330 years, although the actual value is probably much higher. This means that NGC 7741 probably does contain recent radio loud SNRs, although they must be below the e-MERLIN luminosity limit. From this it is possible to conclude that more time is needed to observe the galaxy to detect any SNRs present.

In the lifetime of Cas A, it is predicted that approximately 16 supernovae would have exploded in NGC 7798. As it is the furthest galaxy in the sample, the e-MERLIN luminosity limit is the highest at $3.720 \times 10^{19} \text{ W Hz}^{-1}$. This limit is well above the luminosity of Cas A and therefore we would not expect to detect any Cas A-type SNRs in the observations. As the supernova rate is the highest of all the galaxies, we expect that there are a number of SNRs present that are below the luminosity limit, but more time is needed to observe the galaxy to detect them.

Chapter 5

Conclusion and Future Work

The purpose of this thesis was to study the radio properties of a sample of 10 nearby, optically selected galaxies from the LeMMINGs project. The high resolution of the e-MERLIN array at L-band was utilised to image the galaxies and detect any compact objects within them.

A number of issues arose when pursuing the observations, the first of which was the amount of time spent on each observation. The galaxies were observed for 40 minutes each which in some cases proved detrimental to the detection of compact objects in the target galaxies.

A second issue is that much of the flux from some of the sample targets was resolved out due to the presence of extended emission. This was a major problem for both IC10 and M31 which are at relatively close proximity to us with large angular scales and the presence of extended emission. The other 8 galaxies in the sample have a more compact morphology, and so the issue of resolving out the flux posed less of a problem.

Another problem stems from the galaxy sample selection, which in all cases are bright at optical wavelengths. For four galaxies, NGC 147, 185, 205 and 221, no radio emission was detected in either the e-MERLIN or NVSS observations due to the lack of recent star formation or active nucleus. Without HII regions or supernovae associated with star formation in the galaxies, very little radio

emission is produced hence they were not detected.

None of the other galaxies were detected in the observations apart from IC10, in which a HII region was observed. It is predicted that no compact objects in NGC 7817, 278, 7741, 7798 or M31 were detected because the observations were not adequately deep. Previous studies suggest that for M31 particularly, there are SNRs present within the $27'5''$ FOV of e-MERLIN that have luminosities greater than that required for detection. This implies that more time is needed to obtain a greater sensitivity and lower the limit at which a SNR can be detected. This is also relevant to the observations of NGC 7817, 278, 7741 and 7798, all of which are undergoing recent star formation and which are likely to contain compact objects such as HII regions or SNRs. Although no radio SNRs have been detected in these galaxies so far, there are few studies that analyse their radio characteristics. If more time had been spent observing these galaxies, the sensitivity of the observations would be lower, as would the luminosity limit at which a SNR could be detected.

If there was more time available to continue with this work, one of the first priorities would be to have deeper observations of the galaxies included in this sub-sample to enable the detection of radio-loud compact objects. It would also be beneficial to obtain complementary VLA data of the target galaxies to include the short baseline spacings that e-MERLIN is lacking, to ensure that extended emission is detected and not resolved out. It would also be interesting to include analysis of the *Spitzer* infrared data to investigate the FIR-radio correlation for the target galaxies and also obtain infrared star formation rates to be used as a comparison to the radio derivations.

As the LeMMINGs project contains a wide variety of normal and active galaxy types within the sample, it is hoped that other observation blocks will heed greater results in terms of the number of detections. IC10 is included in the set of 6 galaxies which will undergo deep observations of 6 hours, reaching rms sensitivity levels of $8 \mu\text{Jy}/\text{beam}$ at L-band and greatly improved imaging fidelity. It is

hoped that these observations will allow the detection of more compact objects within IC10 to further analyse the radio characteristics of the galaxy. There are no further plans to observe the other 9 galaxies for longer periods of time, although doing so would be greatly beneficial to our understanding of their radio and star-forming properties.

References

- Ables, J. G. Maximum Entropy Spectral Analysis. *A&AS*, 15:383, 1974.
- Antonucci, R. Unified models for active galactic nuclei and quasars. *Annu. Rev. Astron. Astrophys.*, 31:473–521, 1993.
- Argo, M. Lemmings: An e-merlin legacy sample, 2014. URL <http://www.jb.man.ac.uk/~mkargo/lemmings/> [Accessed:27/11/14].
- Becker, R. H., White, R. L., and Edwards, A. L. A new catalog of 53,522 4.85 GHz sources. *ApJS*, 75:1–229, 1991.
- Begelman, M., Blandford, R., and Rees, M. Theory of extragalactic radio sources. *Rev. Mod. Phys.*, 56:255–360, 1984.
- Bendo, G. J., Galliano, F., and Madden, S. C. MIPS 24-160 μm photometry for the Herschel-SPIRE Local Galaxies Guaranteed Time Programs. *MNRAS*, 423:197–212, 2012.
- Beswick, R. Radio supernovae. In *Proceedings of the 8th European VLBI Network Symposium*, page 51, 2006.
- Beswick, R. The technical capabilities of e-MERLIN, 2013. URL <http://www.e-merlin.ac.uk/tech/>, [Accessed24/11/14].
- Beswick, R. and McHardy, I. Legacy e-MERLIN Multi-band Imaging of a complete Nearby Galaxy Sample (LeMMINGS), 2008. URL http://www.e-merlin.ac.uk/legacy/proposals//e-MERLIN_Legacy_LeMMINGS.pdf, [Accessed:17/11/14].
- Beswick, R., Argo, M., Evans, R., McHardy, I., Williams, D., and Westcott, J. LeMMINGS e-MERLIN Survey of Nearby Galaxies. In *12th European VLBI Network Symposium and Users Meeting*, 2014a.
- Beswick, R., Brinks, E., and Perez-Torres, M. e. a. Ska studies of nearby galaxies: Star-formation, accretion processes and molecular gas across all environments.

- Proceedings of Science*, 2014b.
- Bressan, A., Silva, L., and Granato, G. Far infrared and radio emission in dusty starburst galaxies. *A&A*, 2002.
- Briggs, D. S. High Fidelity Interferometric Imaging: Robust Weighting and NNLS Deconvolution. In *American Astronomical Society Meeting Abstracts*, volume 27 of *Bulletin of the American Astronomical Society*, page 112.02, 1995.
- Brown, M. J. I., Jannuzi, B. T., Floyd, D. J. E., and Mould, J. R. The Ubiquitous Radio Continuum Emission from the Most Massive Early-type Galaxies. *ApJL*, 731:L41, 2011.
- Butler, D. J. and Martínez-Delgado, D. On the Stellar Populations in NGC 185 and NGC 205 and the Nuclear Star Cluster in NGC 205 from Hubble Space Telescope Observations. *AJ*, 129:2217–2231, 2005.
- Cappellari, M., Bertola, F., Burstein, D., Buson, L. M., Greggio, L., and Renzini, A. Objects in NGC 205 Resolved into Stellar Associations by Hubble Space Telescope Ultraviolet Imaging. *ApJL*, 515:L17–L20, 1999.
- Charlton, J. and Churchill, C. *Quasistellar Objects: Intervening Absorption Lines*, page 2366. 2000.
- Chomiuk, L. and Wilcots, E. M. A Universal Luminosity Function for Radio Supernova Remnants. *ApJ*, 703:370–389, 2009.
- Condon, J. Radio emission from normal galaxies. *Annu. Rev. Astron. Astrophys.*, 30:575–611, 1992.
- Condon, J. J., Helou, G., Sanders, D. B., and Soifer, B. T. A 1.425 GHz Atlas of the IRAS Bright Galaxy Sample, Part II. *ApJS*, 103:81–108, 1996.
- Condon, J. J., Cotton, W. D., Greisen, E. W., Yin, Q. F., Perley, R. A., Taylor, G. B., and Broderick, J. J. The NRAO VLA Sky Survey. *AJ*, 115:1693–1716, 1998.
- Condon, J. J., Cotton, W. D., and Broderick, J. J. Radio Sources and Star Formation in the Local Universe. *AJ*, 124:675–689, 2002.
- Considère, S., Coziol, R., Contini, T., and Davoust, E. Starbursts in barred spiral galaxies. IV. On young bars and the formation of abundance gradients. *A&A*, 356:89–101, 2000.
- Contini, T., Considère, S., and Davoust, E. Starbursts in barred spiral galaxies. III. Definition of a homogeneous sample of starburst nucleus galaxies. *A&AS*,

REFERENCES

- 1998.
- Conway, J. E., Cornwell, T. J., and Wilkinson, P. N. Multi-Frequency Synthesis - a New Technique in Radio Interferometric Imaging. *MNRAS*, 246:490, 1990.
- Cornwell, T. and Bridle, A. Deconvolution tutorial, 1996. URL <http://www.cv.nrao.edu/~abridle/deconvol/deconvol.html>, [Accessed:06/03/14].
- Davidge, T. J. The Evolved Stellar Content of NGC 147, NGC 185, and NGC 205. *AJ*, 130:2087–2103, 2005.
- Davidge, T. J. V and I photometry of bright giants in the central regions of NGC 147. *AJ*, 108:2123–2127, 1994.
- Derham, M. *Radio Emission from the Stellar Wind of the Symbiotic Star HM Sagittae*. PhD thesis, University of Manchester, UK, 2000.
- Desroches, L. B. and Ho, L. C. Candidate active nuclei in late-type spiral galaxies. *The Astrophysical Journal*, 690(1):267, 2009.
- Douglas, J. N., Bash, F. N., Bozayan, F. A., Torrence, G. W., and Wolfe, C. The Texas Survey of Radio Sources Covering -35.5 degrees δ declination δ 71.5 degrees at 365 MHz. *AJ*, 111:1945, 1996.
- Eskridge, P. B., Frogel, J. A., Pogge, R. W., Quillen, A. C., Berlind, A. A., Davies, R. L., DePoy, D. L., Gilbert, K. M., Houdashelt, M. L., Kuchinski, L. E., Ramírez, S. V., Sellgren, K., Stutz, A., Terndrup, D. M., and Tiede, G. P. Near-Infrared and Optical Morphology of Spiral Galaxies. *ApJS*, 143: 73–111, 2002.
- Fanaroff, B. L. and Riley, J. M. The morphology of extragalactic radio sources of high and low luminosity. *MNRAS*, 167, 1974.
- Fenech, D. M., Muxlow, T. W. B., Beswick, R. J., Pedlar, A., and Argo, M. K. Deep MERLIN 5GHz radio imaging of supernova remnants in the M82 starburst. *MNRAS*, 391:1384–1402, 2008.
- Fesen, R. A. The SN-SNR connection. In Holt, S. S. and Hwang, U., editors, *Young Supernova Remnants*, volume 565 of *American Institute of Physics Conference Series*, pages 119–128, 2001.
- Fesen, R. A., Hammell, M. C., Morse, J., Chevalier, R. A., Borkowski, K. J., Dopita, M. A., Gerardy, C. L., Lawrence, S. S., Raymond, J. C., and van den Bergh, S. The expansion asymmetry and age of the cassiopeia a supernova remnant. *The Astrophysical Journal*, 645(1):283, 2006.

- Filippenko, A. Optical spectra of supernovae. *Annu. Rev. Astron. Astrophys.*, 35:309–355, 1997.
- Frail, D. A., Goss, W. M., and Whiteoak, J. B. Z. The radio lifetime of supernova remnants and the distribution of pulsar velocities at birth. *ApJ*, 437:781–793, 1994.
- Frank, J., King, A., and Raine, D. *Accretion power in astrophysics*. Cambridge Univrsity Press, Cambridge, 3rd edition, 2002.
- Gallagher, J. Radio emission from small galaxies. In *The Interpretation of Modern Synthesis Observations of Spiral Galaxies*, volume 18 of *Astronomical Society of the Pacific Conference Series*, pages 191–196, 1991.
- Galvin, T. J. and Filipovic, M. D. 20 cm VLA Radio-Continuum Study of M31 - Images and Point Source Catalogues DR2: Extraction of a Supernova Remnant Sample. *Serbian Astronomical Journal*, 189:15–24, 2014.
- Galvin, T. J., Filipovic, M. D., Crawford, E. J., Tothill, N. F. H., Wong, G. F., and De Horta, A. Y. 20 cm VLA Radio-Continuum Study of M31 - Images and Point Source Catalogues. *Serbian Astronomical Journal*, 184:41–68, 2012.
- Garrido, O., Marcelin, M., Amram, P., and Boulesteix, J. GHASP: An H α kinematic survey of spiral and irregular galaxies. I. Velocity fields and rotation curves of 23 galaxies. *A&A*, 2002.
- Garrido, O., Marcelin, M., Amram, P., and Boissin, O. GHASP: An H α kinematic survey of spiral and irregular galaxies. II. Velocity fields and rotation curves of 15 galaxies. *A&A*, 399:51–61, 2003.
- Geha, M., van der Marel, R. P., Guhathakurta, P., Gilbert, K. M., Kalirai, J., and Kirby, E. N. Local Group Dwarf Elliptical Galaxies. II. Stellar Kinematics to Large Radii in NGC 147 and NGC 185. *ApJ*, 711:361–373, 2010.
- Gelfand, J. D., Lazio, T. J. W., and Gaensler, B. M. A Wide-Field, Low-Frequency Radio Image of the Field of M31. II. Source Classification and Discussion. *ApJS*, 159:242–276, 2005.
- Gregory, P. C. and Condon, J. J. The 87GB catalog of radio sources covering delta between O and + 75 deg at 4.85 GHz. *ApJS*, 75:1011–1291, 1991.
- Han, M., Hoessel, J. G., Gallagher, J. S., III, Holtzman, J., Stetson, P. B., Trauger, J., Ballester, G. E., Burrows, C., Clarke, J., Crisp, D., Griffiths, R., Grillmair, C., Hester, J., Krist, J., Mould, J. R., Scowen, P., Stapelfeldt,

REFERENCES

- K., Watson, A., and Westphal, J. A. Stellar Populations in the Dwarf Elliptical Galaxy NGC 147. *AJ*, 113:1001, 1997.
- Healey, S. E., Romani, R. W., Taylor, G. B., Sadler, E. M., Ricci, R., Murphy, T., Ulvestad, J. S., and Winn, J. N. CRATES: An All-Sky Survey of Flat-Spectrum Radio Sources. *ApJS*, 171:61–71, 2007.
- Heesen, V., Rau, U., Rupen, M., Brinks, E., and Hunter, D. Deep Radio Continuum Imaging of the Dwarf Irregular Galaxy IC 10: Tracing Star Formation and Magnetic Fields. *ApJ*, 739:L23, 2011.
- Helou, G. and Bicay, M. D. A physical model of the infrared-to-radio correlation in galaxies. *ApJ*, 415:93–100, 1993.
- Hernandez, O., Carignan, C., Amram, P., Chemin, L., and Daigle, O. BH α BAR: big H α kinematical sample of barred spiral galaxies - I. Fabry-Perot observations of 21 galaxies. *MNRAS*, 360:1201–1230, 2005.
- Hernández-Toledo, H. M., Zendejas-Domínguez, J., and Avila-Reese, V. BVRI Surface Photometry of Isolated Spiral Galaxies. *AJ*, 134:2286–2307, 2007.
- Ho, L., Filippenko, A., and Sargent, W. *Multi-Wavelength Continuum Emission of AGN*. Kluwer Academic Publishers, Dordrecht, 1994.
- Ho, L. C. What Powers the Compact Radio Emission in Nearby Elliptical and S0 Galaxies? *ApJ*, 510:631–636, 1999.
- Ho, L. C. and Peng, C. Y. Nuclear Luminosities and Radio Loudness of Seyfert Nuclei. *ApJ*, 555:650–662, 2001.
- Hoare, M., Kurtz, S., Lizano, S., Keto, E., and Hofner, P. Ultracompact hii regions and the early lives of massive stars. *Protostars and Planets V*, pages 181–196, 2007.
- Högbom, J. A. Aperture Synthesis with a Non-Regular Distribution of Interferometer Baselines. *A&AS*, 15:417, 1974.
- Honma, M., Akiyama, K., Uemura, M., and Ikeda, S. Super-resolution imaging with radio interferometer using sparse modeling. *ArXiv e-prints*, 2014.
- Irfan, M. *The C-Band All Sky Survey (C-BASS): observing diffuse galactic emission at 5GHz*. PhD thesis, University of Manchester, UK, 2014.
- Jarrett, T. H., Chester, T., Cutri, R., Schneider, S. E., and Huchra, J. P. The 2MASS Large Galaxy Atlas. *AJ*, 125:525–554, 2003.

- Jones, M. and Lambourne, R. *An Introduction to Galaxies and Cosmology*. Cambridge University Press, 2004.
- Jones, O. C., McDonald, I., Rich, R. M., Kemper, F., Boyer, M. L., Zijlstra, A. A., and Bendo, G. J. A Spitzer Space Telescope survey of extreme asymptotic giant branch stars in M32. *MNRAS*, 446:1584–1596, 2015.
- Jurusik, W. and Chyzy, K. Modelling of radio emission from normal galaxies at low radio frequencies. In *General Assembly and Scientific Symposium (URSI GASS), 2014 XXXIth URSI*, pages 1–4, 2014.
- Kang, A., Sohn, Y.-J., Rhee, J., Shin, M., Chun, M.-S., and Kim, H.-I. Near-IR photometry of asymptotic giant branch stars in the dwarf elliptical galaxy NGC 185. *A&A*, 437:61–68, 2005.
- Keel, B. Optical spectra of various kinds of active galactic nuclei, 2002. URL <http://www.astr.ua.edu/keel/agn/spectra.html>, [Accessed:06/11/14].
- Kellermann, K. and Owen, F. *Galactic and Extragalactic Radio Astronomy: Radio galaxies and quasars*, pages 563–602. 1988.
- Knapen, J. H., Whyte, L. F., de Blok, W. J. G., and van der Hulst, J. M. The nuclear ring in the unbarred galaxy NGC 278: Result of a minor merger? *A&A*, 423:481–493, 2004.
- Lacki, B., Thompson, T., and Quataert, E. The physics of the far-infrared-radio correlation. i. calorimetry, conspiracy, and implications. *ApJ*, 717(1):1, 2010.
- Lee, J. H. and Lee, M. G. A New Optical Survey of Supernova Remnant Candidates in M31. *ApJ*, 786:130, 2014.
- Lenc, E. and Tingay, S. J. The Subparsec-Scale Radio Properties of Southern Starburst Galaxies. I. Supernova Remnants, the Supernova Rate, and the Ionized Medium in the NGC 253 Starburst. *AJ*, 132:1333–1345, 2006.
- Lisenfeld, U. and Völk, H. On the radio spectral index of galaxies. *A&A*, 354:423–430, 2000.
- Longair, M. *High Energy Astrophysics*. Cambridge University Press, Cambridge, 3rd edition, 2011.
- Lonsdale, C. J., Farrah, D., and Smith, H. E. *Astrophysics Update 2: Ultraluminous Infrared Galaxies*, page 285. 2006.
- Lucero, D. M. and Young, L. M. Radio Continuum and Star Formation in CO-rich Early-Type Galaxies. *AJ*, 134:2148–2159, 2007.

REFERENCES

- Magrini, L. and Gonçalves, D. R. IC10: the history of the nearest starburst galaxy through its Planetary Nebula and HII region populations. *MNRAS*, 398:280–292, 2009.
- Maoz, D. and Badenes, C. The supernova rate and delay time distribution in the Magellanic Clouds. *MNRAS*, 407:1314–1327, 2010.
- Martinet, L. and Friedli, D. Bar strength and star formation activity in late-type barred galaxies. *A&A*, 323:363–373, 1997.
- Martínez-Delgado, D., Aparicio, A., and Gallart, C. The Star Formation History of the Local Group Dwarf Elliptical Galaxy NGC 185. II. Gradients in the Stellar Population. *AJ*, 118:2229–2244, 1999.
- Mazucca, L. M., Knapen, J. H., Veilleux, S., and Regan, M. W. A Connection between Star Formation in Nuclear Rings and Their Host Galaxies. *ApJS*, 174: 337–365, 2008.
- McDonald, A. *High resolution studies of M82 and other nearby galaxies*. PhD thesis, University of Manchester, UK, 2001.
- McDonald, A., Muxlow, T., Wills, K., Pedlar, A., and Beswick, R. A parsec-scale study of the 5/15-GHz spectral indices of the compact radio sources in M82. *MNRAS*, 334:912–924, 2002.
- Meisenheimer, K., Yates, M., and Roeser, H. The synchrotron spectra of radio hot spots. II. Infrared imaging. *A&A*, 325:57–73, 1997.
- Miller, G. E. and Scalo, J. M. The initial mass function and stellar birthrate in the solar neighborhood. *ApJS*, 41:513–547, 1979.
- Miller, S. T. and Veilleux, S. Extraplanar Emission-Line Gas in Edge-On Spiral Galaxies. I. Deep Emission-Line Imaging. *ApJS*, 148:383–417, 2003.
- Mould, J. R., Kristian, J., and Da Costa, G. S. Stellar populations in local group dwarf elliptical galaxies. I - NGC 147. *ApJ*, 270:471–484, 1983.
- Murphy, T., Gaensler, B. M., and Chatterjee, S. A 20-yr radio light curve for the young supernova remnant G1.9+0.3. *MNRAS*, 389:L23–L27, 2008.
- Narayan, R. and Nityananda, R. Maximum entropy image restoration in astronomy. *Annual Review of Astron and Astrophys*, 24:127–170, 1986.
- NED. NASA Extragalactic Database, 2015. URL {<https://ned.ipac.caltech.edu/>}.

- Nidever, D., Ashley, T., Slater, C., Ott, J., Johnson, M., Bell, E., Stanimirovic, S., Putman, M., Majewski, S., Simpson, C., Burton, W., Juetten, E., and Oosterloo, T. Evidence for an Interaction in the Nearest Starbursting Dwarf Galaxy IC 10. volume 223 of *American Astronomical Society Meeting Abstracts*, page 112.07, 2014.
- Niklas, S. and Beck, R. A new approach to the radio-far infrared correlation for non-calorimeter galaxies. *A&A*, 320:54–64, 1997.
- Nityananda, R. and Narayan, R. Maximum entropy image reconstruction - A practical non-information-theoretic approach. *Journal of Astrophysics and Astronomy*, 3:419–450, 1982.
- Panagia, N. e. a. A search for radio emission from type Ia supernovae. *ApJ*, 646: 369–377, 2006.
- Peel, M. W., Dickinson, C., Davies, R. D., Clements, D. L., and Beswick, R. J. Radio to infrared spectra of late-type galaxies with Planck and Wilkinson Microwave Anisotropy Probe data. *MNRAS*, 416:L99–L103, 2011.
- Perez-Torres, M., Alberdi, A., Beswick, R. J., Lundqvist, P., Herrero-Illana, R., Romero-Cañizales, C., Ryder, S., della Valle, M., Conway, J., Marcaide, J. M., Mattila, S., Murphy, T., and Ros, E. Core-collapse and Type Ia supernovae with the SKA. *Advancing Astrophysics with the Square Kilometre Array (AASKA14)*, art. 60, 2015.
- Peterson, B. *An Introduction to Active Galactic Nuclei*. Cambridge University Press, Cambridge, 1997.
- Phillips, A. *The physics of stars*. Wiley, Chichester, 2nd edition, 2002.
- Randriamampandry, S. M., Crawford, S. M., Cress, C. M., Hess, K. M., Vaccari, M., Wilcots, E. M., Bershadsky, M. A., and Wirth, G. D. The far-infrared-radio correlation in MS0451-03. *MNRAS*, 2015.
- Robles-Valdez, F., Carigi, L., and Peimbert, M. Star formation efficiency and flattened gradients in M31. *Rev. Mex. Astronomy and Astrophysics*, 50:271–284, 2014.
- Rossetti, A., Fanti, C., Fanti, R., Dallacasa, D., and Stanghellini, C. The B3-VLA CSS sample. VI. VLA images at 2 cm. *A&A*, 449:49–60, 2006.
- Saha, S. K. *Aperture Synthesis: Methods and Applications to Optical Astronomy*. Springer, New York, 2011.

REFERENCES

- Salpeter, E. E. The Luminosity Function and Stellar Evolution. *ApJ*, 121:161, 1955.
- Sasaki, M., Pietsch, W., Haberl, F., Hatzidimitriou, D., Stiele, H., Williams, B., Kong, A., and Kolb, U. Supernova remnants and candidates detected in the XMM-Newton M 31 large survey. *A&A*, 544:A144, 2012.
- Schmitt, H. R., Calzetti, D., Armus, L., Giavalisco, M., Heckman, T. M., Kennicutt, R. C., Jr., Leitherer, C., and Meurer, G. R. Multiwavelength Star Formation Indicators: Observations. *ApJS*, 164:52–80, 2006a.
- Schmitt, H. R., Calzetti, D., Armus, L., Giavalisco, M., Heckman, T. M., Kennicutt, R. C., Jr., Leitherer, C., and Meurer, G. R. Ultraviolet-to-Far-Infrared Properties of Local Star-forming Galaxies. *ApJ*, 643:173–185, 2006b.
- Smolcic, V., Padovani, P., Delhaize, J., Prandoni, I., Seymour, N., Jarvis, M., Afonso, J., Magliocchetti, M., Huynh, M., Vaccari, M., and Karim, A. Exploring AGN Activity over Cosmic Time with the SKA. *Advancing Astrophysics with the Square Kilometre Array (AASKA14)*, page 69, 2015.
- Steer, D. G., Dewdney, P. E., and Ito, M. R. Enhancements to the deconvolution algorithm ‘CLEAN’. *A&A*, 137:159–165, 1984.
- Thompson, A. R. Fundamentals of Radio Interferometry. In *Synthesis Imaging in Radio Astronomy II*, volume 180 of *Astronomical Society of the Pacific Conference Series*, page 11, 1999.
- Thompson, A. R., Moran, J. M., and Swenson, G. W. *Interferometry and Synthesis in Radio Astronomy*. John Wiley and Sons, 2007.
- Thronson, H. A., Jr., Hunter, D. A., Casey, S., and Harper, D. A. Submillimeter continuum emission from galaxies - Star formation and the interstellar medium in the local group dwarf IC 10. *ApJ*, 355:94–101, 1990.
- Völk, H. The correlation between radio and far-infrared emission for disk galaxies - A calorimeter theory. *A&A*, 218:67–70, 1989.
- Weiler, K., Panagia, N., and Montes, M. SN 1998bw/GRB 980425 and Radio Supernovae. *ApJ*, 562:670–678, 2001.
- Weiler, K. e. a. Radio emission from supernovae. I. one to twelve year old supernovae. *ApJ*, 336:421–428, 1989.
- Westcott, J. A High-Resolution Radio Continuum Study of the Dwarf Irregular Galaxy IC10, 2014.

- Wiaux, Y., Jacques, L., Puy, G., Scaife, A. M. M., and Vandergheynst, P. Compressed sensing imaging techniques for radio interferometry. *MNRAS*, 395: 1733–1742, 2009.
- Yankulova, I. M., Golev, V. K., and Jockers, K. The luminous infrared composite Seyfert 2 galaxy NGC 7679 through the [O III] λ 5007 emission line. *A&A*, 469:891–898, 2007.
- Yatawatta, S. Adaptive weighting in radio interferometric imaging. *MNRAS*, 444:790–796, 2014.
- Young, L. M. and Lo, K. Y. The Neutral Interstellar Medium in Nearby Dwarf Galaxies. II. NGC 185, NGC 205, and NGC 147. *ApJ*, 476:127–143, 1997.